Steam Methanol Reforming - SOFC - ORC System for a superyacht application

Simulation and Heat Management using Aspen Plus

MSc Thesis

Christina Savva

TU Delft

Steam Methanol Reforming - SOFC - ORC System for a superyacht application

Simulation and Heat Management using Aspen Plus

by

Christina Savva

to obtain the degree of Master of Science in the specialization of Sustainable Energy Technology at the Delft University of Technology, to be defended publicly on Monday, August 25, 2025, at 11:00.

Chair:	Prof. Dr. ir. Wiebren de Jong
Supervisors:	Dr. ir. Lindert van Biert, ir. Bojan Grenko
External examiner:	Dr. Lorenzo Botto
Project Duration:	November 2024 - August 2025
Faculty:	EEMCS
Student number:	5950368

Cover: *The Obsidian superyacht* by Feadship in *https://www.feadship.nl/fleet/obsidian*

TU Delft

Acknowledgements

Firstly, I would like to express my gratitude and appreciation to my supervisors, Prof. Dr. ir. Wiebren de Jong, Dr. ir. Lindert Van Biert and PhD supervisor, ir. Bojan Grenko, for their support and guidance throughout this thesis. Specifically, I would like to sincerely thank Bojan for the time he dedicated, his kindness and patience. Additionally, I would like to thank Mr. Lorenzo Botto for participating in this thesis assessment committee. I would also like to thank Amogh Amladi for his assistance with Aspen Plus and for his invaluable advice on building my model. From Feadship, I thank Berend van Veldhuizen for this input on SOFCs and maritime systems. I gratefully acknowledge EKO Cyprus Ltd. Scholarships Foundation for awarding me the Proud of Youth Scholarship, which generously covered my tuition for the academic year 2024-2025.

Numerous people have enriched my two years at TU Delft and I am very grateful for the opportunities they gave me. Especially, Mr. Robin Vismara, my fellow PV Lab TAs and Solar Engineering TAs and supervisors. Working with you has been both enjoyable and enriching, helping me learn and develop over the past two years. I greatly value all the experiences you have given me to grow and contribute.

Lastly, I would like to thank my family for their unwavering support and love over the past two years. I cherish every moment and memory with my old and new friends in the Netherlands, whom I thank for their love and encouragement. Working on my thesis along with all of you truly made my days brighter and remains one of my fondest memories at TU Delft. And finally, Nicolas, thank you for being my rock through it all. This wouldn't have been possible without you.

Christina Savva
Delft, August 2025

Abstract

As global regulations and International Maritime Organization (IMO) targets intensify, the maritime sector faces increasing pressure for decarbonization, reduction of greenhouse gas emissions and improvement of energy efficiency. Conventional marine auxiliary power systems, typically marine diesel generators, operate at low electrical efficiencies (25–45 %) and produce significant emissions. Bio-methanol, a renewable liquid fuel produced from biomass or renewable electricity, offers an attractive alternative for the yachting sector due to its high energy density, ambient-condition storage, compatibility with existing infrastructure, and ability to yield hydrogen-rich reformate gas for fuel cells. However, integrating methanol steam reforming (MSR) with solid oxide fuel cells (SOFCs) in marine environments remains largely unexplored in the literature.

This thesis investigates the design and modeling of an integrated bio-methanol steam reforming (MSR)–solid oxide fuel cell (SOFC)–Organic Rankine Cycle (ORC) system for a Feadship superyacht, developed in Aspen Plus. The bio-methanol reformer supplies hydrogen-rich gas to the SOFC stack, which subsequently drives both electric generation and heat recovery. Component integration includes thermal coupling between the MSR reactor, the afterburner, preheaters, and the ORC. The system meets auxiliary power demands from 225 kW to 325 kW and is modeled at three representative auxiliary power levels: 225 kW, 275 kW, and 325 kW. Motivated by the need to optimize both system efficiency and heat management, this work addresses a critical research gap in the techno-economic assessment of renewable methanol-based SOFC power systems for maritime applications.

The model incorporates MSR kinetics, SOFC electrochemistry—including activation, ohmic, and concentration losses—and waste heat recovery. Iterative SOFC area sizing and heat integration strategies are developed and validated, while an analysis of the operational expenditure of the system is also included. Sensitivity analyses investigate the influence of SOFC fuel utilization and operating temperature on the system's performance and consumption of resources. Analyzing key performance indicators, such as electrical generation efficiency and combined heat and power (CHP) efficiency, under different load conditions, has revealed that at the 225 kW partial-load condition, the system achieves a maximum electrical generation efficiency of 57.2% and a CHP efficiency of 79.4%, significantly outperforming conventional marine diesel generators. At the intermediate 275 kW load, the system reaches an electrical generation efficiency of 54.3% and a CHP efficiency of 71.5%. At full load (325 kW), the corresponding efficiencies are equal to 52.0% and 65.9% respectively.

The results confirm the technical feasibility of bio-methanol-fueled SOFC systems for superyacht applications and demonstrate their potential for significant efficiency gains. The developed model provides a foundation for future optimization, hybridization strategies, and onboard integration, supporting sustainable decarbonization in the maritime sector.

Contents

List of Figures

List of Tables

Nomenclature

Abbreviations

Abbreviation	Definition
AC	Alternating Current
AE	Air Electrode
AOGR	Anode Off Gas Recovery
ASHRAE	American Society of Heating, Refrigerating and Air-Conditioning Engineers
ATRM	Autothermal Methanol Reforming
CAPEX	Capital Expenditure
CCS	Carbon Capture and Storage
CCU	Carbon Capture Utilization
CHP	Combined Heat and Power
CII	Carbon Intensity Indicator
COGR	Cathode Off Gas Recovery
DC	Direct Current
DMFCs	Direct Methanol Fuel Cells
EEXI	Energy Efficiency Existing Ship Index
EMS	Energy Management System
EU	European Union
FC	Fuel Cell
FE	Fuel Electrode
GDC	Gadolinium-doped Ceria
GHG	Greenhouse Gas Emissions
GWP	Global Warming Potential
H/C	Hydrogen-to-Carbon ratio
HFO	Heavy Fuel Oil
HT	High-Temperature
ICE	Internal Combustion Engine
IMO	International Maritime Organization
IMPCA	International Methanol Producers and Consumers Association
ISO	International Organization for Standardization
KPIs	Key Performance Indicators
LCOE	Levelized Cost of Energy
LHSV	Liquid Hourly Space Velocity (h^{-1})
LHV	Lower Heating Value (J/kg)
LNG	Liquefied Natural Gas
LPG	Liquefied Petroleum Gas
MCFC	Molten Carbonate Fuel Cell
MD	Methanol Decomposition
MGO	Marine Gas Oil

Abbreviation	Definition
MS	Multi-Stage
MS-AOGR	Multi-stage Anode Off Gas Recovery
MSR	Methanol Steam Reforming
MSW	Municipal Solid Waste
OPEX	Operational Expenditures
ORC	Organic Rankine Cycle
ODP	Ozone Depletion Potential
PEMFC	Polymer Electrolyte Membrane Fuel Cell
PENG-ROB	Peng-Robinson
PI	Proportional-Integral controller
POM	Partial Oxidation
PSA	Pressure Swing Absorption
r-MD	Reverse Methanol Decomposition
r-MSR	Reverse Methanol Steam Reforming
RGibbs	Minimizing Gibbs free energy reactor model
REquil	Equilibrium reactor model
RPlug	Plug flow reactor model
rSOC	Reversible Solid Oxide Cell
r-WGS	Reverse Water Gas Shift
RWGSR	Reverse Water Gas Shift Reaction
sCO_2	Supercritical Carbon Dioxide
S/C	Steam-to-Carbon molar ratio
SMR	Steam Methane Reforming
SOFC	Solid Oxide Fuel Cell
SS-EGC	Single-Stage Exhaust Gas Combustion
SWRO	Sea Water Reverse Osmosis
TPBs	Triple Phase Boundaries
T-S	Temperature-Entropy
WHSV	Weight Hourly Space Velocity (h^{-1})
WGSR	Water-Gas Shift Reaction
YSZ	Yttria-Stabilized Zirconia

Symbols

Symbol	Definition	Unit
A	Area	m^2
D_{eff}	Effective diffusion coefficient	m^2/s
D_{Kn}	Knudsen diffusion coefficient	m^2/s
D_{i-k}	Binary molecular diffusion coefficient	m^2/s
E	Activation energy	J/mol
E_0	Reversible potential	V
F	Faraday's Constant	96,485 C/mol
I	Current	A
M_d	Molecular Mass	g/mol
N	Number of tubes	-
P	Power	W
p	Partial pressure	bar
R	Universal Gas Constant	8.3145 J/mol·K
R^2	Coefficient of determination	-
T	Temperature	°C
U_f	SOFC Fuel Utilization factor	-
V	Volume	m^3
V_{Act}	Activation overpotential	V
V_{cell}	SOFC Stack Voltage	V
V_{Conc}	Concentration overpotential	V
V_d	Diffusion volume	-
V_N	Nernst overpotential	V
V_{Ohm}	Ohmic overpotential	V
W	Mass	kg
e^-	Electron	-
h	Reactor's length	m
j	Current density	A/m^2
$j_{0,i}$	Exchange current density	A/m^2
n	Number of electrons transferred	$mol_{electron}/mol_{reactant}$
r	Tube radius	m
r_{const}	Electronic resistance	$\Omega \cdot m^2$
$\dot{m}$	Mass flow	kg/s
$\dot{n}$	Molar flow	mol/s
$\dot{Q}$	Thermal power	W
$\dot{r}$	Reaction rate	$mol_{\mathrm{CH_3OH}} g^{-1}_{\text{catalyst}} \cdot s^{-1}$
	Greek Symbols	
α	Symmetry factor	-
γ	Pre-exponential factor	A/m^2
δ	Thickness	m
ΔH^o	Standard Enthalpy Change of a Reaction	kJ/mol
ϵ	Reactor's void fraction	-
ε_{el}	Porosity of electrodes	-
η	Efficiency	-
λ	Combustion excess air ratio	-
ρ	Density	kg/m^3
σ	Conductivity	$\Omega^{-1} \cdot m^{-1}$
τ	Tortuosity of electrodes	-

Chemical Components

Component	Definition
R123	2,2-Dichloro-1,1,1-trifluoroethane
R1233zd(E)	trans-1-chloro-3,3,3-trifluoropropene
R134a	1,1,1,2-Tetrafluoroethane
R1234ze(E)	Trans-1,3,3,3-Tetrafluoropropene
R245fa	1,1,1,3,3-Pentafluoropropane

1 Introduction

1.1. Problem Definition

The maritime industry is under increasing pressure to reduce greenhouse gas emissions and improve energy efficiency while maintaining operational reliability [100]. With international regulations, such as those from the IMO, driving the decarbonization agenda [47], the adoption of alternative fuels and energy conversion technologies has become crucial for sustainable maritime transport [26]. Currently, electricity on most vessels is predominantly supplied by diesel generators, which, while reliable, operate at relatively low practical efficiencies and produce significant greenhouse gas and pollutant emissions [12, 15]. These limitations highlight the urgency of transitioning toward cleaner, more efficient onboard power systems.

Among alternative fuels, methanol has emerged as a promising candidate due to its liquid state at ambient conditions, ease of storage, compatibility with existing infrastructure, and potential for renewable production [47]. When produced from biomass or waste sources, bio-methanol significantly reduces well-to-wake CO_2 emissions, offering a practical route toward low-emission marine propulsion [36].

In luxury yachts—particularly in the superyacht segment—auxiliary power systems are essential for supporting onboard comfort, safety, and daily operations [12]. These systems provide electricity and heat for heating, ventilation, air conditioning, lighting, navigation, communication, and other loads, operating regardless of whether the vessel is cruising, anchored, or docked. This continuous demand makes the efficiency and sustainability of the auxiliary system a critical factor in the yacht's overall environmental impact. As such, decarbonizing the auxiliary system offers an effective pathway for emission reduction without compromising onboard luxury or reliability.

Methanol can be used directly in high-temperature fuel cells such as Solid Oxide Fuel Cells (SOFCs), although these cells generally operate most efficiently on hydrogen or syngas, with studies showing that the maximum power output of hydrogen-fed SOFCs is slightly higher than that of methanol-fed ones [43]. Methanol steam reforming (MSR) provides a viable onboard solution to convert bio-methanol into a hydrogen-rich gas mixture [57]. When coupled with an SOFC system, this reformate can be used to generate electricity at high efficiency, while also offering opportunities for waste heat recovery. The steady power profile and fuel flexibility of SOFCs make them well-suited for supplying base auxiliary loads in hybrid marine systems, with other technologies such as PEMFCs (Polymer Electrolyte Membrane Fuel Cells) or batteries compensating for dynamic variations [11].

To further improve energy utilization, the integration of an Organic Rankine Cycle (ORC) allows recovery of residual heat from the fuel cell and reformer exhaust, enhancing the overall system efficiency [58, 79]. However, the successful implementation of such an integrated system requires careful thermal management, component synergy, and validation under realistic operating conditions.

While methanol and fuel cell technologies have been increasingly studied for marine propulsion, relatively little attention has been given to their integration in auxiliary energy systems, particularly for larger or luxury vessels such as superyachts. Moreover, most existing research focuses on simplified subsystem analysis or does not consider real operational profiles from industry [61, 114, 63]. This thesis addresses that gap by designing and evaluating the performance of a fully integrated MSR–SOFC–ORC system tailored for a superyacht auxiliary power application.

The study is based on operational data provided by Feadship [32], including power demand profiles for the auxiliary and overall systems during sailing, anchoring, and harbor scenarios. The auxiliary system is expected to be in operation during nearly the entire working life of the ship. This real-world dataset enhances the practical relevance of the model and allows for a performance assessment under representative marine conditions. The study contributes new insights into system integration, thermal coupling, and component performance under realistic load conditions—providing a foundation for practical implementation in high-end marine applications. By modeling and simulating the system using the Aspen Plus process simulation software, this research explores the influence of varying operating parameters on key performance indicators. The findings aim to support future experimental and industrial applications of bio-methanol-fueled SOFC systems in the maritime sector.

1.2. Research Questions

The project's main research question is:

Under which conditions is an MSR-SOFC-ORC system a suitable auxiliary power and heat generation solution for the Feadship superyacht in terms of efficiency, fuel consumption, operational costs and thermal integration?

In order to develop the necessary background for the system and answer the primary research question, the following subquestions are examined in the literature overview in Chapters 2 - 4:

a) **What is the suitability of methanol and methanol reforming technologies as fuel solutions for the maritime sector?**

b) **What are the technical and operational considerations for selecting an SOFC technology for marine auxiliary applications, and how can methanol steam reforming be effectively integrated with it to achieve thermal and operational synergy?**

c) **What are the advantages and limitations of an SOFC-based power system for marine applications, considering the auxiliary power demand characteristics of the Feadship superyacht, including integration with an ORC?**

d) **What is the potential of an ORC as a waste heat utilization solution for the system?**

Furthermore, the system modeling and simulations will analyze this system at a steady state for three different power demands of the ship's auxiliary system. Using the results, the system performance is evaluated based on the following Key Performance Indicators (KPIs). It should be noted that the performance assessment focuses exclusively on first-law thermodynamic efficiencies, without incorporating an exergy-based (second-law) analysis.

1. **System's electrical generation and combined heat and power (CHP) efficiency**
2. **SOFC and ORC efficiency**
3. **Methanol, air, and water consumptions**
4. **System's operational costs (€/year)**

1.3. Objective

The objective of this thesis is to design and evaluate an integrated MSR–SOFC–ORC system for the auxiliary power supply on a Feadship superyacht, using Aspen Plus simulations to assess thermal integration, system and subsystem efficiencies, and resource usage. To achieve this, a steady-state model is developed in Aspen Plus, incorporating detailed thermodynamic representations of each subsystem as well as an SOFC model and a kinetic model for MSR. The system's performance is evaluated under three operational auxiliary load levels based on real operational data provided by Feadship. KPIs such as efficiencies and resource consumption, and annual operational expenditures were used to assess the feasibility and effectiveness of the integrated energy system. This approach enables a comprehensive analysis of the system's potential as a sustainable power solution for luxury maritime applications.

1.4. Thesis Outline

The thesis is divided into three parts: the literature review, the system design and evaluation, and the results, operational costs, and recommendations. The report begins with an overview of the maritime sector in Chapter 2, addressing emissions, marine fuels, and the potential of fuel cells. Secondly, Chapter 3 explores bio-methanol as a marine fuel, addressing its sources, composition, storage, feasibility, and safety. It also examines key methanol reforming processes, with a focus on MSR, including reaction mechanisms, catalysts, reactor types, kinetics, and product composition. Chapter 4 introduces the operation, benefits of SOFCs, and their integration with MSR. Moreover, Chapter 5 introduces relevant MSR-SOFC and ORC systems, with supporting literature and system descriptions. Chapter 6 defines the integrated system and the basis of design, covering the system's layout and architecture, model development and detailing the key performance indicators. Next, Chapter 7 outlines the modeling methods and overall model development for each subsystem, including efficiency definitions. Chapter 8 addresses the sizing of core components, such as the ORC, SOFC, MSR reactor, and heat utilization network. Chapter 9 presents system modeling results, including temperature profiles, performance, consumption of resources, and sensitivity analyses. Chapter 10 evaluates operational costs, such as fuel, SOFC stack, and catalyst expenses. Finally, Chapter 11 provides recommendations and concludes with the key findings of the thesis.

2

Maritime Sector

This chapter presents an overview of the maritime sector and the critical need for its decarbonization in the context of global climate goals. Section 2.1 discusses current greenhouse gas emission trends and highlights the sector's reliance on fossil fuels. The limitations of conventional marine fuels are examined alongside emerging alternatives such as methanol, ammonia, and hydrogen. Section 2.2 outlines international regulations and policy targets, particularly aiming at guiding the transition toward low- and zero-emission shipping. Finally, Section 2.3 introduces fuel cell technologies—specifically SOFCs—as a promising solution for clean and efficient onboard energy conversion.

2.1. Decarbonisation of the Maritime Sector

2.1.1. Emissions

The transportation sector is a significant contributor to global greenhouse gas (GHG) emissions, accounting for approximately 15% of total emissions in 2019 [48]. Within this sector, the maritime industry plays a significant role, facilitating over 80% of global trade through marine transportation [99]. However, in 2023, carbon emissions from international shipping were recorded as 20% higher than a decade ago, highlighting the urgent need for the shipping industry to decarbonise while maintaining economic growth [100].

Figure 2.1 illustrates the total carbon dioxide emissions of all vessels over the years 2012-2023 [100]. A rising trend of emissions can be clearly seen in the graph.

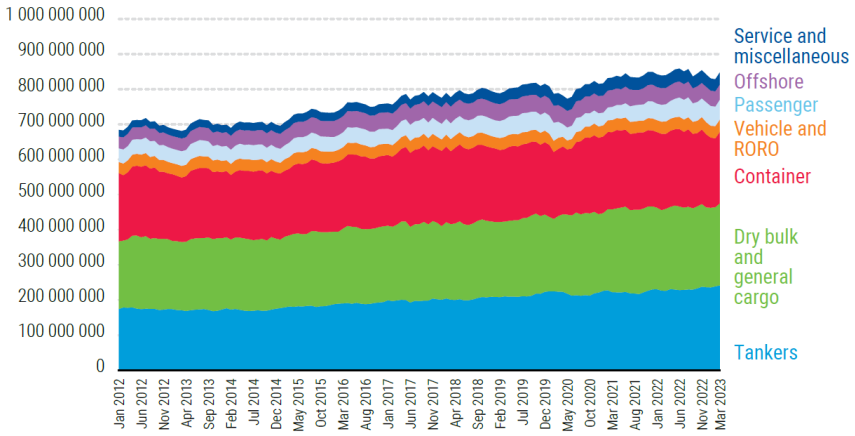

Figure 2.1: Total CO_2 emissions in tons per ship types, from January 2012 until March 2023 [100].

Carbon dioxide (CO_2) emissions are of particular concern because they constitute the majority of GHG emissions from marine fuels and have long-term climate impacts due to their persistence in the atmosphere. In 2018, CO_2 made up about 98% of the total greenhouse gas emissions from the shipping sector, while methane (CH_4) and nitrous oxide (N_2O) contributed the remaining 2% [52]. This highlights that CO_2 is the primary greenhouse gas released by the industry. Although the total CO_2 emissions have continued to grow,

the emissions per ton-mile have decreased, highlighting the improved energy efficiency across the maritime industry. Moreover, carbon intensity varies by vessel type, which is highlighted in Figure 2.2. Emissions from container ships are higher per ton-mile compared to dry and liquid bulk shipping.

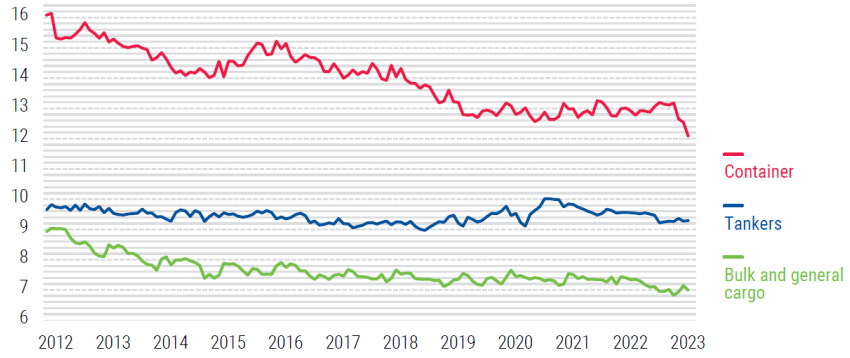

Figure 2.2: Monthly CO_2 emissions per ton-mile of the global maritime feet for three main vessel types from January 2012 until March 2023 (g CO_2/ton·nautical mile) [100].

2.1.2. Conventional Marine Power Systems

Diesel generators are used predominantly on ships for electricity-power production [12, 49]. Although their efficiencies can peak at around 45% for large-scale units [15], due to overcapacity requirements and frequent operation away from optimal load, their practical efficiencies are often in the range of 25–40%. This is due to mechanical losses at part load, which further reduce performance, as rotational speed must be maintained to match grid frequency. Gas turbine generators, while offering high specific power and low maintenance needs, typically have peak efficiencies of only 30–40% for heavy-duty maritime applications, making them less appealing from a fuel consumption perspective compared to other technologies.

2.1.3. Maritime Fuels

The maritime sector continues to rely heavily on fossil fuels; however, as reported in 2024, their dominance is expected to decline with the next generation of ships [26]. As can be seen in Figure 2.3, in the current operating fleet, 99.17% of ships operate using conventional fuels, with just 0.83% using alternative fuels. Within the alternative fuels used, liquefied natural gas (LNG) (0.62%) dominates, with minor contributions from liquefied petroleum gas (LPG) (0.15%) and methanol (CH_3OH) (0.06%). These numbers change for the ships being built currently or are to be built, where 83.15% of ships will still rely on conventional fuels and 16.85% plan to use alternative fuels. Within the alternative fuels used, LNG with 8.98% and methanol with 5.03% lead, with smaller shares for LPG (1.88%), hydrogen (H_2) (0.50%), and ammonia (NH_3) (0.40%).

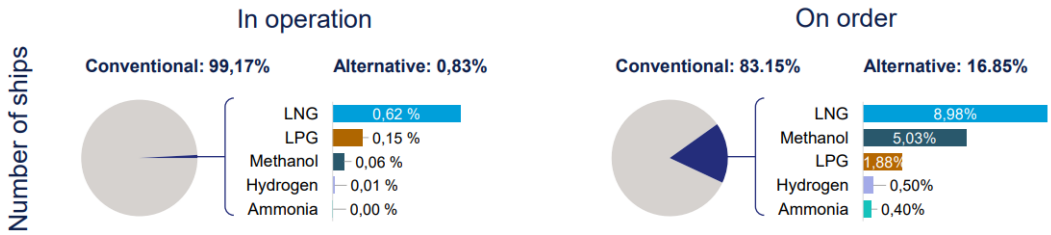

Figure 2.3: Proportion of the maritime fleet utilizing conventional fuels compared to alternative fuels [26].

As expected, the different marine fuels present varied properties, such as heating value, energy density, and storage conditions, which are compared in Table 2.1. Marine gas oil (MGO) and LNG have high volumetric energy densities, making them more suitable for storage and transportation in marine applications. A great disadvantage of LNG is its necessary cryogenic storage temperature. Hydrogen is highlighted with a high lower heating value of 120 MJ/kg; however, it faces major challenges due to low volumetric energy density, low temperatures (-253 °C) for liquefied storage, and high pressures (700 bar) for gaseous storage. Methanol and liquid ammonia present a balance in terms of easier storage handling and lower emissions potential, while hydrogen and ammonia hold promise for decarbonization despite their current limitations.

Table 2.1: Properties of marine fuels [1].

Marine Fuel	Lower Heating Value (MJ/kg)	Volumetric energy density (GJ/m^3)	Storage pressure (bar)	Storage temperature (°C)
MGO	42.7	36.6	1	20
LNG	50	23.4	1	-162
Methanol	19.9	15.8	1	20
Liquid NH_3	18.6	12.7	1 to 10	-34 (at 1 bar) to 20 (at 10 bar)
Liquid H_2	120	8.5	1	-253
Compressed H_2	120	7.5	700	20

Figure 2.4 illustrates the well-to-wake GHG emissions of current and future marine fuels in three categories: fossil fuels, bio-fuels, and e-fuels. Conventional fossil fuels like liquid hydrogen, ammonia, and methanol from natural gas have high well-to-wake CO_2 emissions. At the same time, MGO and LNG also produce significant GHG emissions, with LNG performing slightly better in terms of CO_2. Bio-diesel from waste cooking oil shows lower emissions than bio-diesel from palm oil, and bio-methanol from farmed wood and black liquor present relatively low emissions, and thus are more sustainable options. It is essential to highlight the influence of biomass used as a source in the production of bio-methanol on the overall emissions in these cases. E-fuels, including e-methanol, e-ammonia, and e-hydrogen, have the lowest well-to-wake CO_2 emissions, with e-hydrogen being the cleanest alternative. Overall, the graph emphasizes the potential of bio-fuels and e-fuels to significantly reduce emissions, playing a key role in decarbonizing the maritime sector.

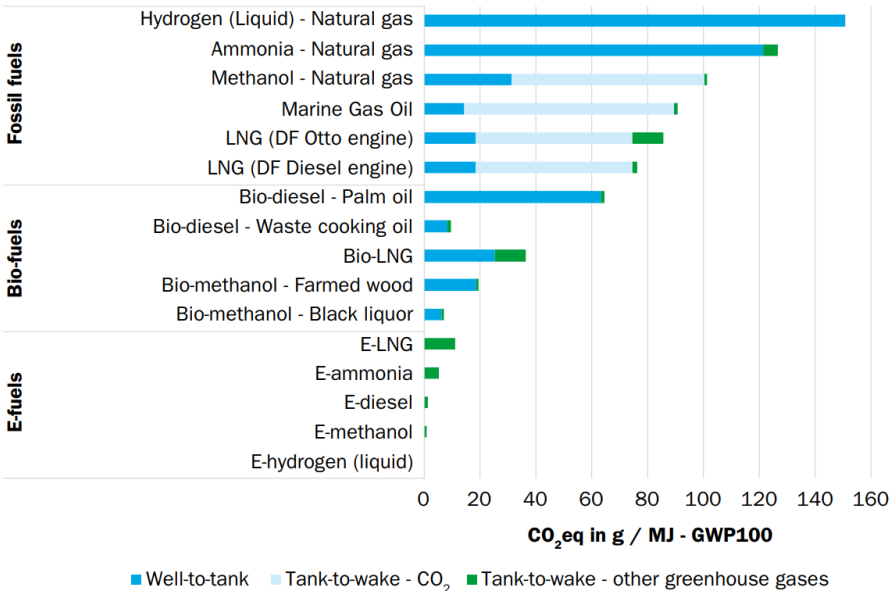

Figure 2.4: Well-to-wake CO_2 emissions from various marine fuels in g CO_2 per MJ [36].

2.2. Goals and Strategies

Since 2018, the International Maritime Organization (IMO) has implemented more actions for pollution prevention in the global shipping sector [47]. More specifically, according to the IMO 2020 regulation, the sulfur content in fuel must not exceed 0.5% by mass (m/m). In 2023, the IMO [51] announced the revised GHG Strategy, which set more ambitious goals targeting a reduction in the total annual GHG emissions of international shipping. The strategy aims to improve energy efficiency for new ships, reducing carbon intensity by at least 40% by 2030 compared to 2008 [100, 51]. Increasing the implementation of zero or near-zero GHG technologies, fuels, and energy sources, is another strategy goal, striving for 10% of the energy used by shipping by 2030 [51]. The ultimate mission is to achieve net-zero GHG emissions by 2050, aiming for at least a 20% reduction by 2030, and a 70% reduction by 2040, compared to 2008 levels.

Key measures of the IMO 2023 strategy [51] include short-term, mid-term and long-term actions. Short-term actions introduce a data collection system for ships' fuel consumption and the Energy Efficiency Existing Ship Index (EEXI) and Carbon Intensity Indicator (CII). Mid-term measures include a marine fuel standard to reduce GHG intensity and a pricing mechanism for emissions to be finalized by 2025. Additional measures until 2030 focus on improving data on emissions, addressing methane and nitrous oxide, promoting new technologies, and encouraging port developments to reduce emissions. Lastly, long-term measures will be reviewed in 2028.

The need for decarbonization of the maritime sector is urgent. To achieve these goals, researchers and scientists are looking into new emissions-free technologies, low-emission fuels, and more efficient energy systems that can be implemented on ships. Systems powered by ammonia, hydrogen and bio-fuels are currently being developed, tested and implemented [77]. Fuel cells are also a technology to be implemented on board, offering many advantages. Their application and bio-methanol usage in the maritime sector will be analysed in the following sections.

2.3. Fuel Cells in Maritime Applications

Fuel cells (FCs) can play a significant role in the maritime industry. Many researchers have studied the possible applications of fuel cells on ships and reported several advantages and drawbacks. FCs are energy conversion devices that generate electricity and heat by directly facilitating the electrochemical reaction between a gaseous fuel and an oxidant [75].

2.3.1. Types of FCs

In 2023, Fu et al. [33] reviewed the application of fuel cells and hydrogen in the maritime sector and analysed the aspects of technology, cost and regulations. The researchers discuss the types of FCs suitable for these applications. Polymer Electrolyte Membrane Fuel Cells (PEMFCs) are well-suited for maritime applications due to their low-temperature operation, fast start-up time, and high energy density, making them ideal for small vessels requiring good maneuverability. However, their susceptibility to carbon monoxide (CO) poisoning and complex water management increases system size and layout requirements. In 2016, Emonts et al. [14] proposed a hybrid maritime propulsion system with hydrogen-fueled PEMFCs, lithium-ion batteries, a DC motor, a PI-controller-based Energy Management System (EMS), and a cryogenic hydrogen tank. Compared to the diesel system, the hybrid system presented reduced weight by 10% and volume by 21%, despite a 77% higher initial cost and 46% higher fuel costs. The system offers significant emission reductions, with potential cost savings through mass production, highlighting its promise for sustainable maritime transport.

Solid Oxide Fuel Cells (SOFCs) are a strong candidate for maritime applications due to their high efficiency and effective waste heat utilization [38]. These FCs operate at higher temperatures (around 1000°C), providing excellent efficiency and structural stability through their solid electrolyte [33]. They are often integrated into hybrid power systems with heat recovery bottoming and combined cycles [33, 38]. Their applications in naval propulsion and large ship auxiliary power systems have been proven [33]. Additionally, SOFC power systems contribute to emission reduction while being capable of sustaining mission requirements for extended periods, making them a viable option for long-duration maritime operations [38]. Despite these advancements, most maritime fuel cell applications remain limited to auxiliary power, with further research and development needed to establish fuel cells as the primary propulsion system for ships [33].

Molten Carbonate Fuel Cells (MCFCs) operate at high temperatures (around 700°C), and utilize hydrocarbons such as methane and natural gas as fuel while generating significant recoverable heat [33]. Consequently, they are efficient for large ships with long operational periods. Integrating MCFC with gas turbines in a cogeneration system can substantially increase the energy conversion efficiency. Although MCFCs and SOFCs have a slow start-up time, this is less of a concern for maritime applications since they provide versatility in fuel choice and generate a considerable amount of heat that can be recovered.

Direct Methanol Fuel Cells (DMFCs) generate electricity by directly converting the chemical energy in methanol into electrical energy [110]. They are used in portable electronics such as laptops, mobile phones, and light electric vehicles, offering advantages over rechargeable batteries, including longer operation times and low operating temperatures [54]. DMFCs typically use Nafion membranes with a temperature limit of 80 °C, though some composite membranes extend this range to 180 °C. Nafion 117 is commonly used due to reduced methanol crossover, but it suffers from high methanol and ruthenium crossover, high cost, and limited thermal stability. DMFCs generally provide power outputs from hundreds of mW to several hundred W, with some achieving 54 W at 90 $mW \cdot cm^{-2}$, suitable for laptops. However, their electrical efficiency is relatively low, with under 30% of methanol's energy converted to electricity [54, 90], as losses occur through methanol

crossover and electrode irreversibility. A key limitation is durability, with noticeable degradation after 200 hours and further decline beyond 1000 hours due to catalyst poisoning and ruthenium loss, despite Nafion's high durability in PEMFCs (>60,000 hours).

While there have been some achievements and pilot projects, fuel cells like PEMFC, MCFC, and SOFC are mostly used for backup or auxiliary power on ships [33]. Fully developing them for main propulsion is still a work in progress. Table 2.2 of the Elkafas et al. [28] review summarizes and presents the main fuel cell technologies for maritime applications and their operational characteristics. DMFCs are not considered a promising power source for maritime propulsion or large auxiliary systems due to their scale, power output and short lifetime [54]. Therefore, their characteristics are not included in the following comparison table.

Table 2.2: Main fuel cell technologies and their characteristics [28].

FC Type	Temperature (°C)	Electrolyte	Typical Fuel	Power Range	Electrical Efficiency	Lifetime (h)	Applications
PEMFC	60–80 (LT-PEMFC), 110–180 (HT-PEMFC)	Water-based polymer membrane	H_2	$\leq$1 MW (up to 200 kW per module)	45–55%	60,000–80,000 (stationary); $>$25,000 (transport)	Backup power, Portable power, Distributed generation, Transportation, Specialty vehicles
SOFC	500–1000	Porous ceramic material	H_2, CH_3OH, C_xH_y	$\leq$1 MW (up to 250 kW per module)	50–60%	20,000–80,000	Auxiliary power, Electric utility, Distributed generation
MCFC	650–800	Molten carbonate salt	H_2, CH_3OH, C_xH_y	$\leq$1 MW (up to 250 kW per module)	43–55%	15,000–30,000	Electric utility, Distributed generation

2.3.2. Advantages

Fuel cells are highly promising for maritime use due to their efficiency and operational benefits. Low - temperature fuel cells reach up to 60% electrical efficiency, while high-temperature types can exceed 70% when paired with gas turbines [15]. Unlike internal combustion engines (ICEs), they are not limited by the Carnot cycle, enabling higher fuel utilization [15, 57]. With no moving parts, fuel cells operate quietly, with low vibrations and minimal maintenance needs. They perform well at part load, produce water as a byproduct, and offer flexible, modular designs for efficient onboard integration and easier maintenance [15, 28]. Compared to batteries, they provide higher volumetric energy density, making them suitable for long voyages. Emissions are minimal, and GHG reductions are achievable—especially with renewable hydrogen from electrolysis or biomass gasification [57, 81, 28].

2.3.3. Disadvantages

Despite these advantages, several challenges limit the widespread adoption of fuel cells in the maritime sector. One of the primary disadvantages is their limited commercial maturity and ongoing development delays their large-scale deployment [15]. High-temperature fuel cells are mechanically vulnerable and prone to degradation under thermal stress or rapid load changes. They also have long start-up times and slow load responses due to their thermal mass. High costs for manufacturing and maintenance remain a significant barrier. Additionally, fuel cells have lower volumetric power density than ICEs and batteries, requiring more space for equivalent power output—an issue in space-constrained ship designs. Overcoming these technical and economic hurdles is essential for their broader maritime adoption.

2.4. Conclusion

Decarbonizing the maritime sector is crucial for achieving global climate goals and improving the sustainability of international trade. While fossil fuels still comprise the majority of the current fleet, the rise of alternative fuels and stricter regulations indicate a shift toward cleaner propulsion systems. Biofuels and e-fuels, such as methanol and hydrogen, have significant potential to reduce well-to-wake emissions. Fuel cells, particularly SOFCs, are notable for their high efficiency and ability to integrate with onboard heat recovery systems. Although most applications are still focused on auxiliary power, ongoing innovation suggests a promising future for fuel-cell-driven propulsion in maritime transport.

3

Methanol and Reforming Processes

This chapter explores methanol's potential as a marine fuel, covering its key properties, renewable production pathways such as bio- and e-methanol, and relevant safety and storage considerations in Sections 3.1 to 3.3. In Sections 3.4 to 3.5 three key methanol reforming methods are reviewed—methanol steam reforming (MSR), autothermal reforming (ATR), and methanol decomposition (MD)—to identify the most suitable process for onboard hydrogen production. Finally, Section 3.6 provides a detailed focus on MSR, discussing reaction mechanisms, catalyst selection, reactor configurations, and operating parameters, thereby laying the groundwork for its integration with SOFCs in the following chapters.

Methanol

3.1. Methanol as a fuel

Methanol is a versatile liquid chemical widely used in products such as plastics, paints, cosmetics, and fuels [71] and is the third most produced commodity chemical, after ethylene and ammonia [57]. It is a transparent, colorless liquid characterized by a sweet and sharp odor [34] and produced from synthesis gas, a mixture of hydrogen, carbon dioxide, and carbon monoxide, which can be derived from various feedstocks using different technological methods [71].

Methanol offers several benefits that make it a promising option for the future adoption of bio-fuels in the maritime sector [111]. When produced from renewable energy sources and sustainable CO_2, renewable methanol can significantly reduce greenhouse gas emissions, contributing to global decarbonization goals. Secondly, methanol is in a liquid state at ambient temperatures, simplifying its storage, transportation and handling compared to other alternative fuels like hydrogen, LNG, or ammonia [111, 57]. It is also a versatile fuel, compatible with internal combustion engines, hybrid systems, fuel cells, turbine engines, and more, and it can act as a liquid hydrogen carrier [1]. Moreover, out of the existing alternative fuels, methanol has the second-highest energy density after LNG, as can be seen in Table 2.1. Lastly, existing fossil fuel infrastructure can be adapted for methanol storage with minimal modifications, further facilitating its integration into the maritime industry.

Despite these advantages, methanol faces some critical limitations. While methanol has a higher volumetric energy density than other alternative shipping fuels such as ammonia and hydrogen, its energy density is still lower than conventional fuels [47]. It can also be seen in Table 2.1, where MGO has an energy density of 36.6 GJ/m^3 and methanol's is 15.8 GJ/m^3. Moreover, its production is less efficient than other renewable fuels such as hydrogen or ammonia, and increased demand may drive the production of grey methanol from fossil fuels, potentially undermining its environmental advantages [111]. Lastly, e-methanol is a synthetic fuel made from green hydrogen and captured CO_2, using renewable energy [88]. Its production is costly, making it three to four times more expensive than fossil MGO. This cost gap limits its competitiveness despite its climate benefits.

The current methanol production pathways are presented in Figure 3.1. Grey methanol, produced from natural gas, is produced in plants with a capacity of over 1.8 million tons annually [47]. In 2020, the majority of methanol used worldwide was produced from reforming natural gas, emitting 110 g CO_2eq/MJ. Brown methanol originates from coal, grey methanol from natural gas, while blue methanol originates from natural

gas and renewable electricity, utilizing carbon capture and storage (CCS). Renewable/green methanol is produced from biomass and renewable electricity, also known as bio-methanol and e-methanol, respectively [71], and it is projected that by 2050, they will account together for approximately 80% of total production, reaching 500 million tons annually [1]. The ability of bio-methanol and e-methanol production to scale up and play a significant role in the decarbonization of the shipping sector lies in the availability of raw materials in ample quantities and at a cost-effective price at the production stage [47].

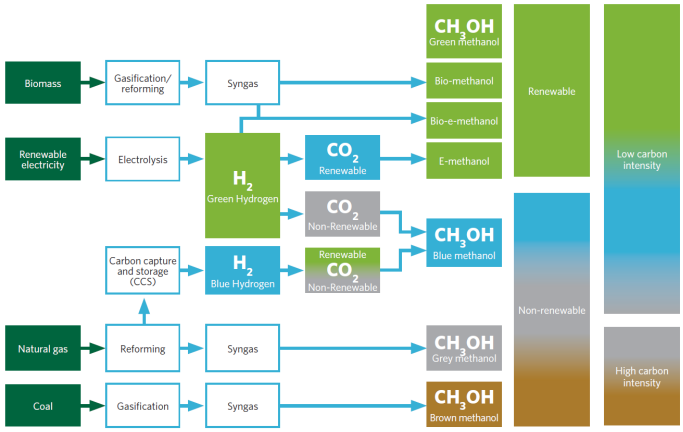

Figure 3.1: Methanol production pathways [1].

Figure 3.2 illustrates the difference in GHG emissions (in g CO_2 eq/MJ) for different methanol sources, including natural gas, coal, biomethane, solid biomass, municipal solid waste (MSW), and electricity. It also highlights the contributions of various life-cycle stages, including feedstock production, transportation, and end-of-life processes, to the final carbon emissions of methanol. The type of pathway clearly plays a major role in the well-to-wake carbon emissions. Clearly, coal-based methanol production shows the highest emissions, exceeding 250 g CO_2 eq/MJ. Renewable feedstock, such as cow manure and organic waste for biomethane, exhibits net-negative emissions due to carbon removal in their life cycle. Cow manure shows negative GHG emissions because its use avoids methane release from natural decomposition. Life cycle assessments credit these avoided emissions, often resulting in a net-negative carbon footprint [47]. Electricity sources, such as the European Union (EU) grid of 2019, have relatively high emissions compared to renewable options. It is apparent that renewable pathways, such as green methanol, bio-methanol, and e-methanol, originating from biomass or renewable electricity, exhibit low carbon intensity. In contrast, non-renewable pathways, such as gray and brown methanol, are associated with higher emissions due to the use of fossil feedstocks. Although blue methanol reduces emissions, it remains less sustainable than renewable methanol because it is produced from natural gas with CCS. Transitioning to renewable methanol production to minimize GHG emissions and comply with sustainability goals is crucial.

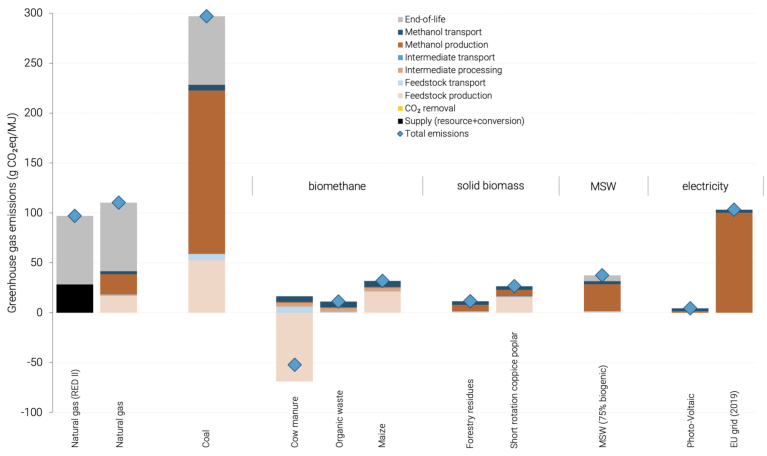

Figure 3.2: Carbon footprint of methanol production pathways [39].

3.2. Bio-methanol

3.2.1. Emissions

Bio-methanol originating from biomass and renewable sources has a significantly lower carbon emissions profile [71]. As presented in Figure 3.2, bio-methanol reduces CO_2 emissions by up to 95%, sulfur oxides (SO_x) emissions by 99%, nitrogen oxides (NO_x) by 80% and particulate matter emissions by 95% compared to conventional fuels [47]. Most renewable production pathways achieve emissions as low as 10–40 g CO_2 eq/MJ, with some pathways even resulting in negative emissions (-55 g CO_2 eq/MJ for methanol derived from biomethane produced from cow manure) [47]. Negative emissions in this context refer to the mitigation of greenhouse gases by preventing emissions that would otherwise occur in alternative systems.

3.2.2. Sources

Methanol produced from biomethane has a carbon footprint ranging from -103 to +38 g CO_2 eq/MJ [71]. The majority of anaerobic digestion facilities utilise a mixture of feedstocks to achieve an economic balance between emission reduction and biogas production (biomethane and CO_2). Waste streams and manure are the most suitable feedstocks for reducing emissions, while crops are ideal for maximizing biogas output. However, relying solely on manure or waste streams is not economically feasible.

Using cow manure as a feedstock avoids conventional treatment and is connected to methane emissions. Therefore, it is reported by the Renewable Energy Directive that the emissions avoided when using this feedstock are equal to 45 g CO_2 eq/MJ manure [71]. Hence, biomethane from manure is a negative-emission product. When converted into bio-methanol, efficiency losses amplify the negative emissions per MJ, as bio-methanol is recognized as an effective manure-removal product. Lastly, for maize, emission results vary due to differences in cropping systems, yields, and fertilizer use.

As Figure 3.1 also presents, bio-methanol can also be produced directly from biomass gasification. Im-orb et al. [76] studied a process for producing bio-methanol from oil palm residues. The process consisted of three key stages: gasification, syngas cleaning and bio-methanol synthesis. The study found that a once-through process at 750 °C with a 0.25 equivalence ratio produced the highest bio-methanol yield. Under optimal conditions, the process achieved 38.57% energy efficiency and 25.44% exergy efficiency. Based on their findings, the researchers highlighted bio-methanol's potential as a viable and sustainable alternative to fossil-based methanol.

3.2.3. Composition

Bio-methanol originating from biomass can have a varying composition based on the source used and usually it is not lab-grade. This is highlighted in the Tsujiguchi et al. [97] study, where the researches examined the feasibility of using crude bio-methanol as a fuel for a direct methanol fuel cell. In their study, they highlighted the economic challenges of bio-methanol production and thus proposed the direct use of crude bio-methanol, derived from woody biomass and produced without refining, as fuel for a fuel cell. However, crude bio-methanol contains various impurities depending on the production process and biomass used (presented in Table 3.1).

Table 3.1: Crude methanol's composition originating from syngas from gasified woods, A and B, and from natural gas, C [97].

Component	Woody biomass (wt %)		Natural gas (wt %)
	A	B	C
Methanol	91.3	93-95	96.8
Ethanol	-	0.3-0.5	0.29
1-Butanol	1.5	0	-
Methyl formate	6.0	$<$0.001	0.92
Methyl acetate	-	-	0.09
Dimethyl carbonate	-	-	0.06
Dimethyl ether	-	-	0.19
Diisopropyl ether	0.7	-	-
Water	0.5	4-5	1.64
Other	-	$<$0.1	$<$0.03

3.3. Marine Methanol

3.3.1. Feasibility

The regulations regarding emissions in the maritime sector are updated yearly. Methanol is a fuel that shipping companies can use immediately to comply with regulations aimed at reducing emissions, as it dramatically decreases SO_x, NO_x and particulate matter emissions [47]. When paired with advanced engines, methanol meets the strictest emission regulations established by the IMO. Methanol is suitable for midrange shipping vessels—in terms of size and operational range—, including cruise ships, inland waterway bulk transport vessels, short-sea container ships, ferries, short-sea tankers, deep-sea container vessels and general cargo vessels [96]. Its global access, supported by a well-established and extensive distribution and storage infrastructure worldwide, makes methanol an advantageous commodity [1]. Furthermore, methanol is available at over 120 ports worldwide and is shipped globally and its production is expected to grow five times larger in 2050 compared to 2020 (100 million tons) [47]. As of April 2024, 33 methanol-fueled ships are operating and 29 more are under construction, with a total of 269 confirmed methanol-fueled vessels expected by 2028 [26]. All in all, while methanol is a viable alternative fuel for the maritime sector and its widespread adoption will depend on addressing challenges related to production efficiency, costs, safety, and environmental impacts.

3.3.2. Purity

In the current marine fuel landscape, methanol with over 95% purity is required for combustion in marine engines [60]. In 2024, ISO 6583:2024, titled ”Methanol as a fuel for marine applications – General requirements and specifications”, was published [53]. This first international standard outlines quality requirements for methanol used in marine engines, boilers, and fuel cells [46]. It applies to methanol from any production method prior to onboard treatment and defines three fuel grades: Grade A (MMA), the most stringent, builds on International Methanol Producers and Consumers Association (IMPCA) guidelines with added provisions for lubricity and cleanliness; Grade B (MMB) follows standard IMPCA criteria; and Grade C (MMC) allows for wider tolerances in properties like density, impurities, and water content for systems that can accommodate them [46, 20].

3.3.3. Storage on board

As mentioned in Section 3.1, methanol’s energy density is much lower than MGO. In other words, on a methanol-powered ship, storage and fuel tanks take about 2.4 times more space than on ships that operate using MGO [47]. However, this disadvantage is mitigated by frequent bunkering and the fact that methanol can be stored in conventional fuel storage tanks or even ballast tanks on board a vessel. In contrast, fuels such as LNG and hydrogen require cryogenic storage, which has a greater impact on cargo space loss. Since methanol is stored at 1 bar, the need for pressure-resistant or independent tanks is eliminated. Consequently, methanol tanks can be integrated into the ship’s structure, similar to diesel tanks. This flexibility allows methanol to be stored in irregular volumes, making it a favorable option for maritime fuel. However, consideration must be given to the necessary area and volume required for methanol-preparation equipment, such as pumps. While methanol bunkering and refueling are operationally similar to MGO bunkering [47], its higher vapor pressure—around 12.8 kPa at 20 °C—implies greater volatility and requires careful attention to tank pressurization, ventilation, and safety systems, especially at elevated ambient temperatures [70]. Given that methanol remains liquid at ambient conditions, the same infrastructure used for traditional marine fuels can be adapted for methanol with minor and inexpensive modifications [47].

Methanol’s properties introduce specific challenges in handling and storage, apart from material compatibility, which needs to be considered for safe and efficient use. As a fuel, methanol can be corrosive to some metals such as aluminum, copper, zinc, titanium and some of their alloys and it may also attack plastic types, resins and rubbers [1]. As a result, compatible metals, plastics and elastomer materials have to be particularly selected. The second factor is that methanol can absorb moisture from the atmosphere. To mitigate this, methanol should be stored in a sealed container with an allowance for thermal expansion, such as larger tanks, floating roof tanks, and pressure relief valves. Moisture is miscible when absorbed by methanol and is retained as a single phase that does not affect combustion.

3.3.4. Safety

Methanol presents both benefits and challenges in terms of health, safety, and environmental considerations [1]. Safety guidelines and regulations for the use of methanol onboard ships have already been developed [47]. In essence, methanol is handled more similarly to gasoline than to diesel fuel. In the following paragraphs, topics such as methanol fire, spills, and on-board transportation will be analysed.

Fire

Measures must be taken to prevent and contain fires in the case of methanol. Methanol can also form explosive mixtures in the air and is highly flammable, burning at a low temperature, with a non-luminous, clear blue flame, difficult to detect in bright light, and a smokeless combustion [1]. Due to its low flashpoint, methanol accumulates close to the ground and remains concentrated in enclosed, poorly ventilated spaces [47]. As less heat release and transfer are noted in methanol than in gasoline fires, methanol is considered a safer fuel [1]. Lastly, methanol fires are extinguished with water- or alcohol-resistant foams.

Exposure to methanol is hazardous and can occur through inhalation, contact with the skin or eyes, or ingestion. [47]. As the Methanol Institute reports, ingesting over 20 mL of methanol can be fatal, while even smaller quantities have the potential to cause permanent blindness. Hence, specific safety measures can prevent the formation of methanol vapors and support the installation of necessary ventilation, leak detection systems, heat detection and fire extinguishing equipment. Measures to prevent methanol fires in a marine environment were established in 2020 by the IMO in the ”Interim Guidelines for the Safety of Ships Using Methyl/Ethyl Alcohol as Fuel” [50]. Methanol’s safe handling is well-established in the marine industry, having extensive experience managing its global transportation.

Spills

Considering that methanol is toxic to humans, marine crews must receive proper training on managing a methanol leak [47]. Hence, adequate precautions are necessary when handling and dispensing methanol. Regarding environmental effects, methanol is water-soluble (entirely dissolving in water) and biodegradable, [1, 73]. Compared to heavy fuel oil (HFO), methane and ammonia, methanol is much less toxic to marine life [47]. In the event of a spill, the impact on marine life is expected to be temporary and completely reversible. Methanol quickly disperses to low concentrations upon release, allowing natural microorganisms to break it down within a brief time frame [1]. Significant releases rapidly dilute to non-toxic levels for marine life within a short distance [73].

One benefit of methanol is denitrification in water treatment plants, as it serves as an energy source for organisms decomposing nitrogen-containing compounds in wastewater [73]. Additionally, according to regulations, methanol does not bioaccumulate and is considered a non-environmentally hazardous substance. Unfortunately, groundwater contamination is possible if methanol is released into the soil. Its rapid biodegradability, however, makes significant accumulation in soil or groundwater unlikely.

Transportation

Several critical aspects of methanol storage and transport for ocean shipping are outlined in the Methanol Institute’s report on the safe handling of methanol [73]. Methanol transportation resembles other hydrocarbon liquids, such as crude oil, gasoline and diesel. It is usually transferred from dockside storage tanks into the sealed cargo holds of tanker ships, with delivery to the dockside facilitated by pipelines, barges, rail, or trucks. Moreover, double-hulled vessels are employed for transporting methanol, and their use is anticipated to become the norm as global production continues to rise.

Regarding the safe transportation of methanol by ship, particular precautions must be taken. This includes ensuring cleanliness to prevent contamination, installing methanol leak detection systems on ships, and supplying suitable firefighting equipment (alcohol-resistant foams). Methanol fuel tanks are always maintained under an inert vapor atmosphere [5], specifically using nitrogen [19]. This approach reduces evaporation and prevents the formation of flammable vapors. Ships using methanol as fuel need enough storage onboard to provide inert gas for purging fuel and bunkering lines. They must keep the tanks inert during trips and ensure safe conditions in port for up to two weeks [5]. This can be achieved with stored nitrogen or an onboard generator, creating gas with no more than 5% oxygen and keeping the tank vapor spaces below 8% oxygen [19, 5]. Safety measures should also be established to protect the crew and prevent reverse flow in piping systems. Lastly, equipment compatible with methanol handling, such as pumps, piping, hoses, and gasket materials, is necessary [73].

Methanol Reforming Processes

In this part of the chapter, Section 3.4 introduces the operating principles, conditions, and catalytic systems of the studied reforming processes. The focus is exclusively on endothermic processes, as the aim is to utilize waste heat from the SOFC. Consequently, three key methods are examined: Methanol Decomposition, Methanol Steam Reforming, and Autothermal Reforming of Methanol. Each process is evaluated in Section

3.5 based on criteria such as conversion and hydrogen yield, CO selectivity, process and equipment requirements, and catalyst technology. A comparative analysis is then performed to highlight the strengths and weaknesses of each method, aiming to determine the process that best suits this thesis project. By understanding these processes, hydrogen production from methanol can be optimized for both energy efficiency and integration with SOFC systems.

3.4. Processes

3.4.1. Methanol Decomposition

Methanol Decomposition (MD) is an endothermic reaction, decomposing methanol to H_2 and CO, as described by Equation 3.1 [24]:

$$\mathrm{CH_3OH} \leftrightarrow \mathrm{CO} + 2\mathrm{H_2} \quad \Delta H^o = 90.1 \text{ kJ/mol} \tag{3.1}$$

This reaction occurs at 200-400°C and atmospheric pressure [64, 9]. Liu et al. [64] emphasize that methanol decomposition is a promising method for hydrogen production, as it can achieve complete conversion at 200°C under atmospheric pressure. However, its reaction kinetics are considerably slower compared to reforming and oxidation processes [34]. Moreover, MD is applicable to recover waste heat at around 200°C from industry processes [101, 9].

MD catalysts include palladium (Pd), platinum (Pt), and metals such as nickel (Ni), ruthenium (Ru), and rhodium (Rh) [34]. Among these, Pd catalysts are the most widely used and are supported on oxides such as zirconium dioxide (ZrO_2), praseodymium(III) oxide (Pr_2O_3), and cerium(IV) oxide (CeO_2), showing high selectivity at lower temperatures. Pt catalysts, on the other hand, present strong activity and stability.

3.4.2. Methanol Steam Reforming

Steam Reforming of methanol is an endothermic process of methanol and water vapor. The chemical reactions occurring are presented as follows:

$$\mathrm{CH_3OH} + \mathrm{H_2O} \leftrightarrow \mathrm{CO_2} + 3\,\mathrm{H_2} \qquad \Delta H^\circ = 49 \text{ kJ/mol} \tag{3.2}$$

$$\mathrm{CH_3OH} \leftrightarrow \mathrm{CO} + 2\,\mathrm{H_2} \qquad \Delta H^\circ = 90.1 \text{ kJ/mol} \tag{3.3}$$

$$\mathrm{CO} + \mathrm{H_2O} \leftrightarrow \mathrm{CO_2} + \mathrm{H_2} \qquad \Delta H^\circ = -41.4 \text{ kJ/mol} \tag{3.4}$$

Reaction 3.2 is the key reforming process that facilitates the stoichiometric conversion of methanol into hydrogen. It effectively combines the contributions of methanol decomposition (3.3) and the water-gas shift reaction (WGSR) (3.4) [57]. The MSR reaction is a complex heterogeneous catalytic reaction, influenced by the reactor structure and catalyst [63]. The reaction occurs at temperature ranges of 200–300°C and pressure 1–5 bar and produces high hydrogen yield (70–74%), CO_2 yield of around 22-25% with low CO formation (<1%) [57]. The methanol reforming conversion decreases with the increase of pressure but remains above 98% even at pressures above 20 bar at H_2O/CH_3OH molar ratio higher than 1.5 [105]. As an endothermic process, the process is safer [57]. Additionally, the reaction necessitates a comparatively low molar ratio of water to carbon. The MSR process is widely used due to its efficiency in producing high-purity hydrogen [57] and the production of a greater number of moles of hydrogen per mole of methanol than the other oxidation processes [34]. More specifically, the energy losses are approximately 15-25% during the conversion of methanol to hydrogen and CO_2 [74]. While the MSR process offers easier temperature control compared to other processes, additional heat input is necessary to advance the reaction [34]. Lastly, it is generally a slow process during start-up [34].

The MSR process stands out among hydrocarbon reforming processes due to its high energy density and relatively low reaction temperature [57]. As methanol has a hydrogen-to-carbon (H/C) molar ratio of 4:1, it offers a significant advantage in hydrogen production. The lack of carbon-carbon (C—C) bonds minimizes the possibility of coke formation, a common issue with hydrocarbons such as gasoline and diesel. Due to this structural simplicity, MSR is more thermodynamically favorable. However, as discussed earlier, MSR is a kinetically comparatively slow process and thus requires residence times of approximately 1 second.

Regarding catalysts, the MSR process utilizes various catalysts, with Cu-based and Pd-based catalysts most widely used [34]. Copper-based catalysts (e.g., Cu/ZnO), are highly active and selective for CO_2 and H_2, and are often enhanced with promoters and rare earth metals. Palladium-based catalysts (e.g., Pd/ZnO), offer better thermal stability and are favored for CO_2 production, with the Pd-Zn alloy improving performance. The most widely used commercial catalyst for methanol steam reforming is $Cu/ZnO/Al_2O_3$ [57].

3.4.3. Autothermal Methanol Reforming

Autothermal Reforming (ATRM) is a combination of steam reforming and partial oxidation (POM), balancing heat generation and consumption. The reaction occurring is the following, where n is the ratio between oxygen and methanol fed to the reaction:

$$\begin{aligned} \mathrm{CH_3OH} + (1-2n)\mathrm{H_2O} + n\mathrm{O_2} &\leftrightarrow (3-2n)\mathrm{H_2} + \mathrm{CO_2} \\ \Delta H^\circ &= (-241.8(2n) + 49.5) \text{ kJ/mol}, \quad 0 \leq n \leq 0.5 \end{aligned} \tag{3.5}$$

ATRM operates at 200–350°C, with moderate hydrogen yield (55–60%) with CO formation (around 2%) [57]. It is proposed that the rate of the ATRM process equals the sum of the rates of POM and MSR reactions. Since air and water are supplied to the reactor in this process, the reaction can take place in compact and simple reactor designs [57, 34] thus reducing the complexity of the heat management, leading to faster response times. The reaction theoretically runs thermo-neutrally, neither using nor producing external energy [34]. As a result, ATRM is more efficient and with better hydrogen selectivity compared to POM. At the same time, ATRM has a better dynamic response compared to MSR and can accommodate a wider range of fuels.

ATRM requires catalysts active for the partial oxidation of methanol and methanol steam reforming under both oxidation and reduction conditions [57, 34]. Copper-based catalysts, such as Cu supported on CeO_2 and doped with ZrO_2, are commonly used due to their high activity. However, they are prone to sintering, leading to deactivation of the catalyst over time [34]. Good activity is also noticed in zinc-based catalysts, including zinc–chromium oxide ($ZnO\text{-}Cr_2O_3$) and zinc–zirconia ($ZnO\text{-}ZrO_2$), with specific supports enhancing methanol conversion or hydrogen selectivity. Moreover, catalysts such as copper–manganese oxide (CuO/MnO) and copper–zinc oxide (Cu/ZnO) have been investigated and demonstrate high methanol conversion as well. Temperature control is critical in ATRM due to the differing reaction rates of the endothermic steam reforming and exothermic methanol oxidation reactions [34, 57].

3.5. Comparison of Reforming Methods

In 2022, Garcia et al. [34] published an analytic review of hydrogen production from methanol, highlighting the aforementioned four key thermochemical conversion pathways. Figure 3.3 presents the summary of their operational conditions, reactants and products.

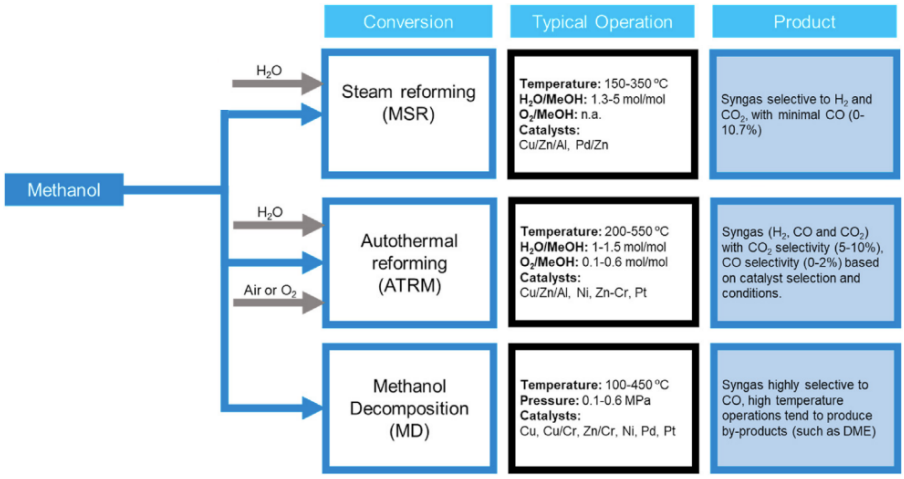

Figure 3.3: Overview of thermodynamic processes for hydrogen production from methanol [34].

Garcia et al. [34] outline four essential criteria for evaluating methanol reforming processes: conversion and hydrogen yield, CO selectivity, process and equipment technology, and catalyst technology. These aspects provide a comprehensive basis for comparison, highlighting the advantages and limitations of each process. The following sections discuss these criteria in detail.

Conversion and Hydrogen Yield:
Regarding the conversion of the reactants and hydrogen production, MSR achieves high conversion efficiency. This is because it utilizes both methanol and water, leading to a higher hydrogen yield. ATRM offers improved efficiency and hydrogen concentration, due to the combination of exothermic oxidation and endothermic

reforming reactions. Lastly, although MD operates at lower temperatures, around 127°C, it is kinetically slower than MSR and POM.

CO Selectivity:
MSR is a low-temperature process with minimal CO yield and is compatible with Cu- and Pd-based catalysts. ATRM also generates high CO concentrations, necessitating additional clean-up before the syngas is used later, for example, in a fuel cell application. In MD, CO selectivity increases, and there is potential for combustion, making it unsuitable for PEMFCs due to catalyst poisoning concerns.

Process and Equipment Technology:
MSR is a well-established process with relatively simple temperature control. As it is endothermic, and it necessitates an external heat source and a steam generation unit to proceed forward. ATRM offers an improved dynamic response compared to MSR and more adaptability in supporting a variety of fuels. Moreover, it performs optimally at a thermo-neutral point, balancing heat input and output. Lastly, MD, being an endothermic process, requires an initial heat input, with early-stage adsorption onto the catalyst surface. The slowest stage in this process is the release of CO, which becomes a constraint at temperatures exceeding 127°C. Above 127 °C, the reaction rate is limited by the desorption of CO, which acts as the rate-limiting step. Strong CO adsorption on the catalyst surface hinders its release, leading to active site blockage and reduced overall methanol conversion rate.

Catalyst Technology:
MSR relies on Cu-based catalysts, which are well-developed and extensive research is going into promoters, supports, preparation methods, and reaction mechanisms. Furthermore, ATRM catalysts must be active for both steam reforming and partial oxidation, often requiring compact catalyst synthesis to enhance performance. MD primarily utilizes Cu-based catalysts, though Chromium (Cr) and other promoters can be incorporated to optimize the process.

Table 3.2 presents an overview of the processes and their performance in the aforementioned evaluation criteria.

Table 3.2: Comparison of methanol reforming processes (MSR, ATRM, and MD).

Characteristic	MSR	ATRM	MD
Conversion & H_2 Yield	High	High	Low
CO Yield	Low	High	High
Process & Equipment†	High	Medium	Low
Catalyst Technology‡	High	Medium	Medium

† *"High" under Process & Equipment indicates a well-established technology or simpler control; "Low" indicates less mature technology or greater complexity.*
‡ *"High" under Catalyst Technology indicates a widely developed and commercially available catalyst technology ; "Low" can indicate less mature catalyst technology or a scarce catalyst with greater complexity.*

Process of choice:
In this project, MSR is selected as a process for hydrogen production using methanol as a fuel. MSR stands out among the other reforming processes in terms of high hydrogen yield, low CO production, commercially available catalyst technology, and easy temperature control, making it the preferred choice for further investigation in this thesis project.

3.6. Methanol Steam Reforming

Now, the focus shifts to the MSR process as a key pathway for hydrogen production in SOFC integration. Subsection 3.6.1 presents the three reactions occurring in the MSR process, while subsection 3.6.2 discusses catalyst selection, emphasizing performance and commercial availability. Moreover, in subsection 3.6.3, the reactor requirements and design options are explored, including heating strategies and various reactor types. Subsections 3.6.4 and 3.6.5 analyze the influence of reaction parameters—such as temperature and steam-to-carbon ratio—on chemical equilibrium and product composition. Finally, subsection 3.6.6 addresses potential side reactions and their impact on hydrogen purity and reactor performance.

3.6.1. Reactions

The key reactions involved in methanol steam reforming are revisited in this section. Reaction 3.6 is the principal reforming process of the stoichiometric conversion of methanol into hydrogen and it consists of the two side reactions; methanol decomposition (3.7) and the water-gas shift reaction (3.8).

$$\mathrm{CH_3OH + H_2O \leftrightarrow CO_2 + 3\,H_2} \qquad \Delta H^\circ = 49 \text{ kJ/mol} \tag{3.6}$$

$$\mathrm{CH_3OH \leftrightarrow CO + 2\,H_2} \qquad \Delta H^\circ = 90.1 \text{ kJ/mol} \tag{3.7}$$

$$\mathrm{CO + H_2O \leftrightarrow CO_2 + H_2} \qquad \Delta H^\circ = -41.4 \text{ kJ/mol} \tag{3.8}$$

3.6.2. Catalyst

Catalysts play a crucial role in MSR technology and various types of catalysts have been developed over time. MSR is a gas-solid phase catalytic reaction, where gaseous reactants interact with a solid catalyst to facilitate the chemical reaction [44]. They are generally categorized into copper-based and noble metal-based types as highlighted by Zhang et al. [69] in their latest review on recent advances in MSR catalysts. As they mention, copper-based (e.g. $Cu/ZnO/Al_2O_3$) and palladium-based (e.g. Pd/ZnO) catalysts are the most dominant, since they are characterised by high efficiency and reliability under challenging conditions, making them preferred choices for industrial hydrogen production via MSR. Typically, catalytic activity improves with increasing water-to-methanol ratios and higher reaction temperatures, up to a specific threshold. The weight hourly space velocity (WHSV) is defined as the ratio of the mass flow rate of methanol to the mass of the catalyst, indicating how fast the feedstock is passed over the catalyst [86]. The WHSV of methanol generally ranges around 1–10 h^{-1}, highlighting the importance of carefully considering reaction conditions when evaluating MSR catalyst performance [69].

The $CuO/ZnO/Al_2O_3$ catalyst is selected for this project, to align with the kinetic model employed and due to its proven performance in MSR and widespread commercial availability [78]. Considering the real maritime application involving a superyacht, it is essential to use a catalyst that is both cost-effective [112] and readily accessible. This choice ensures that the project remains economically viable while meeting the practical demands of the application.

3.6.3. Reactor

Requirements

Design

As noted by Hu et al. [44], the MSR reactor needs to be compact, highly efficient, require minimal equipment, and be portable, with a designed power output in the kW range. The reactor design has a significant impact on the reforming performance of MSR. The reactor must exhibit high heat and mass transfer capacities for efficient methanol conversion, as well as an optimized flow pattern design. The design ensures uniform catalyst distribution in the reactor. Low pressure drop must be a design consideration, as it minimizes energy losses and improves system efficiency. At last, adequate temperature control and insulation are required as temperature variations and uneven distributions impact methanol conversion efficiency and by-product formation.

Heating

MSR is an endothermic reaction, requiring a continuous heat supply to proceed. Therefore, heat must be supplied to the reactor for the reforming reaction to occur. This is done by catalytic combustion occurring in a dedicated chamber integrated within the MSR reactor or by electrical heating. Hu et al. [44] experimentally developed both methods and their reactor design integrates catalyst combustion, providing the necessary heat for MSR. Heat is transferred through the solid structure of the reactor to the reforming chamber, where the endothermic reactions occur. This approach couples the exothermic heat release of combustion with the endothermic heat requirement of reforming. The combustion chamber is designed to burn a mixture of methanol and air, producing heat for vaporization and reforming. As noted in their publication, the heat from catalyst combustion needs to be higher than the endothermic heat required for reforming. The system is designed to achieve stable operation without external heating equipment, relying solely on catalyst combustion once the reaction is initiated. In addition, electrical heating is used for preheating during the start-up phase of the reactor before the catalyst combustion achieves a stable heat supply. Once the desired temperature is reached, the electric heating rod is stopped, and catalyst combustion becomes the only heat source.

In another study, Mei et al. [68] developed a microchannel reactor utilizing electrical heating for a constant heat supply to MSR, achieving a conversion rate of 65–75%. Their experimental results and simulations revealed that modifying the channel structure improved the uniformity of the temperature distribution within the reactor. Lastly, Zhang et al. [113] developed a tubular reactor incorporating both internal and external electrical heating. Their experimental study showed that variations in the design of the internal heating fins influenced the methanol conversion rate. Overall, it is evident that MSR requires a constant heating feed and this can be achieved with different methods.

Types of Reactors

Fixed Bed Reactors

Traditional MSR reactors typically feature a tubular design with a packed-bed configuration, where catalyst particles are packed into the reactor [34]. Fixed bed reactors are primarily used in MSR not only for hydrogen production but also for the catalyst development for this process [57]. However, these reactors can experience inefficient heat transfer and high pressure drops. The latter requires more energy to maintain the methanol and water flows, while poor heat transfer may result in local temperature variations that reduce reactor efficiency. Fixed-bed reactors generally have a lower catalyst deactivation rate than other reactor types, though they require higher operating temperatures to achieve 95% methanol conversion. Additionally, the catalyst particle size plays a crucial role in the performance, since it affects pressure drop and mass transfer. Smaller particles improve catalytic activity but can lead to excessive pressure drops. Thus, an optimal catalyst size exists to balance activity and pressure.

Various conventional MSR reactors have been developed to address these limitations, such as coil-based, rectilinear channel, pinhole, and radial reactors [34]. Coil-based reactors improve heat transfer but suffer from high pressure drops. Rectilinear channel reactors reduce pressure drop but struggle with poor mass distribution and lower methanol conversion. Pinhole designs achieve high conversion rates with lower pressure drops but require complex control systems. Lastly, radial reactors are particularly effective for MSR because their design allows for a larger sectional area as the product gas exits, reducing pressure drop.

Other Reactor Types

Microreactors, featuring sub-millimeter channels, offer enhanced heat and mass transfer, precise residence time control, and minimal pressure drop due to their high surface area-to-volume ratio [34, 57]. Their compact design—up to five times smaller than conventional reactors—makes them ideal for portable and automotive applications. It offers fast thermal response, safe operation, and cost-effective mass production. Other innovative reactor designs include monolithic, metallic foam, and wall-coated heat exchanger reactors [57]. Monolithic reactors, typically ceramic or aluminum-based, provide high mechanical strength and low pressure drop but suffer from limited thermal conductivity. Metallic foams improve heat transfer and shock resistance, though uniform catalyst coating remains challenging. Wall-coated heat exchanger reactors, functioning as scaled-up microchannels, deliver low pressure drop, reduced gas channeling, and fast transient response, making them promising for automotive use.

Reactor of choice

In this project, a multi-tubular fixed-bed reactor was selected due to its established reliability, lower catalyst deactivation rates, and proven performance in hydrogen production. It will be externally heated by circulating a hot fluid through the reactor tube, ensuring uniform heat distribution and enhancing reaction kinetics. This approach optimizes efficiency in the MSR process.

3.6.4. Reaction Rate and Chemical Equilibrium

The reactions occurring in MSR are described in subsection 3.6.1 and they consist of methanol decomposition, steam reforming and water gas shift reaction. In 2023, Hu et al. [44] experimentally evaluated an MSR reactor designed to supply fuel for a kW-class SOFC. The reactor integrated catalyst combustion, vaporization, and reforming processes to provide the necessary fuel without requiring additional heating equipment. In their study, they analysed the specific concentrations of the gas product of MSR and explored the effects of different fuel compositions, particularly varying concentrations of CO and CO_2, on the performance and durability of SOFCs. Figure 3.4a shows the reaction rate of the three dominant reactions as a function of the reaction temperature (ranging from 100–300 °C) for a molar ratio of steam to carbon (S/C) equal to 1.2. As shown, as the reaction temperature increased, the reaction rates of MSR, MD, and WGS all rise, with MSR experiencing the most significant increase, 100 times higher than MD and 10^5 times higher than WGS. In other words, the majority of reactants participate in the MSR reaction. When the temperature exceeds 227 °C, the reaction rate increases sharply.

Figure 3.4b, on the other hand, presents the reaction rates of the three main reactions as a function of the molar S/C at 250°C. Among the three reactions, WGS exhibits the lowest reaction rate, nearly negligible compared to MSR and MD. As a result, the influence of S/C on WGS was neglected in their study. The reaction rate of MSR increased with the S/C ratio, initially rising sharply before gradually slowing down and the highest MSR reaction rate was observed within the S/C range of 0.9–1.4. In contrast, the reaction rate of MD decreased as the S/C ratio increased. When S/C exceeded the theoretical ratio of MSR (S/C = 1), the decline in MD reaction rate became less pronounced, indicating a reduction in the amount of methanol consumed in time. The Liquid Hourly Space Velocity (LHSV) is defined as the ratio of the feed volumetric flow rate to the volume of reactor or catalyst, indicating the residence time of reactants in a reactor [23].

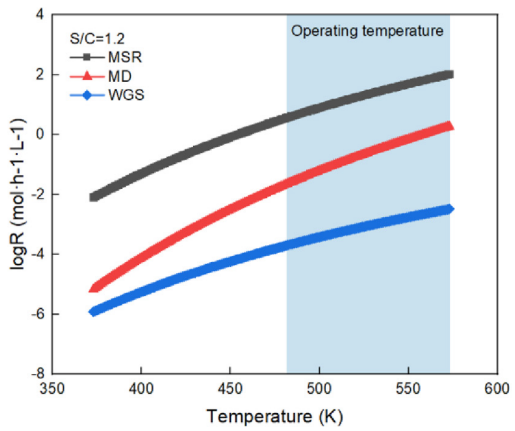

(a) Chemical reaction rates as a function of the reaction temperature for a S/C ratio of 1.2.

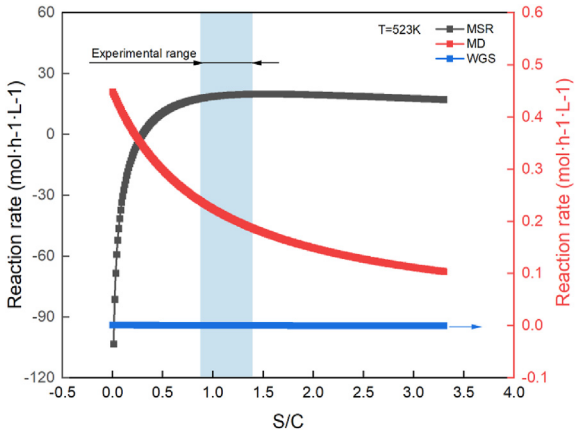

(b) Chemical reaction rates as a function of S/C molar ratio at 523K.

Figure 3.4: Chemical reaction rates as a function of S/C and temperature, with a catalyst composition of 65-70% CuO, 15-20% Al_2O_3, 15% Zn and rare earth and LHSV $\leq 3h^{-1}$ [44].

The researchers [44] also explain that the equilibrium constants of MSR, MD, and WGS are significantly larger than those of their reverse reactions (r-MSR, r-MD, and r-WGSR), as illustrated in Figure 3.5. Consequently, the reverse reactions are not considered in their study. It is further noticed that the equilibrium constants of all three reactions increase with temperature, with the MD reaction exhibiting the fastest increase. As a result, higher temperatures lead to greater CO formation in the reforming gas. The product composition as a result of the reaction conditions is discussed in subsection 3.6.5.

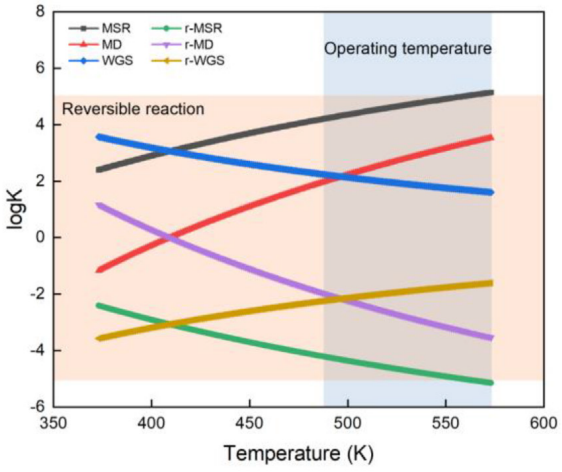

Figure 3.5: Chemical reaction equilibrium constants as functions of the reaction temperature for the three reactions of MSR [44].

3.6.5. Product Composition

Water/Methanol Ratio

Figure 3.6 presents the equilibrium gas composition of the reformed gas product of MSR as a function of the H_2O/CH_3OH molar ratio at 220°C and 5 atm by Kundu et al. [57]. The CH_3OH concentration rapidly drops

to nearly zero, indicating complete conversion at low molar ratios. As expected, the steam concentration increases with the water/methanol ratio, as more water is introduced into the system. The H_2 yield is highest at low water/methanol ratios (around a ratio equal to 1) and decreases as the ratio grows, suggesting that excessive steam concentration suppresses hydrogen production.

Water influences the selectivity of hydrogen as a reactant in MSR when it is not present in excess of the stoichiometric ratio. If water is abundant, its impact is minimal [57]. Since the presence of steam favors the WGSR, the CO_2 concentration increases with the water/methanol ratio. Eventually, it stabilizes, possibly when the WGSR reaches equilibrium or when most CO has been converted to CO_2. As can be seen, CO peaks at low ratios and then declines due to the WGSR. Overall, a H_2O/CH_3OH molar ratio of 1.5–2 is recommended for lower CO concentrations and higher methanol conversion and hydrogen yield. This is consistent with the experimental findings of Hu et al. [44], which report that within an S/C range of 1.1–1.3, the methanol conversion rate exceeds 85%.

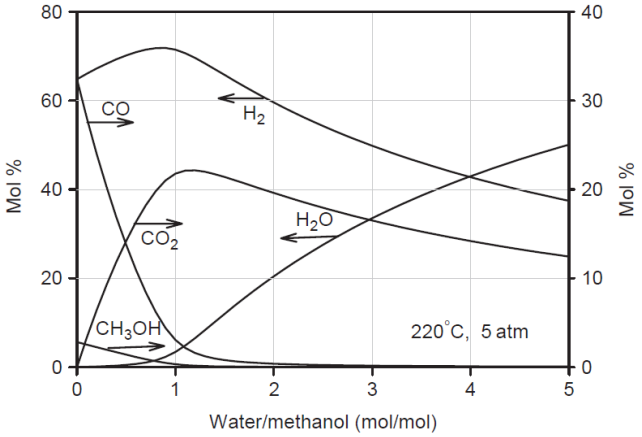

Figure 3.6: Equilibrium gas composition of the reformate gas from MSR [57].

Temperature

The reforming temperature's role in the product composition is evident in the experimental results of Hu et al. [44]. As a part of their results, Table 3.3 presents the effect of temperature on the composition of the reformate gas and the methanol conversion rate, highlighting variations in the concentrations of H_2, CO, methane (CH_4), and CO_2 under low and high-temperature conditions. The table highlights the effect of temperature on product distribution due to MD and MSR activation. As can be seen, at higher temperatures the methanol conversion rate is higher, increasing from 91.75% at low temperatures to 95.03% at high temperatures, as both MD and MSR reactions are thermally activated. The concentrations of H_2 and CO_2 decrease with the rise of temperature, while CO levels increase. This is because of the higher equilibrium constant of MD, which enhances CO formation while limiting MSR. The presence of CH_4 remains minimal for both conditions (at levels close to the detection limit of the gas chromatograph), while trace amounts of ethene (C_2H_4) and ethane (C_2H_6) are also observed. Overall, the data shows that temperature significantly influences reactor performance, with higher temperatures promoting methanol conversion but also increasing CO production while reducing H_2 and CO_2 concentrations.

Table 3.3: Gas composition and methanol conversion rates during MSR at 272.6°C and 287.7°C, based on a S/C ratio of 1.2, LHSV of 0.6 h^{-1} and with a catalyst composition of 65-70% CuO, 15-20% Al_2O_3, 15% Zn and rare earth as reported by Hu et al. [44].

Temperature (°C)	Gas composition (%)						Methanol conversion rate (%)
	H_2	CO	CH_4	CO_2	C_2H_4	C_2H_6	
272.6	72.45	5.23	0.00	20.35	0.001855	0.00228	91.75
287.7	72.12	6.12	0.02	19.82	0.000349	0.001472	95.03

Diving into the CO production, Figure 3.7 presents the equilibrium concentration of CO, as a product of MSR, as a function of the inlet H_2O/CH_3OH molar ratio for different reaction temperatures at the pressure of 2 atm

[57]. The graph illustrates that as the H_2O/CH_3OH ratio increases, the CO concentration in the dry hydrogen mixture decreases, a trend that aligns with the findings presented in Figure 3.6. This occurs due to the WGSR, which promotes the conversion of CO into CO_2 when excess water is present. Additionally, temperature has a significant impact on the CO concentration [44]. At higher temperatures (350 °C), CO levels remain relatively high across all ratios, whereas at lower temperatures (150–200 °C), the concentration drops significantly [57]. The logarithmic scale of the y-axis further emphasizes the sharp decline in CO concentration at higher water/methanol ratios, particularly at lower temperatures. This is justified by the fact that the WGSR is an exothermic reaction and is more favorable at lower temperatures. When the water/methanol ratio exceeds 3–4, CO levels can fall below 0.1 mol%, especially at temperatures below 200 °C. This is particularly relevant for fuel cell applications, where CO must be minimized to prevent poisoning effects.

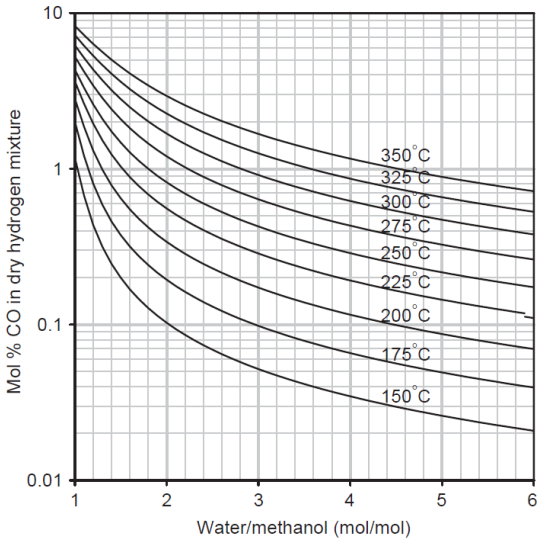

Figure 3.7: Equilibrium CO concentration as a function of the molar water/methanol feed ratio for different reaction temperatures and at the pressure of 2 atm [57].

3.6.6. Side Reactions

In the experimental study of Hu et al. [44] mentioned earlier, the composition analysis of the reformate gas from MSR revealed the presence of CH_4, C_2H_4 and C_2H_6. A series of experiments resulted in the reforming gas composition presented in Table 3.4.

Table 3.4: The reforming gas experimental composition at a temperature range of 249.85 - 279.85 °C, S/C ratio from 0.9 - 1.4, LHSV of 0.4 - 0.6 h^{-1} and with a catalyst composition of 65-70% CuO, 15-20% Al_2O_3, 15% Zn and rare earth as reported by Hu et al. [44].

Gas composition	H_2	CO_2	CH_4	CO	C_2H_6	C_2H_4
Value range	75.0-70.0%	22.0-18.0%	0.3-0.0004%	8.0-3.0%	0.005-0%	0.005-0%

Methane is formed through the methanation reactions occurring within the reforming reactor (Equations 3.9 and 3.10). These are highly exothermic reactions. As a result, their equilibrium shifts at higher temperatures, reducing methane formation. However, within the reforming reactor's operating temperature range of 250–280°C, methanation still occurred as a side reaction. The methane concentration in the reforming gas was still low, between 0.0004% and 0.3%, making its precise quantification challenging due to measurement limitations. The scientists also mention that localized temperature hotspots, influenced by factors such as the S/C ratio, LHSV (the higher LHSV, the shorter residence time of reactants in the reforming reactor), and airflow dynamics, can promote methanation. While the primary goal of MSR is hydrogen production, the study underlines the importance of considering side reactions, such as methanation, and the presence of methane as a byproduct to optimize reactor performance and hydrogen yield.

$$\mathrm{CO} + 3\,\mathrm{H_2} \leftrightarrow \mathrm{CH_4} + \mathrm{H_2O} \tag{3.9}$$

$$\mathrm{CO_2} + 4\,\mathrm{H_2} \leftrightarrow \mathrm{CH_4} + 2\,\mathrm{H_2O} \tag{3.10}$$

The researchers highlight that C_2H_4 and C_2H_6 may be intermediate products of MSR. Their formation reactions are shown below in Equations 3.11 and 3.12 and both reactions require high temperatures. During their measurements, the levels of C_2H_4 and C_2H_6 were more than ten times different from the standard gas, making it challenging to differentiate from gas chromatograph errors.

$$2\,\mathrm{CH_4} \leftrightarrow \mathrm{C_2H_6} + \mathrm{H_2} \tag{3.11}$$

$$\mathrm{C_2H_6} \leftrightarrow \mathrm{C_2H_4} + \mathrm{H_2} \tag{3.12}$$

3.7. Conclusion

Methanol is a strong candidate for maritime decarbonization due to its low emissions, liquid handling, and compatibility with existing infrastructure. Renewable methanol pathways further enhance its environmental appeal. Among reforming options, MSR is best suited for integration with SOFCs, offering high hydrogen yields, low CO emissions, and mature catalyst technologies. The selected $CuO/ZnO/Al_2O_3$ catalyst and fixed-bed reactor design provide reliable performance under maritime conditions. With favorable operating conditions identified, MSR is confirmed as a practical method for onboard hydrogen production, forming the basis for system modeling in the next chapters.

4

Solid Oxide Fuel Cells

Solid Oxide Fuel Cells are one of the most promising high-temperature fuel cell technologies with great potential for high-power applications and integration with intelligent automobile devices and other electronic applications [75]. This chapter presents an overview of SOFCs, focusing on the working principles, material composition, operational characteristics, and their potential for integration with MSR systems. Section 4.1 explains the electrochemical processes within an SOFC and outlines the material requirements for efficient operation. Section 4.2 highlights the advantages of SOFCs, such as high efficiency, fuel flexibility, and suitability for CHP applications, while Section 4.3 addresses the main challenges related to high-temperature operation and load flexibility. Finally, Section 4.4 explores experimental studies on the coupling of MSR with SOFCs, analyzing dynamic performance, fuel utilization, and the effects of reformate composition on the system efficiency.

4.1. Working Principles

The SOFCs are composed entirely of solid-state materials and function at high temperatures (700–1000°C), offering significant heat recovery and integration opportunities [4, 10]. The highly exothermic oxidation reaction within the SOFC generates heat, which can be utilized to drive endothermic methane or methanol reforming, enhancing overall system efficiency. For effective performance, SOFC materials must exhibit high ionic conductivity (higher than 0.1 S/cm), low porosity, and thermal compatibility with other components [10]. However, challenges include reducing operating temperatures while maintaining conductivity and optimizing electrolyte thickness (less than 50 µm) to improve efficiency and durability in stationary applications. Figure 4.1 illustrates the schematic of an SOFC with the three key components (anode, electrolyte, and cathode). As shown, oxygen from the air is reduced at the cathode, forming oxygen ions, which migrate through the electrolyte to the anode, where they participate in electrochemical reactions with fuel reactants [4, 10].

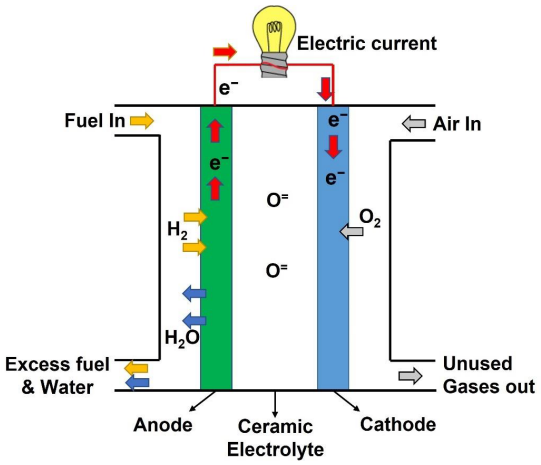

Figure 4.1: Basic schematic diagram of an SOFC [28].

Some of the early electrolyte materials used in SOFCs include yttria-stabilized zirconia (YSZ) [10] and gadolinium-doped ceria (GDC) [75]. Both materials demonstrate excellent properties and compatibility with electrode materials, with little to no thermal mismatch issues even at high operating temperatures. In principle, the electrolyte allows oxygen ions (O^{2-}) to migrate from the cathode to the anode, where they react with H_2 and/or CO to generate electricity, water (H_2O), and CO_2 [10]. The structure of the SOFC consists of two cermet porous electrodes and an oxide-conducting electrolyte, with nickel/zirconia cermet as the anode, doped lanthanum manganite as the cathode, and stabilized zirconia as the electrolyte [4]. The reactions occurring in the anode, cathode and overall are presented in Equations 4.2, 4.1 and 4.3 respectively.

$$\text{Cathode:} \quad \frac{1}{2}O_2 + 2e^- \leftrightarrow O^{2-} \tag{4.1}$$

$$\text{Anode:} \quad H_2 + O^{2-} \leftrightarrow H_2O + 2e^- \tag{4.2}$$

$$\text{Overall reaction:} \quad H_2 + \frac{1}{2}O_2 \leftrightarrow H_2O \tag{4.3}$$

4.2. Advantages

SOFCs offer several advantages, making them a competitive technology for power generation across various applications. Due to their high operational temperature, the kinetics are improved [28] and electrical efficiencies can reach 60%, or up to 70% in combined cycles with gas turbines [3, 10]. With heat recovery, overall efficiency rises to 80–90%, making them ideal for CHP systems [10, 28]. SOFCs are fuel-flexible, tolerant to impurities like CO and sulfur (S), and capable of internal reforming, reducing the need for external processing [3, 28]. They avoid costly noble metal catalysts, lowering production costs, and their modularity allows scalable deployment [3, 10, 28]. SOFCs emit few pollutants, produce stable, high-quality electricity, and can reduce ship GHG emissions by up to 34% [10, 11]. With lifespans up to 90,000 hours and quiet, efficient operation requiring minimal infrastructure, they are well suited for stationary and distributed energy systems [10]. Incentives have made SOFCs the second most widely adopted fuel cell after PEMFCs [3].

4.3. Drawbacks

Despite their advantages, SOFCs face several challenges limiting widespread adoption. Their high operating temperatures require costly, heat-resistant materials and result in long start-up times, making them unsuitable for rapid power delivery [28, 3, 75]. Prolonged thermal exposure can cause material degradation, affecting reliability and lifespan [3]. SOFCs also struggle with load flexibility, as rapid changes can induce thermal stress and accelerate degradation, posing challenges for maritime use [38]. Their lower volumetric and gravimetric power densities and larger size compared to PEMFCs further constrain their suitability in space-limited applications [28]. Lastly, effective thermal insulation and regular exhaust maintenance are crucial to minimize heat loss and ensure efficiency.

4.4. Coupling MSR with an SOFC

Methanol reforming is one of the best methods to be chosen for on-board hydrogen supply in fuel cells [57]. Managing the temperature fluctuations and mechanical vibrations is unavoidable in automotive applications where on-board hydrogen is required for fuel cells. Consequently, a primary challenge in integrating a fuel cell with a methanol reformer lies in choosing the right catalysts and reactor designs that can reliably handle these dynamic conditions.

Many researchers have studied the behaviour of a methanol reformer during cold start conditions and its dynamic performance characteristics. Emonts et al. [29] developed a compact methanol reformer for PEMFC-powered light-duty vehicles. They point out that at low load, increasing the operating temperature from 260 °C to 280 °C dramatically enhanced the methanol conversion rate, achieving complete conversion. However, further temperature increases produced only marginal gains in performance. They also noted that while higher temperatures led to elevated levels of CO emissions, these emissions decreased as the system load was increased. Wiese et al. [106] analysed the behaviour of a methanol reformer coupled with a PEMFC under quasi-static and dynamic conditions, focusing on its startup phase. They observed that the reforming reaction did not commence until approximately 10 minutes after startup. Moreover, the study revealed that the fuel supply system's reaction rate had a profound impact on the reformer's dynamic response.

From the experimental study of Hu et al. [44], mentioned earlier, the coupling operation of MSR and an SOFC and their setup are seen in Figure 4.2. The system setup included a reforming reactor, SOFC, electronic load, water circulation system, and a test island to regulate operational parameters. The experiment lasted for 74 hours in total. The researchers experimented to verify the power generation capability of the SOFC-reforming reactor system by initially operating the SOFC with pure hydrogen (anode) and air (cathode), then gradually switching to reformate gas after 10 hours of stable operation. The reforming reactor operated at 270 °C with S/C equal to 1.2, a fuel flow rate of 3.6 mL/min, with reactant and air flows of 1 mL/min and 1.85 L/min, respectively, and the gas composition was monitored throughout the experiment. Due to the limited reactant supply, the methanol solution remained in the reactor longer, resulting in a high conversion rate. At the same time, minimal fluctuations in the reforming gas confirmed a stable fuel supply.

A buffer system—with an overflow valve and stabilizer tank—regulated the reformate gas before entering the SOFC, which completed its start-up in 3 hours at a core temperature of 670 °C. After 24 hours of steady state, power generation tests at 0.7 V revealed a 12.7% drop in power generation efficiency when using reformate gas compared to pure hydrogen. Over a 74-hour test, the gas composition remained stable with only minor fluctuations in H_2, CO, and CH_4. The reactor was estimated to support a fuel cell stack of up to 1125 W, with predicted volumetric and gravimetric power densities of 303 W/L and 172 W/kg, respectively, demonstrating its feasibility for distributed power generation. Their findings are discussed in subsections 3.6.4,3.6.5 and 3.6.6.

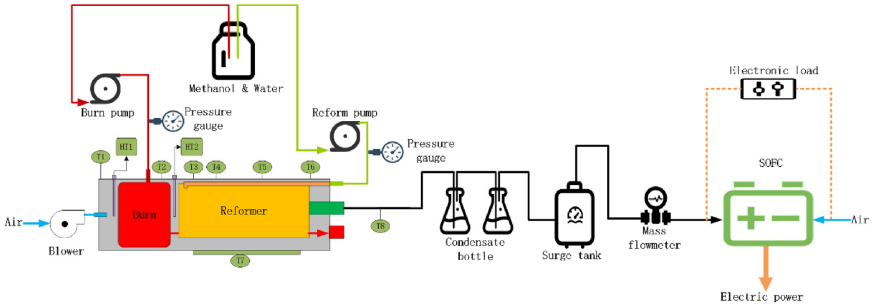

(a) Schematic design of the experimental setup.

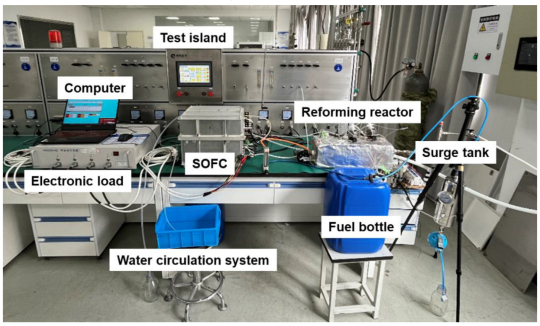

(b) Experimental devices.

Figure 4.2: Schematic design and devices of the experimental setup of Hu et al. [44] of an MSR reactor coupled with an SOFC.

In their follow-up to the previous study, Hu et al. [45] investigated the fuel adaptability of flat-chip SOFCs by using hydrogen-rich gas produced from MSR using the same previous setup. The goal was to determine the limits of using MSR-derived hydrogen-rich gas to fuel these cells. Various hydrogen-rich gas mixtures were simulated, each ensuring a hydrogen content of at least 70%, with the concentration variations of CO (0–10%) and CO_2 (0–30%). A Dt-20 SOFC stack was used in this setup, insulated, heated by a heating wire and maintained at a constant temperature of 670°C by a cooling system. The anode exhaust was analyzed using gas chromatography, while electrochemical tests evaluated the performance under different operating conditions. The researchers tested for both discharge and no discharge states of the SOFC and they point out that due to the flat-chip design, the anode reaction zone was maintained at 670°C while its ends remained at 250°C, and such steep temperature gradients can trigger side reactions.

Figure 4.3 illustrates how the composition of the SOFC anode exhaust gas changes when using hydrogen-rich fuels containing CO_2, comparing discharge and no-discharge states. Under discharge, H_2 is significantly consumed for power generation, leading to a drop in its concentration, while methanation and CO_2 reduction reactions produce noticeable amounts of CH_4 and CO. The figure also shows that the extent of these reactions

varies with CO_2 concentration, with a peak in the CH_4 production at a fuel mix of 25% CO_2/75% H_2 and maximum CO formation at 20% CO_2/80% H_2.

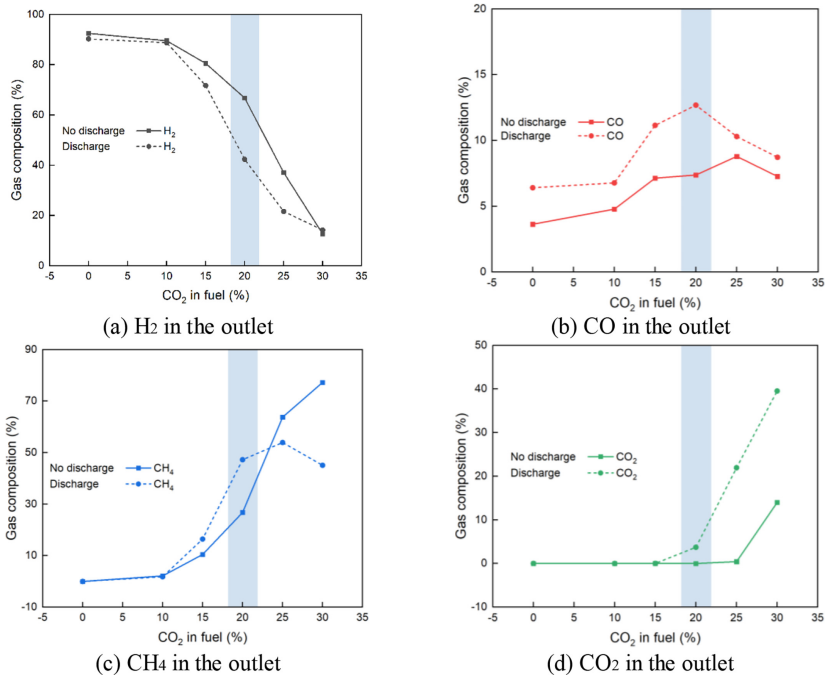

(a) H_2 in the outlet (b) CO in the outlet

(c) CH_4 in the outlet (d) CO_2 in the outlet

Figure 4.3: The anode exhaust gas composition as a function of CO_2 in the the hydrogen-rich fuel [45].

Figure 4.4 depicts the changes in the anode exhaust gas composition when hydrogen-rich gas containing CO is used. The data reveal that, along with high H_2 levels (over 82% when CO is below 10%), significant amounts of CH_4 and trace CO_2 are produced, indicating active methanation and water-gas shift reactions [45]. Notably, as the CO concentration increases, the CO_2 level initially rises, peaking at 0.2% with 6% CO—and then decreases, while CH_4 levels surge rapidly. The exhaust gas composition is similar to that observed with pure hydrogen fuel, suggesting that residual CO_2 from the catalyst material may be reduced at high operating temperatures, highlighting the SOFC's sensitivity to CO_2.

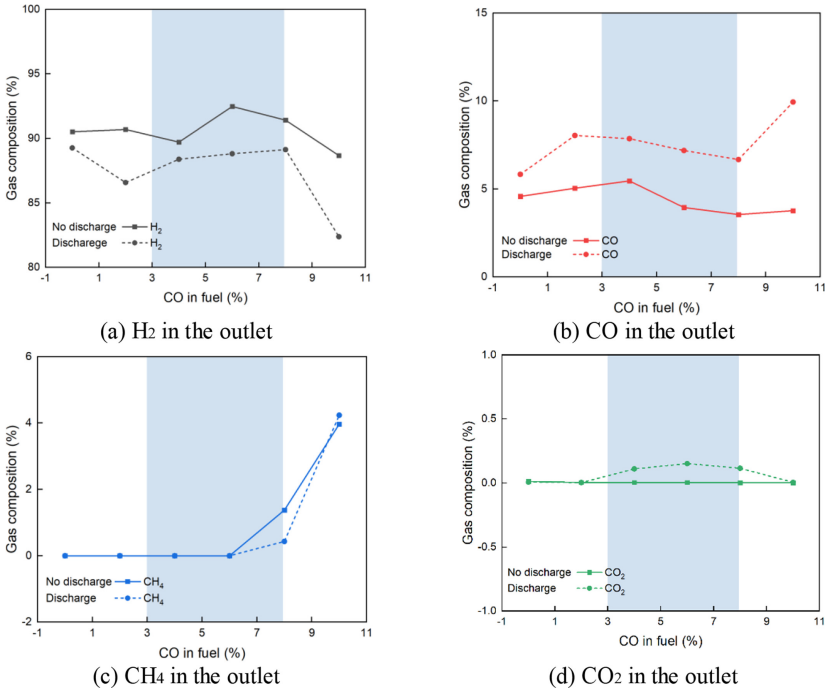

(a) H_2 in the outlet (b) CO in the outlet

(c) CH_4 in the outlet (d) CO_2 in the outlet

Figure 4.4: The anode exhaust gas composition as a function of CO in the the hydrogen-rich fuel [45].

Figure 4.5 presents the fuel utilization rate of the SOFC as a function of the CO and CO_2 percentage in the reformate gas. It shows that increasing CO_2 and CO concentrations in the fuel lead to decreased fuel utilization, directly linking fuel composition to SOFC efficiency [45]. The fuel utilization rate is higher for the percentages of CO_2 in hydrogen-rich gas compared to CO, indicating that CO has a greater impact on the stack's power generation performance. All in all, the graph underscores the critical role of CO in the overall system performance.

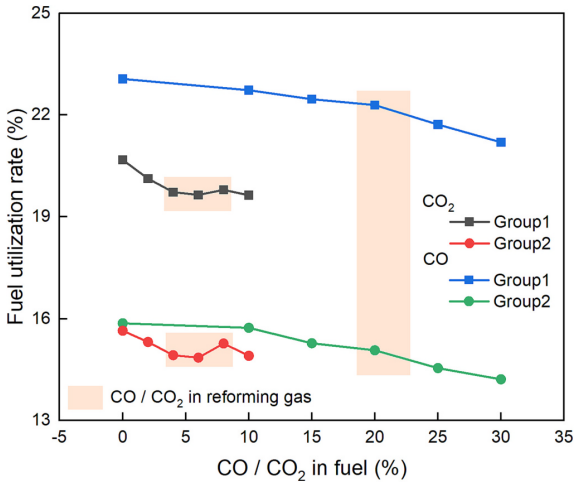

Figure 4.5: The fuel utilization rate as a function of the CO and CO_2 % in the reforming gas [45].

Long-term power generation experiments confirmed that under controlled conditions, an MSR reactor can reliably supply fuel to the SOFC [45]. However, using reforming gas as fuel results in a 0.06% decrease in the fuel utilization rate. The CO concentration predominantly influences the SOFC's fuel utilization rate and power output. Additionally, methanation occurs within the stack, especially when using hydrogen-rich fuel with CO_2—which is enhanced by the flat-chip structure's steep temperature gradients. High operating temperatures combined with CO and CO_2 also promote carbon deposition in the flat chip structure, resulting in performance degradation.

4.5. Conclusion

Solid Oxide Fuel Cells offer a high-efficiency, low-emission solution for stationary and distributed power systems, with great promise in marine applications combined with the MSR process. High-temperature operation enables the efficient integration of endothermic processes and internal reforming. However, there are still challenges of material degradation, slow start-up, and sensitivity to fuel composition. Experimental studies confirm that SOFCs can be run reliably on methanol-derived reformate gas, though small efficiency losses and increased CO sensitivity must be accepted. In conclusion, SOFCs are promising as a central component of future marine energy systems, particularly when supported by stable MSR integration and proper thermal management.

5

System Overview

This chapter presents a review analysis of system configurations combining SOFCs with other technologies to enhance energy efficiency and meet the operational requirements of maritime applications. Section 5.1 presents combined cycles with MSR-SOFC systems and outlines their performance factors and limitations in maritime environments. Section 5.2 addresses the ORC, evaluating its thermodynamic characteristics and suitability for waste heat recovery on ships. Finally, Section 5.3 addresses two literature-based integrated systems, describing their configuration, efficiency, and feasibility.

5.1. MSR-SOFC Systems and Combined Cycles

Coupling an SOFC with other bottoming cycles is proven to increase electrical efficiency through various studies. These combined cycles benefit from the high-energy waste heat of an SOFC and produce additional power. There have been many previous studies on the coupling of an SOFC and a combined cycle and some of them are presented in Table 5.1. The studies include combined cycles and technologies such as the Brayton Cycle, the ORC, supercritical CO_2 (sCO_2) Cycle, pressure swing absorption (PSA), Carbon Capture Utilization (CCU), a Stirling engine and catalytic combustion. As can be seen, two of the studies also include steam methane reforming (SMR). The presented studies focus on some KPIs to evaluate the performance of the different systems. These include energy efficiency, output power, economic performance, environmental impact, exergetic efficiency, hydrogen production rate, fuel consumption, overall system performance, system complexity, methanol conversion and thermal efficiency.

Table 5.1: Recent studies of SOFC applications with Combined Cycles.

Authors	Year	Type of System
Ma et al. [67]	2024	Methanol Reforming & SOFC & sCO_2 cycle
Aliyu et al. [4]	2023	SMR & SOFC & CCU-PSA & Steam Generation & Auxiliary power system
Li et al. [61]	2024	MSR & SOFC & Engine & ORC hybrid power generation system
Schöffer et al. [89]	2021	SMR & SOFC & sCO_2 Brayton Cycle
Rokni M. [84]	2014	Biomass (woodchips) gasification & SOFC & Stirling engine
Li et al. [63]	2025	Methanol Reforming & SOFC & Catalytic combustion

Although several concepts of the studies in Table 5.1 demonstrate promising efficiency, not all are well-suited for maritime applications. Systems involving the sCO_2 cycle — as seen in the studies by Ma et al. [67] and Schöffer et al. [89] —require operation at very high pressures, adding significant complexity and material constraints in marine environments. Similarly, Stirling engine-based systems (Rokni M. [84]) rely on external combustion and operate with considerable thermal inertia, making them less responsive to the typical ship fluctuating power demands. Systems incorporating CCU-PSA technologies (Aliyu et al. [4]) introduce additional volume, complexity, and maintenance requirements, which may be impractical in space-limited marine

settings.

The ORC cycle is chosen as the waste heat utilization cycle for this thesis project. The cycle will utilize the waste heat from the SOFC to produce additional power, meeting the superyacht's demand [83]. The high-temperature waste heat stream from the SOFC is expected to cover the thermal needs for heating the inlet streams of the SOFC and the MSR process, and the heating needs for the MSR reactor, and work as the heat source for the ORC. The cycle's compact and modular design makes it ideal for integration in space-constrained marine environments. The organic fluids used in the cycle operate at moderate pressures and do not require water treatment, reducing complexity and corrosion risks. The technology also maintains good efficiency under part-load conditions, aligning well with the variable power demands of maritime operation. Lastly, with zero emissions, the ORC is an excellent fit for maritime applications.

5.2. Organic Rankine Cycle

The Organic Rankine Cycle is a heat-to-power thermodynamic cycle technology designed for low-grade, small-scale applications such as waste heat recovery and renewable energy systems, including biomass, geothermal, and solar [17]. The upper temperature limit for the ORC is around 400°C, restricted by the thermal stability of the organic working fluids, with typical operating temperatures ranging from 200°C to 300°C. ORC systems typically recover heat from sources with low thermal energy content, often operating at temperatures below 350 °C, as commonly found in waste heat recovery applications [59].

Figure 5.1a presents a schematic diagram of the ORC and Figure 5.1b presents the temperature-entropy (T-S) diagram of the cycle [59]. In the ORC cycle, the saturated liquid working fluid (state 1) is pressurized by a pump (state 9) to reach high pressure. It then absorbs heat from the source in an evaporator (states 7–8), reaching the saturated or superheated vapor phase, and enters the expander (state 2). After expansion, the working fluid (state 3) generates mechanical work, which is then converted into electricity via the expander's shaft and a generator. The superheated fluid exiting the expander is then cooled and condensed into a saturated liquid (state 4) within the condenser. and returns to a saturated liquid (state 5), completing the cycle. The lines (7)-(8) and (5)-(6) in the T-S diagram, in Figure 5.1b, present the heat source and heat sink in the evaporator and the condenser, respectively.

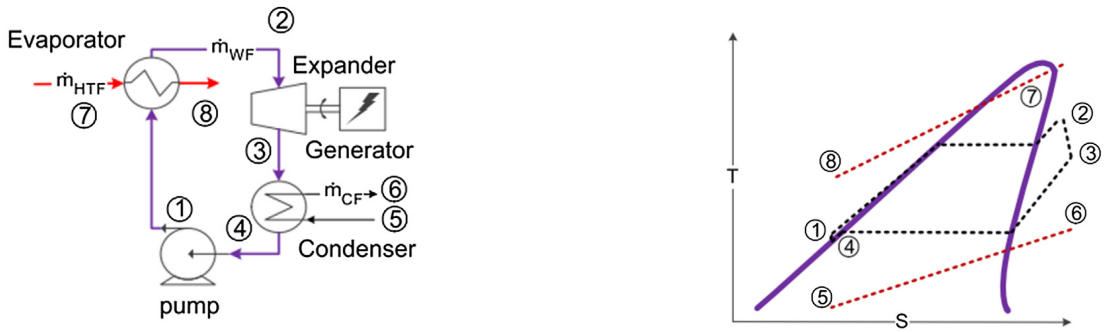

(a) The Cycle layout.

(b) The ORC T-S diagram.

Figure 5.1: Simple ORC layout and T-S diagram [59].

Regarding the ORC working fluids, 1,1,1,3,3-Pentafluoropropane (R245fa) is the most frequently used, followed by 2,2-Dichloro-1,1,1-trifluoroethane (R123) and 1,1,1,2-Tetrafluoroethane (R134a) in order of popularity [79]. Environmentally friendly working fluids for ORC systems are those with zero ozone depletion potential (ODP), low global warming potential (GWP), and low toxicity, such as the hydrofluoroolefin refrigerants trans-1-chloro-3,3,3-trifluoropropene (R1233zd(E)) and trans-1,3,3,3-tetrafluoropropene (R1234ze(E)) and natural refrigerants such as isopentane and CO_2 [80]. These fluids are preferred over refrigerants like R245fa or R123, which have high GWP or ozone-depleting effects and are being phased out. Table B.1 in Appendix B presents the characteristics of the ORC working fluids.

The ORC presents many advantages. This system is compact and operates without emitting gases such as CO, CO_2, NO_x, or other pollutants [108]. Its primary advantage is its ability to utilize a wide range of heat sources, especially when converting low-grade heat into power (electricity) [108, 79]. Another asset is the economy of scale, as the efficiency of ORC systems increases with power output due to smaller auxiliary

losses and the use of specialized, scale-appropriate equipment [79]. Compared to other waste utilization cycles, the ORC holds the most significant promise for increasing fuel efficiency, while the combined cycle delivers exceptionally high thermal efficiency [58]. As highlighted by Park et al. [79], ORC systems offer high efficiency with a relatively simple process layout. The cycle's conversion efficiency (mechanical to electrical) is reported around 70% and the overall heat to electrical power conversion efficiency was around 44% of the Carnot cycle efficiency.

5.3. Relevant Work

5.3.1. MSR-SOFC-ORC-Engine System

In 2024, Li et al. [61] published their study on the exergetic and exergoeconomic evaluation of an MSR-SOFC-Engine-ORC hybrid power generation system with methanol for a ship application. As the authors point out, the SOFC-Engine hybrid system combined with an ORC system and methanol fuel is an excellent option for marine power, thanks to its high efficiency and robust ability to handle variable loads, increased overall efficiency and significantly reduced carbon emissions. The system studied is presented in Figure 5.2.

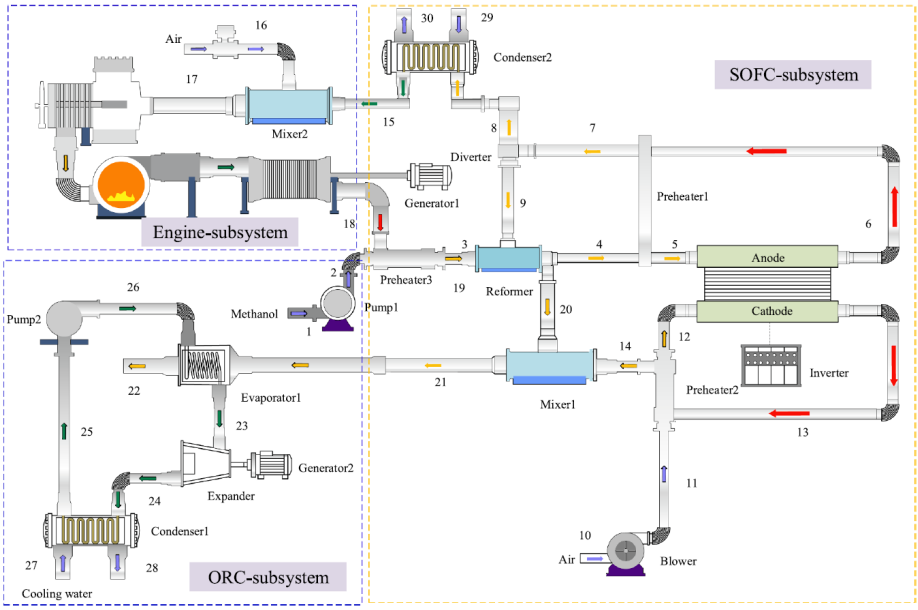

Figure 5.2: SOFC-Engine-ORC system structure diagram by Li et al. [63].

System Description

The hybrid system combines the SOFC, the engine, and the ORC to maximize power generation and overall efficiency. The system consists of the following key parts:

1. Methanol Fuel Input & Reforming: The process begins with methanol being mixed with the tail gas that is returned from the SOFC anode. Then the mixture undergoes a reforming reaction in the reformer, which converts the methanol into a hydrogen-rich gas.
2. Preheating & SOFC Power Generation: The hydrogen-rich gas is preheated before it enters the SOFC. The preheated, hydrogen-rich gas enters the SOFC, where an electrochemical reaction occurs to generate electricity. The SOFC subsystem also includes an inverter, a condenser, and a mixer.
3. Anode Tail Gas: The anode tail gas from the SOFC is separated by a diverter. Part of this gas is recycled back to the reformer to mix with fresh methanol, while the rest is cooled and then enters the engine for combustion.
4. Engine Power Generation: The remaining anode tail gas is combusted in the engine to generate further power.
5. Heat Recovery: The cathode tail gas from the SOFC is used to preheat air. The engine exhaust gas is then mixed with the SOFC cathode tail gas, which is used to drive the evaporator of the ORC system.
6. ORC Power Generation: The ORC is a simple single-stage pump ORC, where the mixed exhaust gas evaporates the organic working medium (R134a) in the evaporator. This vapor then drives an

expander to generate additional power. The expanded vapor is then condensed and pumped back to the evaporator to start the cycle again.

7. Overall System: The engine uses the fuel from the SOFC anode tail gas to generate further power. The ORC system uses the waste heat from the engine and the SOFC to generate additional power.

Methodology

The researchers conducted an energy and exergoeconomic analysis of the system. Mathematical models were developed for each component, with the SOFC modeled as a lumped parameter system and reforming based on the minimum Gibbs free energy method. The engine cycle follows the Otto cycle. Key assumptions included: air as 79% N_2 and 21% O_2, no generator/inverter losses, negligible kinetic, potential, and radiative effects, steady-state operation, ambient conditions of 25 °C and 1 bar, and no side reactions such as NO_x formation. The models were validated against experimental data, and a parametric study analyzed the effects of current density, fuel utilization, air excess, and anode reflux rate. Finally, the study evaluated the system's economic viability using the Levelized Cost of Energy (LCOE) method.

Results

The system produces a 418.16 kW total power output. The SOFC contributes 307.34 kW, accounting for 73.48% of the total production, while the engine, utilizing the SOFC's anode tail gas, generates 95.43 kW. Additionally, the ORC system recovers waste heat to produce 15.48 kW. Overall, the system achieves a power generation efficiency of 61.86% and an exergy efficiency of 58.06%.

The authors also report that the system's carbon emissions are 378.80 g/kWh, significantly lower than those of current marine diesel or LNG engines, at 772.97 g/kWh and 471.85 g/kWh, respectively. Due to methanol's renewable properties, its use creates a negative carbon benefit for the system by reducing the lifetime overall emissions. Lastly, the economic analysis revealed that the system has an LCOE of 0.2458 $/kWh, considerably higher than the 0.09 $/kWh for current marine diesel engines, mainly due to the high cost of the SOFC and its auxiliary reformer.

5.3.2. Reforming-SOFC-Heat Management System

In 2017, Zhang et al. [114] published a comparative analysis and optimization of SOFC – Combined Heat and Power systems, focusing on improving the utilization of exhaust gas energy, enhancing system performance, efficiency, and safety. Traditional systems often fail to fully exploit the high-temperature exhaust, leading to reduced fuel efficiency and potential safety concerns due to extremely high combustion temperatures in single-stage exhaust gas combustion (SS-EGC). To address this, their study proposes a Multi-Stage (MS) Exhaust Energy Recycling strategy, exploring several configurations to recover both thermal and chemical energy from anode and cathode off-gases. These include MS-EGC, Multi-stage Anode Off Gas Recovery (MS-AOGR), MS-AOGR & Cathode Off Gas Recovery (COGR), and MS-AOGR & EGC, with SS-EGC used as a benchmark. The different configurations can be seen in Figure 5.3.

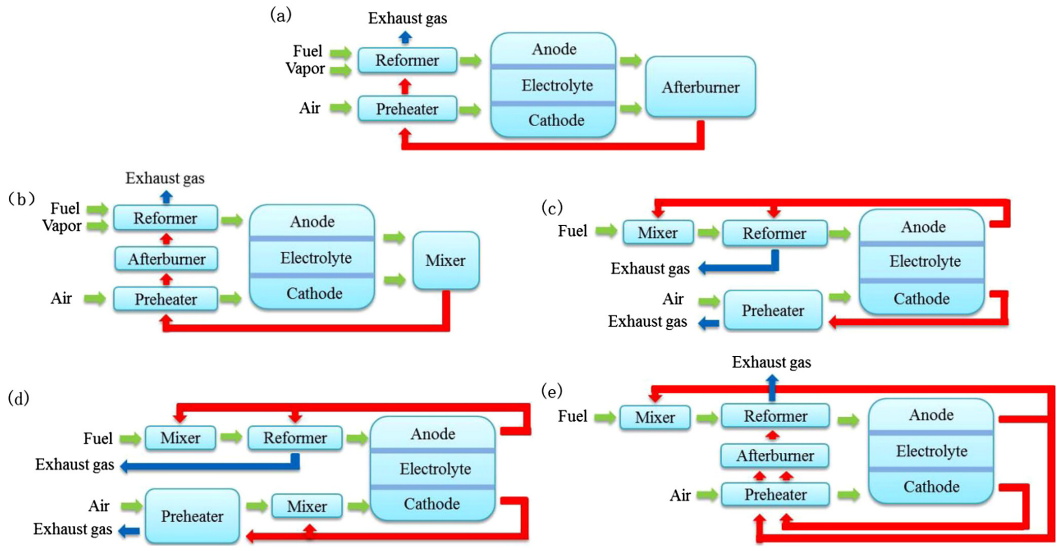

Figure 5.3: The SOFC-CHP system process with different models of exhaust gas recycles: (a) traditional single stage EGC, (b) newly designed multi-stage EGC, (c) MSAOGR, (d) MS-AOGR & COGR, and (e) MS-AOGR & EGC [114].

Methodology

The study employed an integrated methodology combining process modeling, experimental validation, and comparative analysis to develop and optimize novel multi-stage exhaust energy recycling strategies for an SOFC-CHP system. A detailed numerical model of the system was created in Aspen Plus, with a custom Fortran-based electrochemical subroutine simulating the fuel cell operation. The model is simulating a steady-state, zero-dimensional analysis. The validation was achieved by comparing simulation results with experimental data from existing systems, demonstrating strong agreement.

Subsequently, five system configurations were designed and simulated under uniform conditions to evaluate thermal and electrical performance, including four multi-stage and one traditional single-stage setup. Parametric studies explored the influence of operational variables, such as the AOGR ratio. Complementing the modeling work, experiments were conducted on a custom-built 1 kW reactor integrating catalytic combustion, steam reforming, and heat exchange. These experiments, conducted under realistic SOFC conditions, confirmed the feasibility and benefits of the proposed multi-stage designs.

Results

Among the findings, the MS-EGC design notably reduced operating temperatures from 1149 °C to 830 °C, improving safety without compromising efficiency. MS-AOGR improved electrical output by utilizing unreacted anode fuel, while MS-AOGR & COGR showed limited additional benefits. The MS-AOGR & EGC configuration emerged as the most effective, achieving a simulated 92% overall cogeneration CHP efficiency and demonstrating the best balance of electrical and thermal performance. Experimental results confirmed the feasibility of the multi-stage approach, especially the MS-EGC, affirming that early-stage thermal recovery does not hinder downstream chemical energy utilization.

5.4. Conclusion

This chapter reviewed and evaluated state-of-the-art hybrid systems integrating SOFCs and complementary technologies for performance enhancement in maritime applications. Among various combined cycles with high efficiency, the ORC is highlighted due to its simplicity, modularity, and compatibility with marine conditions. As seen from the above-reviewed research work, SOFCs can be integrated with methanol reforming and waste heat recovery subsystems to enhance overall system efficiency and reduce emissions. Motivated by these efforts, the following chapter presents the project's system, which leverages synergies in electrochemical conversion, thermal integration, and clean fuel use to offer a compelling concept for onboard energy systems in next-generation sustainable ships.

6

Basis of Design

This chapter outlines the foundational elements underlying the system design and simulation work conducted in this project. It begins by examining the operational characteristics and power requirements of the modern Feadship superyacht, where the system will be applied, identifying key conditions that influence system sizing and performance targets. Section 6.2 introduces the integrated MSR-SOFC-ORC-Afterburner system configuration, developed to meet the auxiliary energy demands with high power and heat management efficiency. Section 6.3 details the Aspen Plus modeling approach, including thermodynamic methods, kinetic implementations, and subsystem customizations. Section 6.4 summarizes the data sources, modeling assumptions, and system boundaries. Finally, Section 6.5 presents the Key Performance Indicators (KPIs) used to evaluate system efficiency, fuel and resource consumption, and operational costs across different load scenarios.

6.1. Superyacht's specifications and Power demand

The Feadship luxury motor superyacht is designed to be 84 m long and is suitable for oceangoing voyages. The dataset includes operational data such as detailed power demand profiles for various operational scenarios, such as sailing, anchoring, and harbor conditions. The yacht will primarily operate at cruising speeds between 13 and 16 knots, with a peak around 14 knots, indicating efficient, steady-state operation. Low and high speeds are rare, suggesting limited maneuvering and high-speed transit. The yacht will be seasonally repositioning with frequent transatlantic travel, from the Mediterranean,the Caribbean, and the East Coast of the United States. This supports the need for a power system optimized for fuel efficiency at cruising speeds and capable of long-range, autonomous operation. Table 6.1 presents the Feadship superyacht's specifications. The ship has an electrical azimuthing primary propulsion type, and as reported by Feadship, 10% of the time the yacht is sailing, 33% of the time is at anchor and 57% in harbour. It is assumed that the auxiliary power system is in operation for the majority (90%) of the time.

Table 6.1: Feadship superyacht's specifications [103].

Parameter	Value
Length	87.0 m
Beam	13.5 m
Draught	3.9 m
Displacement	2470 t
GT volume	3000 t
Maximum speed	18 kn
Range	5000 nm
Max propulsive power	4000 kW
Max auxiliary power	1000 kW
Mean auxiliary load	280 kW

The Figures 6.1a and 6.1b present the superyacht's total and auxiliary load profiles. As can be verified from the graphs, the ship's auxiliary demand is dominant during its operation.

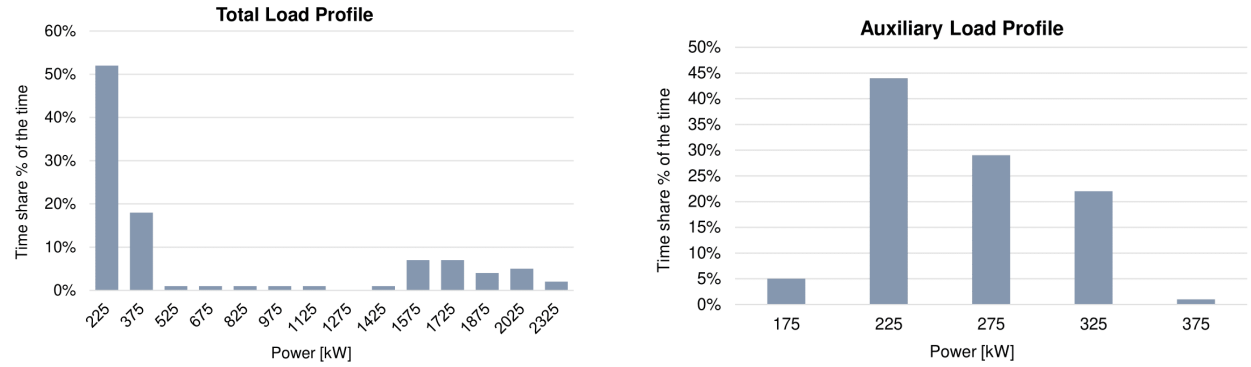

(a) Distribution of the total load profile including propulsion loads on the Feadship superyacht in operating time.

(b) Distribution of auxiliary power load on the Feadship superyacht in operating time.

Figure 6.1: Load profiles of the Feadship superyacht [103].

The system designed in this thesis project will cover a maximum power demand of 325 kW and will be modeled in three different power states of the auxiliary demand of 225 kW, 275 kW and 325 kW.

6.2. System Description

Inspired by the Li et al. [61] SOFC-ORC-coupling system and the Zhang et al. [114] heating configurations and use of an afterburner, this thesis project will analyse an MSR-SOFC-ORC-Afterburner system, presented in Figure 6.2.

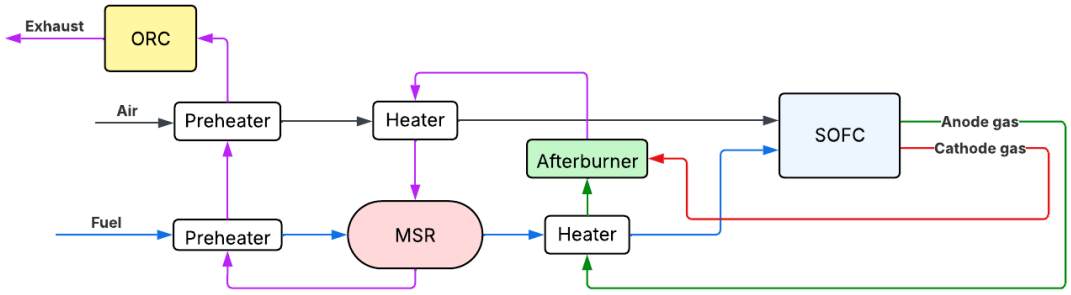

Figure 6.2: System Configuration.

6.2.1. Architecture

As illustrated in Figure 6.2, the system consists of the following key subsystems:

- **Methanol Steam Reformer (MSR):** Converts bio-methanol and water into hydrogen-rich syngas.
- **Solid Oxide Fuel Cell (SOFC):** Utilizes the reformed gas to generate electricity and heat through electrochemical conversion.
- **Organic Rankine Cycle (ORC):** Recovers thermal energy from the SOFC exhaust for additional electricity generation.
- **Afterburner and Heat Integration Network:** Enhances fuel utilization and recovers residual heat to support preheating and MSR requirements.

This configuration enables high system-wide electrical and CHP efficiency through synergistic integration of chemical, thermal, and electrical processes.

6.2.2. System Operation and Energy Flows

In this design, bio-methanol is mixed with water and reformed in the MSR reactor to produce a hydrogen-rich syngas. This gas is then fed to the SOFC, where electricity is generated through electrochemical conversion. The high-temperature exhaust from the SOFC is recovered and utilized to maximize energy recovery: (i) it supplies heat to the ORC evaporator for additional power generation, (ii) it provides the endothermic heat

required by the MSR, and (iii) it preheats the incoming air, fuel, and water streams, boosting system efficiency. To ensure complete fuel utilization, the anode off-gas is directed to an afterburner, where remaining fuel is combusted to recover residual chemical energy, and the heat generated is used to support the MSR reactor, air and fuel preheaters via integrated heaters. A Sea Water Reverse Osmosis (SWRO) unit produces the freshwater necessary for the system. The SOFC additionally supplies power for the fuel pump, air compressor, and the SWRO unit while working in cooperation with the ORC to help meet the superyacht's auxiliary power requirements. This highly synergistic configuration aims to achieve efficient energy conversion with minimal waste.

6.3. Model Development

The system model was developed in Aspen Plus, a process simulation software, using steady-state assumptions. Aspen Plus inherently solves the mass and energy balances across the flowsheet using its internal property methods and unit operation modules. For key subsystems, specific customizations were implemented to improve physical accuracy:

- **Thermodynamic Models**: Appropriate thermodynamic methods were assigned to each stream and unit operation depending on the fluid phase and composition. The methods for each chemical component are presented in Table 6.2. The Peng–Robinson equation of state offers accurate vapor-phase predictions and is ideal for reformers, gas-phase reactors, and high-temperature or high-pressure systems [65].

Table 6.2: Thermodynamic methods for each component.

Component	Method
Air	PENG-ROB
Methanol	PENG-ROB
R1233zd(E)	PENG-ROB
Water	STEAMNBS

- **Methanol Steam Reforming** : A user-defined kinetic model based on literature data was implemented in a custom Aspen Plus reactor block. This allowed the simulation of temperature - and composition-dependent reaction rates and accurate sizing of the reformer unit. The reactor sizing and pressure drop settings were also inserted in the reactor's block parameters.
- **Solid Oxide Fuel Cell**: The electrochemical performance of the SOFC was modeled by manually implementing a Fortran electrochemical model-calculating subroutine within a calculator block, accounting for activation, ohmic, and concentration losses. The anode and cathode properties, the fuel utilization, stack temperature, current density, and area were inserted into the electrochemical model. The model outputs are the SOFC voltage and generated power.
- **Heat Integration & Afterburner**: A custom heat exchanger network was designed to utilize the thermal energy from the SOFC exhaust. The recovered heat evaporates the working fluid of the ORC, heats the reformer, and preheats the feed streams. The afterburner combusts the SOFC outlet gases and generates further heat. Energy targets and feasibility were validated based on temperature pinch constraints.

6.4. Data Sources and Model Assumptions

All model parameters, including reaction kinetics, component properties, and SOFC performance data, were sourced from experimental studies and literature. Reactor sizing constraints were derived from published designs and scaled according to the system requirements. The model validation was performed for both the MSR and SOFC subsystems by comparing simulation outputs to reported experimental results under similar operating conditions. Each submodel includes assumptions, which are discussed in their respective subsections. A key overarching assumption is that the modeled system is intended for auxiliary power generation aboard a superyacht, not for primary propulsion.

6.5. Key Performance Indicators

Now that the four key aspects of the research questions (a–d) outlined in the literature background have been addressed and the system concept has been refined accordingly, the focus shifts to identifying and evaluating

the system's KPIs. These KPIs serve as the basis for assessing the system's performance, efficiency, and overall viability. The following KPIs will be evaluated for the three different power states of the yacht:

1. **System's electrical generation and CHP efficiency**
2. **SOFC and ORC efficiency**
3. **Methanol, air, and water consumptions**
4. **System's operational costs (€/year)**

6.6. Conclusion

This chapter defined the basis for modeling and evaluating an advanced integrated energy system tailored to the auxiliary demands of a superyacht. By analyzing the ship's power profile, an appropriate design was established for the modeled system. The proposed configuration integrates the MSR process, the SOFC technology, and an ORC, coupled through heat recovery and afterburner subsystems. Through detailed modeling in Aspen Plus, the system is defined with realistic thermodynamic and kinetic parameters, while remaining aligned with maritime operational conditions. These foundational elements set the stage for the modeling methods presented in the following chapter.

7

Modeling

This chapter elaborates on the modeling methodology used to simulate the MSR–SOFC–ORC system and evaluate its performance for auxiliary power generation aboard a superyacht. Firstly in Section 7.1 the system's Aspen Plus model layout is presented. Sections 7.2 to 7.6 provide a comprehensive explanation of the modeling strategy for each component: the MSR process, the SOFC, the ORC, the heat integration network, and the afterburner. Lastly, in Section 7.7, the key efficiencies studied are defined.

7.1. Overall System Model

The system Aspen Plus model is shown in Figure 7.1. The individual subsystem models are discussed analytically in the following sections of the chapter.

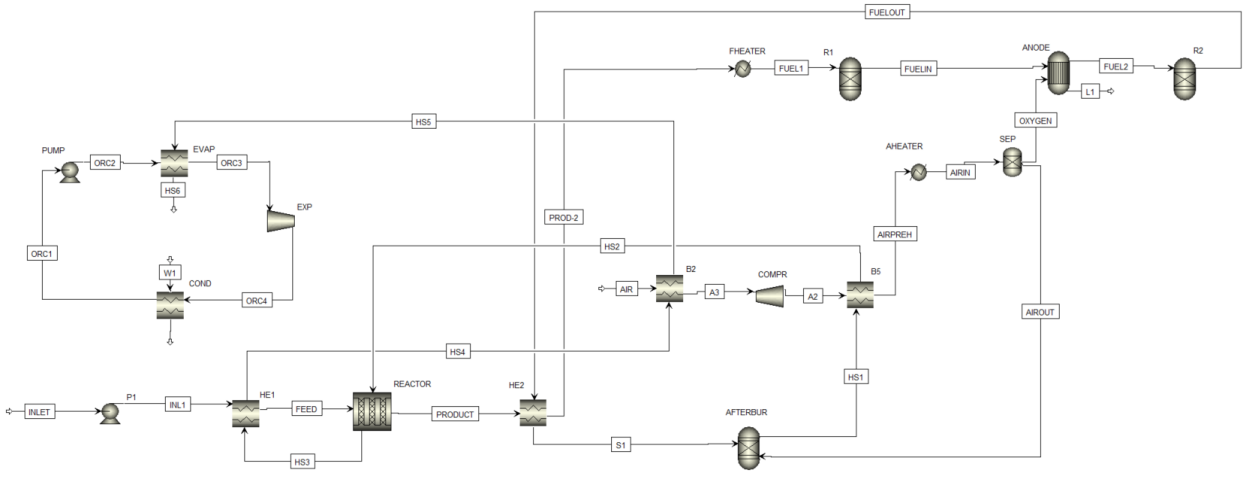

Figure 7.1: System model in Aspen Plus.

7.2. Methanol Steam Reforming

7.2.1. Kinetic Model

Özcan O. and Akın A. [78] examined the MSR kinetics over the commercial catalyst $CuO/ZnO/Al_2O_3$ (HiFUEL W220) and applied the results to simulate an integrated methanol steam reforming-high-temperature PEMFC (MSR–HT-PEM) system for portable power. Experiments were performed at 246°C and 1 atm, with methanol and water vapor diluted in nitrogen. A power-law kinetic model was developed by non-linear regression (Equation 7.1, where p_i is the partial pressure in (kPa), which exhibited an accurate prediction of the observed rate, yielding reaction orders of 0.29 (CH_3OH) and 0.09 (H_2O) and an activation energy of 65.59 kJ/mol. The kinetic model was tested for a range of temperatures from 180 to 310°C and the thermodynamically optimum temperature was 246 °C. The validated rate expression was implemented in Aspen Plus to simulate the reformer integrated with an HT-PEMFC, targeting outputs around 15 W. Their simulation results strongly

agreed with the experimental data, confirming the model's suitability for system-level performance analysis. Their model is selected as the MSR reaction kinetic model of this project since it accurately describes reaction rates under realistic operating conditions and relies on a proven $CuO/ZnO/Al_2O_3$ catalyst.

$$\dot{r}_{\mathrm{MSR}} = 53.48 \exp\left(-\frac{65.59\ \mathrm{kJ\,mol^{-1}}}{RT}\right) p_{\mathrm{CH_3OH}}^{0.29}\, p_{\mathrm{H_2O}}^{0.09} \quad (mol_{\mathrm{CH_3OH}} \cdot s^{-1} \cdot g_{catalyst}^{-1}) \tag{7.1}$$

For the kinetic model, this simplified approach was selected that represents the overall MSR reaction (Reaction 3.6). While this model does not account for CO formation, this limitation is addressed downstream, in Aspen Plus, by an RGibbs reactor, which re-establishes chemical equilibrium and generates a significant amount of CO.

7.2.2. Kinetic Model Validation

The MSR kinetic model of Özcan O. and Akın A. [78], adopted in this work, was validated against their reported experimental results and data. More specifically, the effect of varying the methanol's partial pressure on the methanol conversion was studied. Table 7.1 presents the six data sets used in the model validation. In these sets, the partial pressure of water was kept constant, the catalyst weight was equal to 50 mg, and the temperature was 246 °C. The last column of the table lists the experimentally measured reaction rate. Nitrogen was added to the inlet feed stream and served as an inert diluent to maintain a constant total pressure of 1 atm during the experiments. As the partial pressures of CH_3OH and H_2O were varied, the N_2 partial pressure was adjusted accordingly to balance the total pressure. Although present in the gas mixture, N_2 does not participate in the reaction and is not included in the rate law, indicating it has no direct effect on the reaction kinetics.

Table 7.1: MSR Kinetic Model Validation data, with catalyst $CuO/ZnO/Al_2O_3$ weight of 50 mg, at 246 °C and 1 atm [78].

Set of data	Partial pressure (kPa)			$W_{cat}/F_{CH_3OH,in}$ (kg·s·mol^{-1})	H_2O/CH_3OH molar ratio	Rate ($\times 10^{-5}$ mol$_{CH_3OH}$·s^{-1}·g$_{cat}^{-1}$)
	CH_3OH	H_2O	N_2			
1	57.09	38.63	5.61	0.99	0.66	6.24
2	50.67	38.63	12.03	1.11	0.74	6.11
3	44.26	38.63	18.45	1.28	0.85	5.78
4	37.84	38.63	24.86	1.49	0.99	5.53
5	31.43	38.63	31.28	1.80	1.20	5.39
6	25.01	38.63	37.69	2.26	1.50	5.05

A MATLAB code (see Appendix A.1) was developed to calculate the model's methanol conversion for the six different sets of data and compare them against the conversion results obtained using the experimental rates. The results are shown in Figure 7.2, and as can be seen, they are a good fit to the experimental points of $R^2 = 0.9307$.

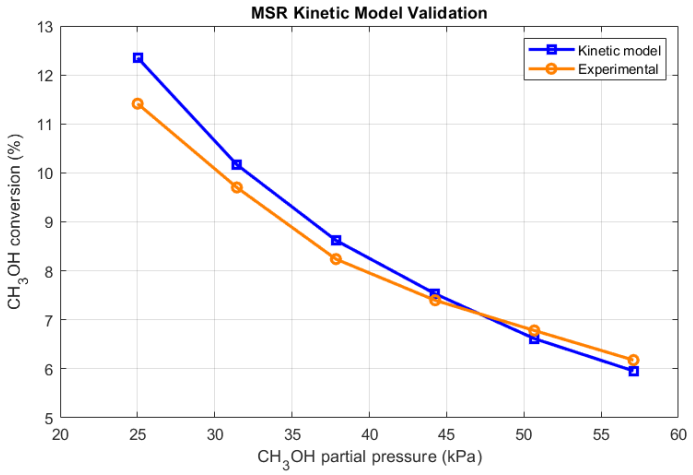

Figure 7.2: Methanol conversion as a function of methanol partial pressure in the inlet stream, at 246°C, $P_{H_2O} = 38.63$ kPa and 50mg of $CuO/ZnO/Al_2O_3$ catalyst.

To further validate the model, the composition graph was modeled using MATLAB (see Appendix A.2), as shown in Figure 7.3. The results match the researchers' reported composition graphs, which were developed in Aspen Plus.

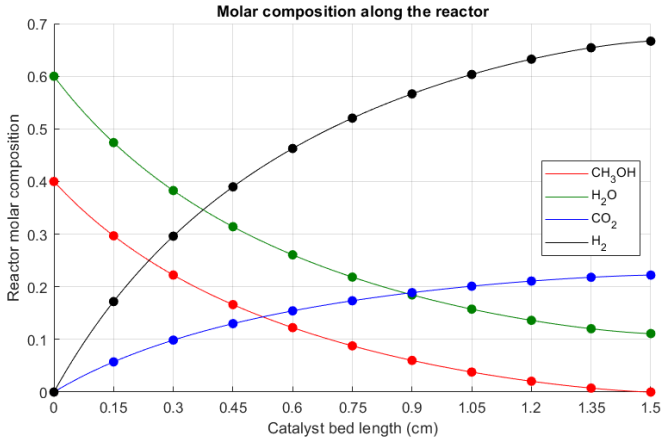

Figure 7.3: MSR components molar compositions along the catalyst bed length.

7.2.3. Aspen Plus Modeling

The MSR process was modeled in Aspen Plus using an RPlug reactor. The configuration of the MSR model is presented in Figure 7.4. The pump's function is to offset the process stream's pressure drop across the reactor. The inlet stream is a combined stream of methanol with water entering the system at ambient conditions. The stream is consequently heated by the heat utilization network and it then enters the reactor, which is externally heated by a thermal fluid. In the reactor block, reaction (3.6) is simulated, taking into account the pressure drop of the process stream and the thermal fluid, the catalyst density and void fraction.

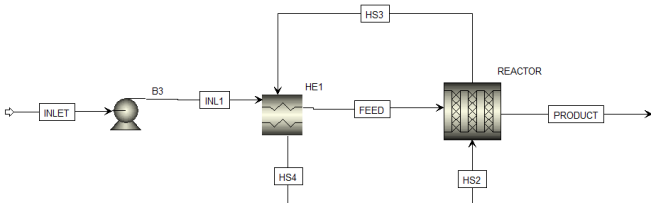

Figure 7.4: MSR Aspen Plus Model.

7.3. Solid Oxide Fuel Cell

The model used by Amladi et al. [6] is adopted for the SOFC modeling. The authors followed the model developed by Hauck et al. [40] of a reversible SOFC. Amladi et al. [6] investigated an energy storage system based on a reversible solid oxide cell (rSOC) operating with ammonia as fuel, conducting a thermodynamic analysis aimed at maximizing efficiency.

7.3.1. Assumptions

In the SOFC model, the following assumptions are taken into consideration:

1. The SOFC stack is considered to have a uniform temperature, with all reactions occurring isothermally at this constant temperature.
2. Zero-dimensional and steady state model, maintaining constant current density.
3. Due to the elevated operating temperatures of the stack, the reaction kinetics are assumed to be rapid.
4. Nitrogen in the air is considered electrochemically inert.
5. From the MSR reformate gas product, only H_2 and CO are considered electrochemically active.
6. The anode and cathode outlet streams exit at the same temperature [114].

7. The fuel and air streams do not enter the fuel cell at the same temperature, as their temperatures result from the heat utilization system's preheating. The air enters the fuel cell at a lower temperature to minimize thermal gradients within the stack. The temperature difference between the outlet and inlet temperatures was aimed to be constant, below 150 K [104] and equal to ΔT = 100 K [16].
8. All working fluids are modeled as ideal gases with no pressure drop.
9. The air molar composition was considered 79% N_2 and 21% O_2.
10. The porosity is assumed to be uniform across the full thickness of the fuel electrode in the model.
11. Constant utilisation factor [16].
12. Isobaric electrochemical reaction at SOFC inlet pressure [16].

7.3.2. Fuel and Oxygen Flows

To determine the required methanol feed rate inlet to the MSR reaction for the SOFC to reach a specified fuel utilization U_f and cell current I (A), the stoichiometry of the MSR reaction and subsequent electrochemical reactions is considered. One mole of methanol produces 3 moles of hydrogen, and each mole of hydrogen yields 2 electrons when oxidized in the SOFC. This results in a total of 6 moles of electrons per mole of methanol, leading to the following expression for the methanol molar flow rate:

$$\dot{n}_{\mathrm{CH_3OH}}\,(\mathrm{mol/sec}) = \frac{I}{6FU_f} \tag{7.2}$$

The fuel utilization factor, U_f, is defined as follows:

$$U_f = \frac{\dot{n}_{\mathrm{eq\,H_2,consumed}}}{\dot{n}_{\mathrm{H_2,inlet}}} \tag{7.3}$$

The oxygen flow necessary for the H_2 and CO reactions in the SOFC is [82]:

$$\dot{n}_{\mathrm{O_2,required}}(\mathrm{mol/sec}) = \frac{I}{4F} \tag{7.4}$$

7.3.3. Overpotential

The cell voltage has a major role in the fuel cell modeling.The cell voltage is calculated from Equation 7.5:

$$V_{cell} = V_N - V_{\mathrm{Ohm}} - V_{\mathrm{Act}} - V_{\mathrm{Conc}} \tag{7.5}$$

The reversible Nernst voltage, V_N, is calculated using Equation 7.6, where E_0 is the reversible potential in (V) at standard conditions of 1 bar, 2 represents the number of electrons produced per mole of hydrogen fuel reacted, T is the average SOFC temperature (K), R is the universal gas constant and p_i is the partial pressure of gaseous i-component (bar).

$$V_N = E_0 + \frac{RT}{2F}\ln\left(\frac{p_{\mathrm{H_2}}p_{\mathrm{O_2}}^{0.5}}{p_{\mathrm{H_2}O}}\right) \tag{7.6}$$

The reversible potential E_0, is calculated by the empirical Equation 7.7 of Yang et al. [109] used in Pianko-Oprych and Palus work on SOFC modeling in Aspen Plus [82]:

$$E_0 = \frac{4187\cdot\left(58.3 - (0.0113 + 9.6\cdot 10^{-7}\cdot T)\cdot T\right)}{2F} \tag{7.7}$$

Ohmic overpotential

The Ohmic overpotential (V_{ohm} (V)) accounts for voltage losses caused by resistance to ionic and electronic charge transport within the fuel cell components. Among these, the electrolyte's ionic resistance is significantly higher and more temperature-dependent than the electronic resistance of other materials. As a result, the electronic resistance, denoted by r_{const} ($\Omega\cdot m^2$), is assumed to remain constant. The Ohmic overpotential is calculated with Equation 7.8, where δ_{el} is the electrolyte thickness (m). The conductivity of the electrolyte is symbolized as σ_{el} (Ω^{-1} m^{-1}) and is calculated using an Arrhenius-type relation shown in Equation 7.9.

$$V_{\mathrm{Ohm}} = j\left(\frac{\delta_{\mathrm{el}}}{\sigma_{\mathrm{el}}} + r_{\mathrm{const}}\right) \tag{7.8}$$

$$\sigma_{\mathrm{el}} = \sigma_{0,\mathrm{el}}\exp\left(\frac{-E_{\mathrm{act,el}}}{RT}\right) \tag{7.9}$$

Activation Overpotentials

The activation overpotential represents the activation energy required for the reaction. It is calculated at the two electrodes, the anode and cathode. The activation overpotential at electrode i ($V_{\text{Act},i}$ (V)) is determined using the hyperbolic sine approximation of the Butler–Volmer equation, as shown in Equation 7.10. In these equations, $j_{0,i}$ ($A \cdot m^{-2}$) represents the exchange current density at the two electrodes. This is calculated with an Arrhenius-type relation as shown in Equation 7.11. The current density of the stack is represented as j ($A \cdot m^{-2}$).

$$V_{\text{Act},i} = \frac{RT}{n_i F \alpha_i} \sinh^{-1}\left(\frac{j}{2j_{0,i}}\right) \tag{7.10}$$

$$j_{0,i} = \gamma_i \exp\left(\frac{-E_{\text{act},i}}{RT}\right) \tag{7.11}$$

Concentration Overpotentials

The concentration overpotential accounts for voltage losses arising from limited diffusive mass transport within the electrodes. Because mass transfer is slow, the species concentrations at the reaction sites—also known as triple-phase boundaries (TPBs)—differ from those in the bulk flow. This concentration gradient leads to a voltage difference, defined as the concentration overpotential, denoted by $V_{\text{Conc},i}$ (Equations 7.12 and 7.13), for each electrode i. The indices FE and AE represent the fuel electrode, the anode, and the air electrode, respectively, as the cathode.

$$V_{\text{Conc,FE}} = \frac{RT}{2F} \ln\left(\frac{p_{\text{H}_2,\text{bulk}} \cdot p_{\text{H}_2\text{O,TPB}}}{p_{\text{H}_2,\text{TPB}} \cdot p_{\text{H}_2\text{O,bulk}}}\right) \tag{7.12}$$

$$V_{\text{Conc,AE}} = \frac{RT}{2F} \ln\left(\frac{p^{0.5}_{\text{O}_2,\text{bulk}}}{p^{0.5}_{\text{O}_2,\text{TPB}}}\right) \tag{7.13}$$

The species partial pressures at the TPB are determined using Equations 7.14-7.16. For these equations, current density j (A/m^2) is considered positive. In reality, the porous support layer has higher porosity than the active layer, leading to lower diffusion losses. To account for this, the model was modified by Hauck et al. [40], and the effective anode thickness δ_{FE} (m) was adjusted and a fitted value was used. The $p_{i,\text{bulk}}$, is the partial pressure of each species in the bulk. For H_2 and H_2O, it is calculated as the average partial pressure between the streams before and after the "ANODE" (see Figure 7.6) and for O_2 between the inlet and outlet streams of air in the SOFC. The CO partial pressure is added to the partial pressure of H_2.

$$p_{\text{H}_2,\text{TPB}} = p_{\text{H}_2,\text{bulk}} - \frac{RT\delta_{\text{FE}} \cdot j}{2F D_{\text{eff},\text{H}_2}} \tag{7.14}$$

$$p_{\text{H}_2\text{O,TPB}} = p_{\text{H}_2\text{O,bulk}} + \frac{RT\delta_{\text{FE}} \cdot j}{2F D_{\text{eff},\text{H}_2\text{O}}} \tag{7.15}$$

$$p_{\text{O}_2,\text{TPB}} = p_{\text{O}_2,\text{bulk}} - \frac{RT\delta_{\text{AE}} \cdot j}{4F D_{\text{eff},\text{O}_2}} \tag{7.16}$$

The effective diffusion coefficient $D_{\text{eff},i}$ (m^2 s^{-1}) for species i depends on the Knudsen diffusion coefficient $D_{\text{Kn},i}$ (m^2 s^{-1}) and the binary molecular diffusion coefficient D_{i-k} (m^2 s^{-1}) for species i and k. This relationship is outlined in Equation 7.17. The Knudsen diffusion coefficient is calculated using Equation 7.18. The binary diffusion coefficient is determined with the Fuller equation, which is Equation 7.19, where p is the stack pressure in (atm), τ and ε are the tortuosity of and the porosity of electrodes, d_p is the mean diameter of electrode pores in (m), M is the molecular mass in (g/mol) and V_d is the diffusion volume of each species.

$$D_{\text{eff},i} = \frac{\varepsilon}{\tau} \cdot \frac{D_{\text{Kn},i} D_{i-k}}{D_{\text{Kn},i} + D_{i-k}} \tag{7.17}$$

$$D_{\text{Kn},i} = \frac{d_p}{3}\sqrt{\frac{8RT}{\pi M_i}} \tag{7.18}$$

$$D_{i-k} = \frac{1.43 \times 10^{-7} \cdot T^{1.75}}{p\sqrt{\frac{2M_iM_k}{M_i+M_k}}\left(V_{d,i}^{1/3} + V_{d,k}^{1/3}\right)^2} \tag{7.19}$$

7.3.4. Stack output power

The SOFC stack-generated power is described in Equation 7.20:

$$P_{SOFC,generation} = V_{cell} \cdot I \tag{7.20}$$

7.3.5. Parameters

Table 7.2 presents the SOFC parameters used in the calculation of the overpotentials in the model reported by Amladi et al. [6], originally from Hauck et al. [40].

Table 7.2: SOFC parameters for overpotential calculations [6].

Parameter	Symbol	Value	Unit
Anode			
Thickness	δ_{FE}	$3.20 \cdot 10^{-5}$	m
Number of electrons transferred	n_{FE}	2	$\text{mol}_{\text{electron}}/\text{mol}_{\text{reactant}}$
Symmetry factor	α_{FE}	0.5	–
Pre-exponential factor	γ_{FE}	$1.34 \cdot 10^{10}$	$A \cdot m^{-2}$
Activation energy	$E_{\text{act,FE}}$	$1.00 \cdot 10^{5}$	$J \cdot mol^{-1}$
Cathode			
Thickness	δ_{AE}	$1.75 \cdot 10^{-5}$	m
Number of electrons transferred	n_{AE}	4	$\text{mol}_{\text{electron}}/\text{mol}_{\text{reactant}}$
Symmetry factor	α_{AE}	0.5	–
Pre-exponential factor	γ_{AE}	$2.05 \cdot 10^{9}$	$A \cdot m^{-2}$
Activation energy	$E_{\text{act,AE}}$	$1.20 \cdot 10^{5}$	J mol^{-1}
Electrolyte			
Thickness	δ_{el}	1.25×10^{-5}	m
Pre-exponential factor — conductivity	$\sigma_{0,\text{el}}$	$3.33 \cdot 10^{4}$	Ω^{-1} m^{-1}
Activation energy — conductivity	$E_{\text{act,el}}$	85,634	$J \cdot mol^{-1}$
Electronic area-specific Ohmic resistance	r_{const}	$5.70 \cdot 10^{-6}$	$\Omega \cdot m^2$
Diffusion Volume			
H_2	V_{d,H_2}	6.12	–
H_2O	V_{d,H_2O}	13.10	–
O_2	V_{d,O_2}	16.30	–
N_2	V_{d,N_2}	18.50	–
Molecular Mass			
H_2	M_{d,H_2}	2.02	$g \cdot mol^{-1}$
H_2O	M_{d,H_2O}	18.02	$g \cdot mol^{-1}$
O_2	M_{d,O_2}	32.00	$g \cdot mol^{-1}$
N_2	M_{d,N_2}	28.01	$g \cdot mol^{-1}$
Electrodes			
Porosity of electrodes	ε	0.30	–
Tortuosity of electrodes	τ	5.00	–
Mean diameter of electrode pores	d_p	$2.00 \cdot 10^{-6}$	m

7.3.6. Model Validation

The SOFC model adopted in this work and was validated against the reported experimental results and data of Amladi et al. [6]. The model was coded in MATLAB, where the modeled voltage and current density were calculated using input data from the reference study. The model was evaluated by varying the current density over a defined range, calculating the corresponding voltage using the Hauck et al. [40] model, and plotting the resulting voltage–current density characteristics. Table 7.3 presents the validation data used, while Figure 7.5 shows the correlation of the modeled and experimental points. The modeled results are a good fit to the experimental points of R^2 = 0.9465. The MATLAB code can be found in Section A.3 in Appendix A.

Table 7.3: Parameters for SOFC model validation [6].

Parameter	Value	Unit
Stack temperature	850	°C
Stack pressure	1	bar
Stack area	16	cm^2
Fuel inlet flow	0.01859	mol/min
Hydrogen mole fraction in fuel	0.5	-
Steam mole fraction in fuel	0.5	-
Oxygen mole fraction in oxidant	1	-

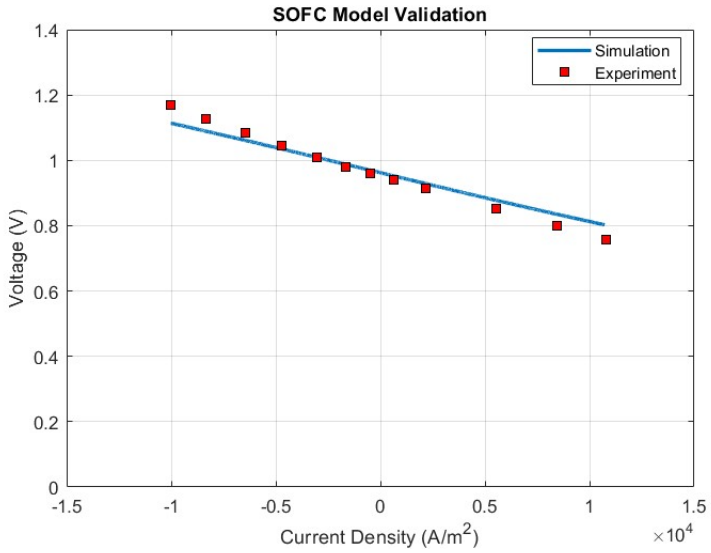

Figure 7.5: Validation of the simulated voltage–current density results against experimental data.

7.3.7. Aspen Plus Implementation

The SOFC is modeled in Aspen Plus using two heat exchanger blocks, three reactor blocks and a separator. Figure 7.6 presents the SOFC Aspen Plus model configuration.

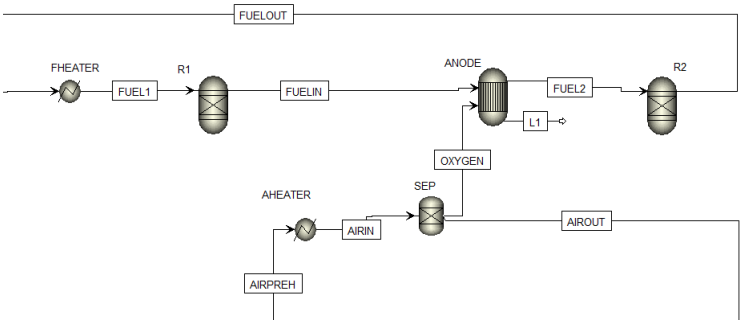

Figure 7.6: SOFC Aspen Plus Model.

Firstly, the MSR reformate gas is preheated in the heat exchanger ”HE2” of Figure 7.1 and then enters the SOFC. In the cell, it is further heated by the cell environment up to the operating temperature, which is modeled by the heat exchanger ”FHEATER”. Next, the gas enters the RGibbs reactor ”R1”, where it reaches chemical equilibrium. At this stage, as discussed in subsection 7.2.1, the reformate gas contains a considerable amount of CO, which the kinetic model did not account for in the ”REACTOR” block kinetics. Reactors ”R1” and ”R2” simulate the equilibrium conditions under which the SOFC operates. Following ”R1”, the fuel enters the ”ANODE” reactor block, where it reacts with oxygen.

In this system, air fulfills two critical functions: the SOFC thermal regulation and providing oxygen for fuel

oxidation in the anode. Ambient air is initially heated close to the designated inlet temperature (in heat exchanger ”B5” of Figure 7.1) and then directed to the cathode. Internally, the air is heated by the cell in the heat exchanger ”AHEATER” and reaches the cell’s operating temperature. Then the air is separated into the ”OXYGEN” and ”AIROUT” streams. The first, models the oxygen flow from the cathode through the electrolyte to the anode, basically the oxygen flow reacting with H_2 and CO in the anode. The ”AIROUT” stream models the cathode unreacted exhaust air comprising N_2 and O_2.

As both oxygen and MSR reformate gas enter the ”ANODE”, Reactions 4.3 and 7.21 occur. The CO produced after the ”R1” reactor is subsequently consumed within the ”ANODE” block, ensuring realistic species distributions throughout the system. The two overall reactions are simulated since Aspen Plus cannot simulate the individual half-cell reactions of the fuel cell [114]. The ”ANODE” block, modeled by a REquil reactor, operates at constant pressure and temperature. ”FUEL2” subsequently enters the RQibbs ”R2” where the stream exits the SOFC at chemical equilibrium.

$$\mathrm{CO} + \frac{1}{2}\,\mathrm{O_2} \leftrightarrow \mathrm{CO_2} \tag{7.21}$$

Two Calculator blocks were used to regulate the inlet fuel flow to the system and the oxygen flow to the anode. The inlet fuel molar flow of methanol is calculated using Equation 7.2 and by the molar composition of the inlet mixture of water and methanol, the total fuel molar flow is calculated. Additionally, the oxygen supply in stream ”OXYGEN” is defined in the Calculator as expressed in Equation 7.4. The SOFC fuel utilization factor, the SOFC operating temperature, the current density and the SOFC area are constant inputs to the calculator blocks. The current density varies for each power level. Its value is determined using a Design Specification in Aspen Plus, where the optimum value of the current density is found to match the system’s total power with the desired level.

Lastly, the SOFC model, described in the Section 7.3, is implemented as a Fortran subroutine in a different Calculator block. All the inputs regarding stream properties are imported into the calculator from the flowsheet and the model equations are written in the block. The block’s outputs are the voltage of the cell, the power generated and the overall power balance equation expressed in Equation 7.22. In the equation, $\dot{Q}_{Anode}$ symbolizes the total power (electrical and heat) produced by the ”ANODE” block, $P_{SOFC,generation}$ is the total power produced by the cell, $\dot{Q}_{Air,heater}$ and $\dot{Q}_{Fuel,heater}$ are the heat demands for heating the air and fuel to the stack temperature and $\dot{Q}_{R_1}$ and $\dot{Q}_{R_2}$ the heat required by the ”R1” and ”R2” reactor blocks. Since air plays a key role in the thermal management of the SOFC, its molar flow is controlled by a Design Spec in Aspen Plus such that the Balance equation equals zero. In other words, the air flow cools the SOFC stack, maintaining it at a constant temperature and ensuring electrical and heat balance.

$$Balance = \dot{Q}_{Anode} + P_{SOFC,generation} + \dot{Q}_{Air,heater} + \dot{Q}_{Fuel,heater} + \dot{Q}_{R_1} + \dot{Q}_{R_2} \tag{7.22}$$

7.4. Organic Rankine Cycle

As shown in Figure 7.7, the ORC system is a single-stage configuration with key components such as a pump, evaporator, expander and condenser. A pump pressurizes the working fluid, which is then evaporated using the hot stream ”HS5”, expanded in a turbine to generate power, and condensed before returning to the pump. The cycle recovers low-grade heat (via ”HS5”) to produce additional electrical power efficiently. A pinch point of 13°C in the evaporator is maintained in all power levels between the heating stream ”HS5” and ”ORC3”. The ”W1” stream represents the water stream cooling the condenser, entering at ambient conditions.

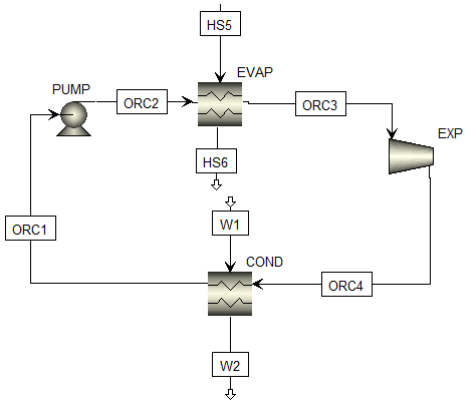

Figure 7.7: ORC Aspen Plus Model.

7.5. Heat Utilization Network

The heat utilization network of heat exchangers is designed taking into consideration the following key parameters:

1. The exhaust gas should exit in a vapor phase.
2. Air should be heated as close to 100 °C lower than the SOFC operating temperature, by the heat exchangers network.
3. The inlet fuel to the MSR reactor should be preheated to a sufficiently high temperature to ensure that the process stream reaches the desired temperature range within the reactor.
4. The heat stream in the MSR reactor should be sufficiently hot such that the reaction occurs and is completed along the entire reactor length. No unreacted methanol exits the reactor.
5. The need for additional electrical heaters should be avoided.
6. The afterburner's temperature should be at least 800 °C, to ensure combustion.
7. A minimum 13 °C temperature pinch point should be maintained in all heat exchangers between the hot and cold streams.
8. Splitting of hot streams should be avoided.

As shown in Figure 6.2, the integrated heat recovery network maximizes energy efficiency by utilizing waste heat from the SOFC and the afterburner. Initially, the anode gas, after it exits the SOFC, preheats the reformate gas before it enters the SOFC. Meanwhile, the cathode off-gas is directed to the afterburner, where it undergoes combustion with the anode gas. The resulting high-temperature exhaust serves as a thermal source for the system. It firstly preheats the air stream at a higher temperature range and then acts as the thermal fluid of the MSR reactor. Subsequently, it preheats the inlet MSR fuel and is recirculated further to preheat the air stream at a lower temperature range. Finally, the stream is utilized as the heat source for the ORC evaporator before being discharged as exhaust.

The multiple heat exchangers design enables efficient preheating and reduction of external heating needs. In the network, all heat exchangers are considered counter-current. This innovative thermal integration covers all key parameters and enhances overall system performance by minimizing energy losses and utilizing available heat across all sub-systems.

7.6. Afterburner

The afterburner's main role is to convert the chemical energy in the exhaust gases into heat through combustion and is generally placed directly after the SOFC stack [114]. The afterburner was modeled as an RGibbs reactor operating at constant pressure and adiabatic conditions (zero heat duty), presented in Figure 7.8. Since the combustion reaction is exothermic, the temperature in the reactor rises.

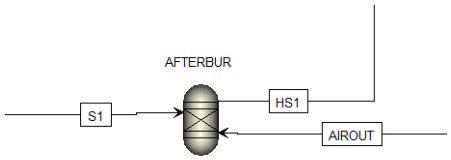

Figure 7.8: Afterburner Aspen Plus Model.

7.7. Efficiencies

7.7.1. SOFC Efficiency

The SOFC efficiency is defined in Equation 7.23, as the ratio of the generated power by the SOFC to the inlet chemical energy input to the anode, derived from the hydrogen feed.

$$\eta_{\text{SOFC}} = \frac{P_{\text{SOFC, generation}}}{(\dot{n}_{\text{H}_2} \cdot \text{LHV}_{\text{H}_2})_{\text{anode,in}}} \tag{7.23}$$

7.7.2. ORC Efficiency

The ORC efficiency is defined in Equation 7.24, as the ratio of the net generated power by the ORC to the inlet thermal energy input from the heat source in the evaporator. The net generated power is determined by subtracting the power consumed by the pump from the power produced by the turbine.

$$\eta_{\text{ORC}} = \frac{P_{\text{ORC,net}}}{\dot{Q}_{evap}} \tag{7.24}$$

7.7.3. System's Electrical Generation Efficiency

The system's electrical generation efficiency is defined in Equation 7.25, as the ratio of generated AC power by the SOFC and the ORC to the inlet chemical energy input to the system, derived from the methanol feed. The AC-generated power of the SOFC is calculated as the power generated by the fuel cell $P_{SOFC,generation}$ multiplied by the inverter's efficiency, which converts the DC produced power of the SOFC to AC. Respectively, the AC-generated power by the ORC is calculated as the net power generated by the cycle $P_{ORC,net}$ multiplied by the generator's and inverter's efficiencies, which convert the DC produced power in the turbine of the ORC to AC.

$$\eta_{\text{el,sys}} = \frac{P_{\text{AC,SOFC}} + P_{\text{AC,ORC}}}{(\dot{m}_{\text{CH}_3\text{OH}} \cdot \text{LHV}_{\text{CH}_3\text{OH}})_{\text{system,in}}} \tag{7.25}$$

7.7.4. System's CHP Efficiency

The system's CHP efficiency is defined in Equation 7.26, as the ratio of the total AC generated power of the system plus the heat released by heating the water in the condenser of the ORC. This heated stream can be repurposed for other onboard applications, such as space heating or domestic hot water supply within the yacht.

$$\eta_{\text{CHP}} = \frac{P_{\text{AC,SOFC}} + P_{\text{AC,ORC}} + \dot{Q}_{\text{cond}}}{(\dot{m}_{\text{CH}_3\text{OH}} \cdot \text{LHV}_{\text{CH}_3\text{OH}})_{\text{system,in}}} \tag{7.26}$$

7.7.5. Parameters

Table 7.4 lists the hey thermochemical properties of methanol and hydrogen and the efficiencies used for the generator and inverters in the model. The inverter efficiency from DC to AC is set at 95% [87] and the ORC generator efficiency is set at 90% [102], with the values held constant across all system power levels.

Table 7.4: Thermochemical Properties and Efficiencies used in the model.

Parameter	Value	Unit	Source
Methanol Lower Heating Value	638.1	kJ/mol	[72]
Hydrogen Lower Heating Value	120.0	MJ/mol	[25]
Inverter efficiency	95	%	[87]
Generator efficiency	90	%	[102]

7.8. Conclusion

This chapter presented the modeling framework used to assess the feasibility and performance of the proposed MSR–SOFC–ORC system. A steady-state Aspen Plus model was developed, incorporating literature-based kinetics, electrochemical loss models, and validated subroutines for key system components. Each subsystem—MSR, SOFC, ORC, and the afterburner—is modeled with realistic assumptions based on experimental or literature data, ensuring technical accuracy. The system design incorporates detailed heat integration to enhance overall efficiency and minimize the need for external heaters. The defined efficiencies will guide performance evaluation across different power states, laying the foundation for the analysis presented in the following chapters.

8

System Sizing

In this chapter, the complete sizing methodology for each subsystem of the integrated power system is presented. The focus lies on the ORC, the SOFC, the MSR reactor and the heat utilization network. Accurate dimensioning of these components is crucial to ensure optimal performance, energy efficiency, and thermal integration under the specified operational conditions. The analysis builds on literature-based parameters and design constraints, with the system inlet streams entering at ambient inlet conditions of 25 °C and 1 bar [61]. Each subsystem is tailored to meet the power and heat demands of the superyacht, with the overall goal of achieving a reliable, self-sustained, and thermally efficient energy system.

8.1. Organic Rankine Cycle

8.1.1. Working Fluid Selection

The working fluid R1233zd(E) is selected for this project due to its comparably beneficial properties. Among the other ORC working fluids (see Table B.1 in Appendix B), R1233zd(E) presents the lowest GWP and ODP values combined, making it the most favorable choice for a sustainable ORC system. Moreover, its high molecular mass results in a lower volumetric flow rate, consequently reducing the size and cost of equipment (turbines, pumps, and heat exchangers). The corresponding lower specific volume allows the turbine to operate at reduced blade speeds and mechanical stress, enhancing reliability and simplifying design. Additionally, its high critical temperature allows reaching higher temperatures and pressures in the evaporator, thus increasing the pressure ratio (ratio of high to low pressure level of the cycle) and allowing more power to be extracted in the expander. The fluid's properties are presented in Table 8.1, where the safety group A1 by ASHRAE Standard 34 indicates that R1233zd(E) is safe to handle under normal conditions, with minimal health and fire risks, making it suitable for commercial ORC systems.

Table 8.1: Properties of the R-1233zd(E) ORC working fluid [80].

Working fluid	T_{cr} (°C)	P_{cr} (MPa)	ODP	GWP	Safety group
R1233zd(E)	166.5	3.62	0.00034	1	A1

8.1.2. Model Inputs and Operating Conditions

In this work, the condenser temperature is set to 32.8 °C, consistent with standard practice, as condenser temperatures are typically maintained at 30 °C or higher [41]. Moreover, the condenser pressures are often maintained above atmospheric pressure to prevent air from leaking into the system. Operation near the critical point is avoided due to the rapid variation of thermophysical properties, which can lead to system instability and reduced heat transfer performance. To ensure reliable heat exchanger operation, the maximum cycle temperature and pressure are set at least 10 °C below the critical conditions of the working fluid. The pump and expander isentropic efficiencies are set to 0.85, based on Li et al. [61]. The working fluid mass flow is selected such that, at a 225 kW power level, the "HS6" stream exits the system in vapor phase. The water-cooled condenser is designed to subcool the working fluid by 5 K below its saturation temperature, and subcooling/superheating values are based on the design by Georges et al. [35]. The hot stream "HS5" is maintained at a constant 150 °C across all power levels to ensure consistent evaporator heating. Overall, Table 8.2 summarizes the operating conditions and input parameters of the ORC model.

Table 8.2: Input parameters and operating conditions of the ORC used in the model.

Parameter	Value
Working fluid	R1233zd(E)
Temperature of the hot stream in the evaporator	150 °C
Evaporation Pressure	20 bar
Evaporation Temperature	137.2 °C
Evaporation Superheating	5 K
Condensation Pressure	2 bar
Condensation Temperature	32.8 °C
Condensation Subcooling	5 K
Pump isentropic efficiency	0.85
Expander isentropic efficiency	0.85
Mass flow of R1233zd(E)	0.381 kg/s
Mass flow of water in the condenser	0.515 kg/s

8.2. Solid Oxide Fuel Cell

As mentioned in subsection 6.2.2, the SOFC is sized such that it provides the necessary power to the fuel pump, the air compressor, and the SWRO unit, as well as contributes, along with the ORC, to the auxiliary power demand of the superyacht. Figure 8.1 presents the current density–voltage–power density profiles of SOFC assembled single cells by Buonomano et al. [18], which were generated by evaluating their electrochemical performance. The maximum power density of cells without graphite is 4900.174 W/m^2, which was used for the SOFC sizing. For the maximum system power demand of 325 kW, the freshwater requirement is the sum of the ORC condenser and the MSR process water demands. Given the SWRO unit's consumption of approximately 3 kWh/m^3 [55], its power demand was calculated and combined with the air compressor's.

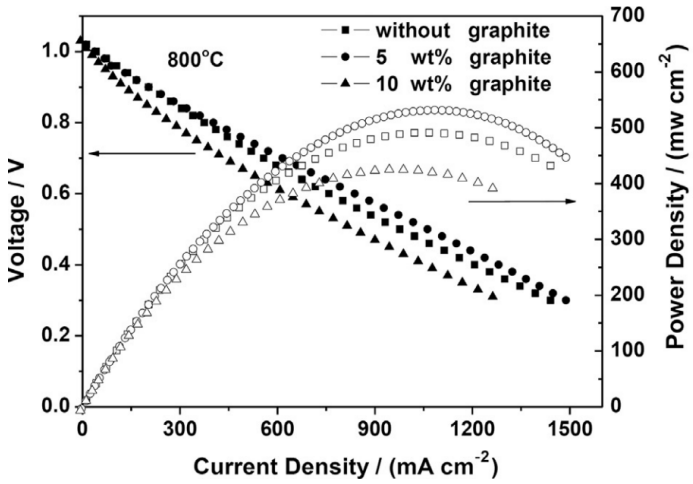

Figure 8.1: Current density–Voltage–Power density profiles of three individual SOFC cells tested at 800°C [18].

The ORC contributes approximately 14.1 kW, leaving 310.9 kW to be supplied by the SOFC. The fuel pump's power demand is negligible (at 0.0012 kW at the maximum power level). After accounting for the SWRO and compressor demands, the total maximum required SOFC output is calculated to be around 355.64 kW. Dividing this by the maximum power density yielded a required SOFC active area of 72.7 m^2. More details on the SOFC sizing process can be found in Appendix C Section C.1.

Table 8.3 presents the SOFC operating characteristics and the physical parameters used in the model. The stack area and the current density were chosen as input constants, whereas the fuel utilization and temperature were adopted from the Amladi et al. [6] study. In their sensitivity analysis, the fuel utilization was held steady at 80% and current density, stack temperature and pressure were varied. Additionally, the fuel cell operation at 800 $^{\circ}\mathrm{C}$ was found to be the optimum with the minimum exergy efficiency.

Table 8.3: Physical parameters and operating characteristics of the SOFC used in the model [6].

Parameter	Value	Unit
Fuel Utilisation	0.8	–
Temperature of the SOFC stack	800	$^{\circ}\mathrm{C}$
Pressure of the SOFC stack	1.098	bar
Stack area	72.7	m^2

8.3. Methanol Steam Reforming Reactor

The MSR reactor was sized based on two key design principles. The first factor is keeping the tube-to-particle diameter ratio greater than 10. At this ratio, wall effects and flow or heat maldistribution are minimal [107]. This leads to better catalyst use and manageable pressure drops. As a result, the Ergun equation, which is based on a uniform, infinitely extended bed, can accurately predict pressure drop with less than 3% deviation from more complex models. This significantly simplifies reactor design and operation by removing the need to consider edge effects. Hence, the catalyst particle and tube diameters used by Zhu et al. [116] were adopted for reactor sizing in this work, as their dimensions ensure a diameter ratio greater than 10.

The second design consideration was to ensure that the temperature range of the process stream matched the operating range of the applied kinetic model. To achieve this, the length and number of reactor tubes were varied through a series of trials. These parameters were adjusted until the minimum temperature of the process stream in the reactor closely approached the target value of 180 °C, ensuring consistency with the kinetic assumptions. Table 8.4, displays the input parameters, reactor dimensions and conditions of the MSR reactor block. Regarding the heat transfer coefficient, its value varies a lot in literature, with values ranging from 50-200 W/m^2K [66, 31, 94]. A value of 100 W/m^2K was chosen as the heat transfer coefficient in this work [91]. The reaction kinetics of reaction (3.6) are inserted in the ”Reactions” section of the Aspen Plus flowsheet.

Table 8.4: Parameters and operating conditions of the MSR reactor used in the model.

Parameter	Value	Unit	Source
S/C molar ratio	1.3	-	[56]
Catalyst particle diameter	1.5	mm	[116]
Void fraction	0.38	-	[116]
Process stream temperature range	173.3 - 239.5	°C	[61]
Operating Pressure	1.098	bar	[116]
Heat transfer coefficient	100	W/m^2K	[91]
Tubes’ diameter	1.6	cm	[116]
Pressure drop	0.098	bar	[30]
Reactor length	1.3	m	-
Number of tubes	95	-	-

8.4. Heat Utilisation Network

The heat utilization network was developed through an iterative process, exploring various configurations to meet key design objectives. The final layout was guided by a clear prioritization of subsystem thermal needs, aiming to fully preheat the inlet air and fuel, avoid splitting hot streams, and ensure the exhaust gas exited in the vapor phase. High-temperature exhaust from the SOFC was first used to preheat the fuel—specifically the anode stream due to its lower mass flow—before merging with the cathode stream in the afterburner to recover temperature losses. The resulting hot gas was then directed to preheat the air at its highest required temperature range, while also ensuring a suitable outlet temperature for MSR heating. After heating the MSR, the residual heat was sequenced to preheat the methanol-water feed, and finally to raise the air inlet temperature before compression. The network was thus structured by matching heat sources to the most thermally demanding subsystems, with special attention given to the requirements of the MSR process and ORC, ensuring efficient and targeted thermal integration. Key temperatures in the heat utilization network were set and kept constant across all power levels, as shown in Figure 8.2. More specifically, the temperature of the anode and cathode gases is defined within the SOFC blocks, while the fuel exits the second heater at

700 °C. The temperature of the thermal fluid-exhaust gas at the external heating of the MSR reactor is set at 285 °C and at the ORC evaporator is set at 150 °C. Lastly, the air and fuel both enter the system at 25 °C. Further analysis on the heat utilization network design process can be found in Appendix C section C.2.

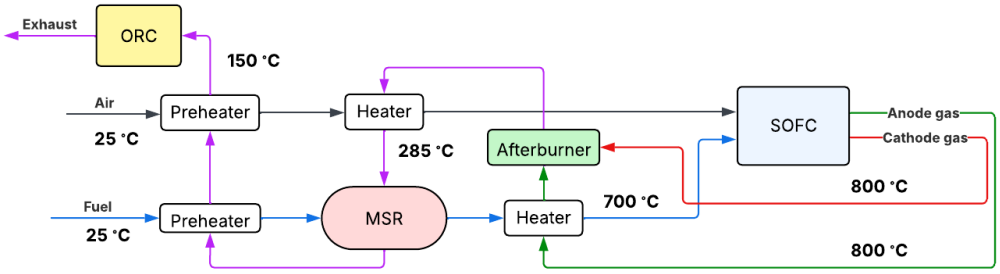

Figure 8.2: Key temperatures set in the heat utilization network.

8.5. Conclusion

The system sizing described in this chapter provides a basis for the following simulation and performance evaluation of the integrated energy system. The SOFC is sized to produce most of the auxiliary electrical power, with support from the ORC, which recovers waste heat. The MSR reactor is designed to meet temperature limits and ensure stable reforming conditions. Meanwhile, the heat utilization network effectively redistributes thermal energy to improve efficiency across all subsystems. By matching component parameters with realistic operating limits and insights from literature, this sizing method helps create a consistent and balanced design for the intended maritime application.

9 Results

This chapter presents the simulation results of the integrated bio-methanol-fueled energy system, examining the behavior and performance of its core components across three auxiliary system power levels: 325 kW, 275 kW, and 225 kW. The results begin with an analysis of the MSR process, focusing on species evolution and thermal profiles in Section 9.1. Next, in Sections 9.2 and 9.3, the performance of the ORC and the heat utilization network is evaluated to assess heat recovery and thermal integration. The combustion fuel composition in the afterburner is also investigated in Section 9.4. Following this, Section 9.5 provides detailed insights into the SOFC results, including fuel composition, power output, and operational efficiency. Finally, in Sections 9.6 to 9.8 the chapter presents an overview of resource consumption, overall system performance, and a sensitivity analysis examining the effects of the SOFC fuel utilization and temperature on system behavior.

9.1. Methanol Steam Reforming

This section presents the results of the MSR process for the three different system power levels. The results include the composition graphs of molar fractions of the species in the MSR reaction and the temperature profiles of the thermal fluid and process stream in the MSR reactor.

9.1.1. Molar composition

Figure 9.1 illustrates the molar composition profiles of H_2, H_2O, CO_2, and CH_3OH along the MSR reactor length for the three different system power levels studied: 325 kW, 275 kW, and 225 kW. These profiles explain how the MSR process progresses under varying system power conditions. In the different power states, the molar flow of the inlet fuel (methanol and water) changes, increasing as the power level increases.

Regarding the products, in all three cases, the mole fraction of hydrogen increases steadily with reactor length, indicating that the reforming reaction is proceeding efficiently. The final H_2 molar fraction is approximately the same in all power levels, equal to 0.6977. The CO_2 concentration rises progressively along the reactor and eventually levels off at 0.2326, indicating the point at which the reaction approaches equilibrium. On the other hand, the concentrations of the main reactants, methanol and water, decrease along the reactor length. Methanol is consumed rapidly in the early sections of the reactor due to its high reactivity. The water molar fraction also declines throughout the reactor, following a similar trend, due to its role in both the reforming reaction and as a heat sink. The final molar composition of the reformate gas is presented in Table 9.1.

Table 9.1: Molar composition of the reformate gas, product of the MSR process.

H_2	H_2O	CO_2	CH_3OH
0.6977	0.0697	0.2326	0

The differences in molar composition profiles between the three figures originate primarily from changes in flow rate. At higher system power levels, with a higher inlet fuel molar flow rate, the process stream passes through the reactor more quickly, resulting in a shorter residence time and reduced contact with the catalyst. The Aspen Plus simulations indicate that the residence time is 0.088 sec at 325 kW, 0.104 sec at 275 kW,

and 0.127 sec at 225 kW, as is presented in Table 9.2.

Table 9.2: Residence time for both the process stream and the thermal fluid in the MSR reactor for three different system power levels.

P_{system} (kW)	Residence time (sec)
325	0.088
275	0.104
225	0.127

Despite the higher flow of thermal fluid at higher power levels, the larger heat capacity of the process stream limits the temperature rise. This leads to slower reaction rates and a more gradual conversion of methanol and water along the reactor. In contrast, at lower system power levels and lower inlet molar flow rates, longer residence times are observed, and more effective heating enables the process stream to reach higher temperatures earlier in the reactor. This accelerates the reaction kinetics, resulting in a faster conversion of reactants and an earlier formation of products. Consequently, the reactants are consumed more quickly in the low-flow case, while in the high-flow case, conversion extends over a longer reactor length and thus, the plateau of the products is reached sooner in the 225 kW case compared to the higher power levels. Overall, these findings underscore the importance of effective thermal management and accurate system sizing when designing reformers for downstream energy conversion units, such as SOFCs.

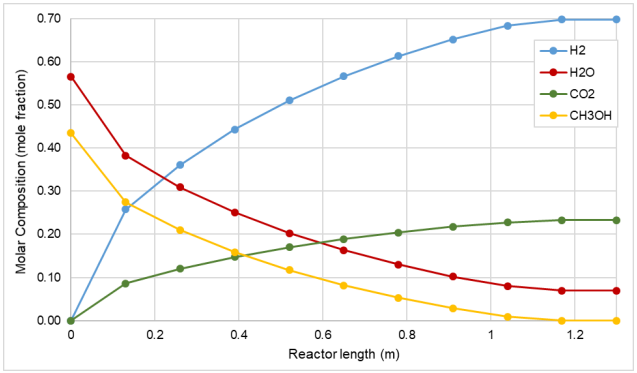

(a) System power level equal to 325 kW.

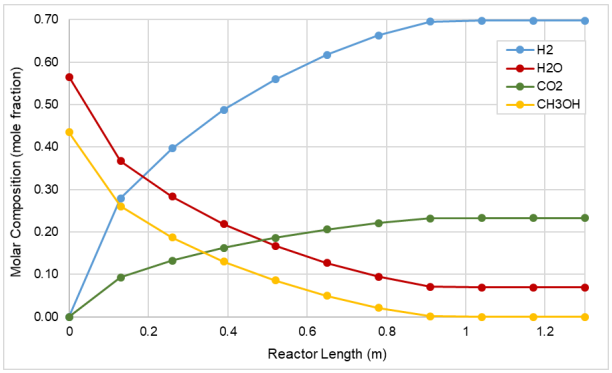

(b) System power level equal to 275 kW.

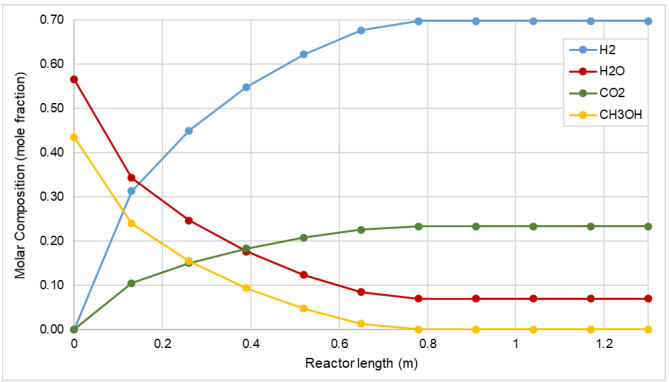

(c) System power level equal to 225 kW.

Figure 9.1: Molar composition profiles along the MSR reactor length for three different system power levels.

9.1.2. Temperature profiles

Figure 9.2 presents the temperature profiles of the process stream (reactants and products) and the external thermal fluid along the reactor length for three different power levels of the system: 225 kW, 275 kW, and 325 kW. The thermal fluid, which provides the heat necessary to drive the endothermic MSR reaction, enters the system at the high temperature of 285 °C in all cases and gradually releases heat transferred to the process stream, decreasing its temperature. Higher power levels result in slightly elevated thermal fluid temperatures along the reactor's length, reflecting the reduced heat transfer to the process stream. As discussed in

subsection 9.1.1, at higher system power and inlet fuel flow rate, although the thermal fluid flow rate is also increased, the quick flow through the reactor and the high heat capacity of the process stream limit the heat transfer between the two sides of the reactor.

The process stream exhibits a steep temperature drop immediately after entering the reactor due to the intense heat absorption associated with the endothermic nature of the reforming reaction. After this drop, the process stream temperature gradually increases along the reactor length as it continues to absorb heat from the thermal fluid. This recovery is more significant at lower power levels, with the 225 kW case reaching the highest outlet temperature, followed by the 275 kW and 325 kW cases.

Overall, the graph illustrates how increasing system power impacts thermal behavior in the MSR reactor: lower power levels enhance the heat transfer rate due to longer residence times, leading to improved temperature recovery within the process stream.

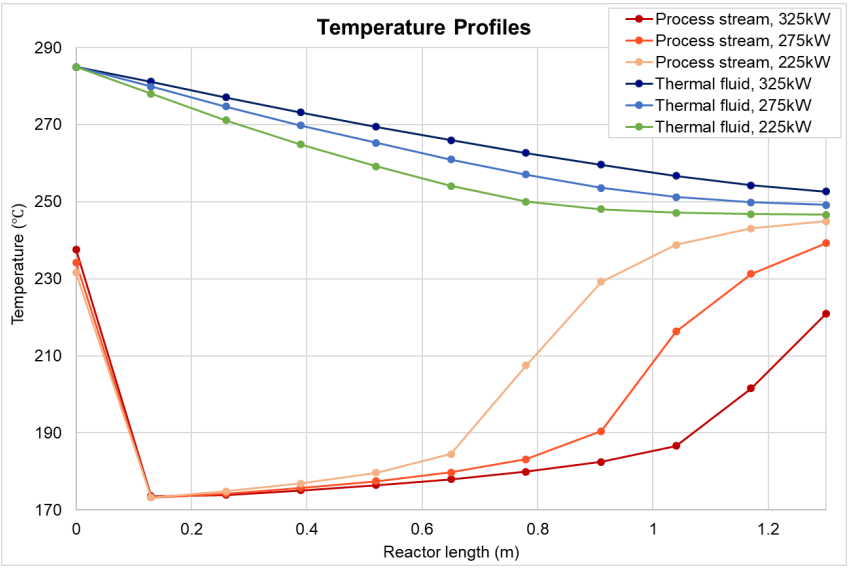

Figure 9.2: Temperature profiles of the thermal fluid and process stream of the MSR reactor for three system power levels.

9.2. Organic Rankine Cycle

The key performance parameters of the ORC subsystem are shown in Table 8.2. The pump power demand is 0.65 kW, while the expander produces a gross power output of 14.75 kW. After considering the pump's consumption, the net electrical power output of the cycle is 14.1 kW. The thermal energy provided to the evaporator is 96.4 kW. Based on these numbers, the overall thermal efficiency of the ORC system is 14.6%, representing the net power output compared to the thermal energy input. This efficiency aligns with the typical performance levels of ORC systems that utilize low- to medium-temperature heat sources.

Table 9.3: ORC Results.

Parameter	Value
Pump power demand (kW)	0.65
Expander power production (kW)	14.75
ORC Net Power Production (kW)	14.10
Heat input to the evaporator (kW)	96.40
ORC Efficiency	14.6%

9.3. Heat Utilization Network

Table 9.4 presents the resulting temperatures of the inlet air in the SOFC, the exhaust gas and afterburner for the three system power levels. As aimed, the inlet air enters the SOFC with temperatures very close to 700 °C and the exhaust gas exits with temperatures lower than 90 °C. Lastly, the afterburner operates at all levels above 800 °C, which satisfies one of the key requirements of the network design.

Table 9.4: SOFC inlet air, exhaust gas, and afterburner temperatures at varying system power levels.

P_{system} (kW)	$T_{air,in\ SOFC}$ (°C)	$T_{exhaust}$ (°C)	$T_{afterburner}$ (°C)
325	692.4	88.3	842.0
275	691.8	69.8	845.5
225	691.3	41.2	848.3

9.4. Afterburner

Table 9.5 presents the molar compositions of the ”S1”, ”AIROUT” and ”HS1” streams for the 225 kW power level. In this afterburner process, the fuel-rich stream (”S1”) containing mainly H_2, CO_2 and CO is mixed with an oxidizer stream (”AIROUT”) rich in O_2 and N_2. Complete combustion occurs, converting H_2 to H_2O and CO to CO_2, with negligible unburned fuel in the outlet stream (”HS1”). As can be seen, H_2, H_2O, CO_2 and CO react completely and they are found in minimal quantities in the product stream. The combustion is very lean, as indicated by the high excess air ratio (λ≈30), with significant O_2 remaining in the exhaust. Methane and methanol are present in the ”HS1” stream (same stream composition as the exhaust gas stream ”HS6”), in negligible amounts and have minimal impact.

Table 9.5: Mole fractions composition of reacting and product streams in the afterburner at 225 kW system power.

Species	S1	AIROUT	HS1
H_2	0.1091	-	3.28e-10
H_2O	0.6584	-	0.0648
CO_2	0.2020	-	0.0196
O_2	1.49e-17	0.19	0.1690
CH_3OH	5.52e-12	-	4.43e-36
CO	0.0306	-	1.09e-10
N_2	-	0.81	0.7466
CH_4	4.27e-07	-	3.20e-36
C	1.24e-30	-	5.20e-37

9.5. Solid Oxide Fuel Cell

9.5.1. Fuel Composition

Table 9.6 presents the molar fraction composition of the fuel and air streams in the SOFC. Along with many reactions occurring in reactor ”R1”, evidently the r-GWS dominates, increasing significantly the amount of CO and H_2O in the fuel and decreasing the amounts of CO_2 and H_2. In the ”ANODE”, H_2 and CO react with O_2 and thus the amounts of H_2O and CO_2 increase. Finally, in the ”R2”, all the reactions occurring result in the chemical equilibrium state of the ”FUELOUT” stream. Due to the negligible molar carbon fraction, the carbon deposition risk in the SOFC is eliminated.

Table 9.6: Mole fractions of fuel and air streams in the SOFC.

Species	FUEL1	FUELIN	FUEL2	FUELOUT	AIRIN	AIROUT
H_2	0.6977	0.5376	0.1069	0.1091	-	-
H_2O	0.0697	0.2295	0.6602	0.6584	-	-
CO_2	0.2326	0.0740	0.2023	0.2020	-	-
O_2	-	7.48e-20	1.56e-17	1.49e-17	0.21	0.19
N_2	-	-	-	-	0.79	0.81
CH_3OH	-	6.94e-10	6.94e-10	5.52e-12	-	-
CO	-	0.1582	0.0299	0.0306	-	-
CH_4	-	0.0008	0.0008	4.27e-07	-	-
C	-	9.03e-29	9.03e-29	1.24e-30	-	-

9.5.2. Power Distribution

The SOFC increases its power output at higher levels, covering the demand in addition to the ORC power production, which remains constant. Table 9.7 provides a breakdown of the power generated by the SOFC and its distribution across key auxiliary components in the system for three different power levels: 325 kW, 275 kW, and 225 kW. The total SOFC-generated power ($P_{\text{SOFC,generation}}$) ranges from 355.64 kW at the highest system load to 233.67 kW at the lowest. The heat released by the SOFC ($P_{SOFC,heat}$) ranges from 213.94 kW at the highest to 124.02 kW at the lowest power level. Moreover, the net available SOFC power ($P_{\text{SOFC,net}}$) to cover the auxiliary power demand—after accounting for the SWRO unit, the fuel pump and the air compressor—also decreases accordingly. The two primary auxiliary loads are the air compressor (P_{Compr}) and the SWRO unit (P_{SWRO}). As expected, the power demand for both components scales with system size, with the compressor consuming between 8.30 kW and 15.37 kW, and the SWRO unit requiring between 14.50 kW and 29.40 kW. This table highlights the importance of accounting for auxiliary demands when sizing the system and evaluating net power availability and overall system efficiency.

Table 9.7: SOFC Power distribution.

P_{system} (kW)	$P_{SOFC,generation}$ (kW)	$P_{SOFC,heat}$ (kW)	$P_{SOFC,net}$ (kW)	P_{Compr} (kW)	P_{SWRO} (kW)
325	355.64	213.94	310.91	15.37	29.40
275	294.53	166.38	260.91	11.52	22.10
225	233.67	124.02	210.92	8.30	14.50

9.5.3. Operation and Efficiency

Figure 9.3 illustrates the relationship between SOFC voltage and current density, showing a typical declining trend as current density increases. At low current densities, the voltage remains close to the open-circuit voltage (approximately 0.94 V). At higher current densities, a typical trend for the SOFCs is seen where the voltage gradually decreases due to increasing activation, ohmic, and concentration losses. The relatively linear drop of the voltage suggests moderate ohmic losses and a marginal influence of activation and concentration losses. The figure also reveals a well-managed fuel utilization (no fuel depletion) within the modeled operating range. As can be seen, the trend aligns with the voltage-current density graph of Buonomano et al. [18], which was used to size the stack (Figure 8.1).

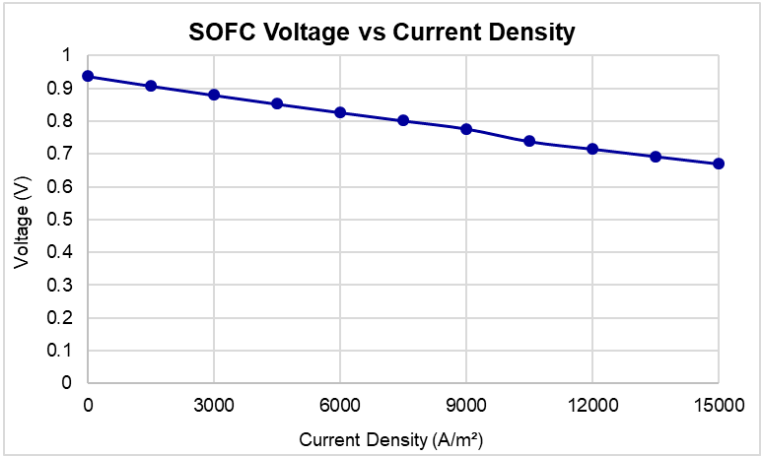

Figure 9.3: Current density-Voltage profile of the SOFC stack operating at 1.098 bar and 800 °C.

Table 9.8 presents the SOFC operating parameters and efficiency at the three system power levels: 325 kW, 275 kW, and 225 kW. As the system power decreases, the SOFC-generated power ($P_{SOFC,generation}$) decreases proportionally. The current density follows a similar trend, declining from 5902.7 A/m^2 at 325 kW to 3706.8 A/m^2 at 225 kW, indicating reduced electrochemical activity at lower power levels. In contrast, the cell voltage increases slightly as power decreases, from 0.829 V at 325 kW to 0.867 V at 225 kW. This reflects lower ohmic and concentration losses under reduced current densities. Consequently, the SOFC electrical efficiency (η_{SOFC}) improves with decreasing system power, rising from 52.9% at 325 kW to 55.3% at 225 kW, highlighting the trade-off between output and efficiency, where lower operating loads favor more efficient cell performance. In other words, at lower power levels and current densities, the SOFC operates within a more

favorable electrochemical regime, characterized by higher cell voltage and greater electrical energy extracted per mole of fuel. Under these conditions, thermal and mass transport limitations are less severe, resulting in reduced degradation, enhanced operational stability, and an extended system lifetime.

Table 9.8: SOFC Operating Parameters and Efficiency.

P_{system} (kW)	$P_{SOFC,generation}$ (kW)	Current density (A/m^2)	Voltage (V)	η_{SOFC}
325	355.6	5902.7	0.829	52.9%
275	294.5	4776.7	0.848	54.1%
225	233.7	3706.8	0.867	55.3%

9.6. Consumption of Resources

Table 9.9 presents the annual resource consumption associated with three different system power levels (325 kW, 275 kW, and 225 kW) under a constant fuel utilization factor of $U_f = 0.8$. As expected, the consumption of methanol, air, and water decreases with lower system power. At the highest power level of 325 kW, the system requires 936.9 tonnes of methanol per year, 83,945.4 m^3 of air, and 16,969.6 m^3 of water. These values drop progressively at lower power levels: for 275 kW, the methanol, air, and water demands are 758.2 t/y, 64,383.9 m^3/y, and 16,838.7 m^3/y, respectively; and for 225 kW, they are 588.4 t/y, 47,338.9 m^3/y, and 16,714.4 m^3/y. The vast majority of the system's water demand—over 96%—is attributed to the ORC cycle, with the remaining fraction corresponding to the water required for the MSR process. Overall, the table highlights the scaling behavior of input requirements with respect to system power output.

Table 9.9: Methanol, Air and Water annual consumptions at the three different system power levels and under a constant fuel utilization factor of $U_f = 0.8$.

P_{system} (kW)	Methanol (t/y)	Air (m^3/y)	Water (m^3/y)
325	936.9	83,945.4	16,969.6
275	758.2	64,383.9	16,838.7
225	588.4	47,338.9	16,714.4

9.7. System Performance

Table 9.10 presents the system's efficiencies at three different power levels: 325 kW, 275 kW, and 225 kW. It highlights two main performance metrics: electrical generation efficiency of the overall system ($\eta_{el,sys}$) and combined heat and power efficiency (η_{CHP}). As the system power decreases, both efficiencies increase. The electrical generation efficiency improves from 52.0% at 325 kW to 57.2% at 225 kW, while the CHP efficiency rises significantly from 65.9% to 79.4%. These trends indicate that the system operates more efficiently at lower power levels, likely due to more favorable electrochemical and thermal conditions.

Table 9.10: System Performance Efficiencies.

P_{system} (kW)	$\eta_{el,sys}$	η_{CHP}
325	52.0%	65.9%
275	54.3%	71.5%
225	57.2%	79.4%

Comparing these results with the relevant study by Li et al. [61], it becomes evident that the system presented in this work performs at a comparable level. In their analysis of an MSR–SOFC–ORC–Engine system, they report a power generation efficiency of 61.86%. However, their calculation does not account for conversion losses in the generator and inverter, which are included in the present work's overall system efficiency. Taking this into consideration, the electrical generation efficiency achieved in this study—ranging from 52.0% to 57.2%—is very close, especially under lower power loads. This comparison confirms that the proposed system is equally efficient and well-optimized from an electrochemical and thermal integration perspective.

Figure 9.4 depicts the SOFC, the system's electrical generation and CHP efficiencies as a function of the total system power level. It is clear that, at higher power levels, the efficiencies drop.

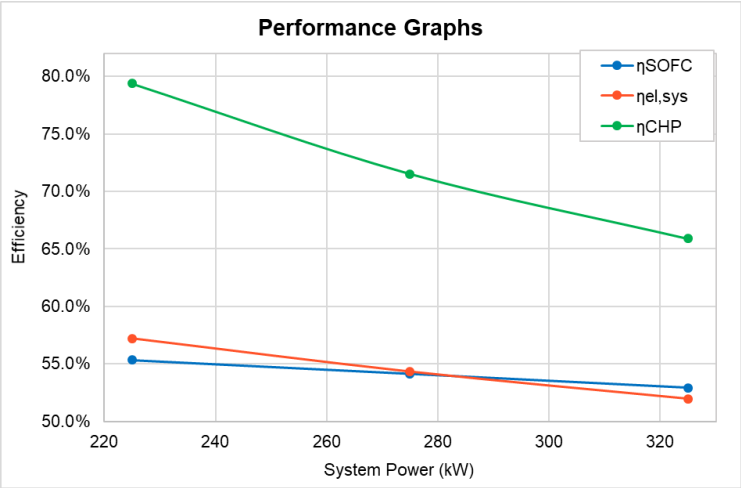

Figure 9.4: SOFC, System electrical and CHP efficiencies as a function of the total system power.

9.8. Sensitivity Analysis

To evaluate the system's performance and assess its suitability under different operating conditions, a sensitivity analysis was performed through two separate cases. Such an analysis is a valuable tool for identifying how changes in key parameters affect the overall system behavior, pinpointing optimal operating ranges and guiding design decisions. In the first case, the SOFC fuel utilization factor (U_f) was varied while maintaining a constant SOFC operating temperature (T_{SOFC}) of 800 °C. This allowed for an assessment of how efficiently the fuel is being used and its impact on system outputs. In the second case, T_{SOFC} was varied while keeping U_f fixed at 0.8, providing insight into how temperature influences electrochemical performance, thermal integration, and overall system efficiency. Together, these cases provide valuable insights into the underlying trade-offs and support the development of a well-optimized and resilient system design.

9.8.1. Case 1 - SOFC Fuel Utilization

In the first sensitivity analysis case, the SOFC fuel utilization factor was varied from 0.7 to 0.9 with increments of 0.5. In this subsection, the afterburner temperature, the SOFC, and the system's electrical generation efficiency are plotted and analysed in detail. All the results of the sensitivity analysis are presented comprehensively and can be found in Appendix E.

As shown in Appendix E, several cases for the 275 kW and 225 kW power levels did not yield viable results, indicating that the system could not operate as designed under those conditions. At 275 kW with a fuel utilization of 0.9, the temperature of the afterburner product stream is insufficient to meet the system's heating requirements. Specifically, the hot stream cannot simultaneously preheat the inlet air and provide the necessary thermal input to the ORC at 150 °C. For the 225 kW case with a fuel utilization of 0.85, the exhaust gas exits the system in a vapor phase, which is incompatible with the intended system configuration. Similarly, at 225 kW and a fuel utilization of 0.9, the exhaust gas also exits in vapor form, and the afterburner outlet temperature remains too low to meet the required heating demand.

Afterburner Temperature

Figure 9.5 presents the afterburner temperature profiles as a function of the SOFC fuel utilization factor of the SOFC between 0.7 and 0.9, at three different system power levels: 225 kW, 275 kW, and 325 kW. In all cases, an increase in fuel utilization results in a noticeable decrease in afterburner temperature. This trend is expected, as higher fuel utilization in the SOFC leaves less unreacted fuel available for combustion in the afterburner, thereby reducing the thermal output and temperature level of the combustion. Additionally, higher system power levels are associated with slightly lower afterburner temperatures at equivalent fuel utilization values, due to more efficient energy extraction in the SOFC stage. These results highlight the trade-off between the SOFC's higher fuel deployment and waste heat recovery in the system.

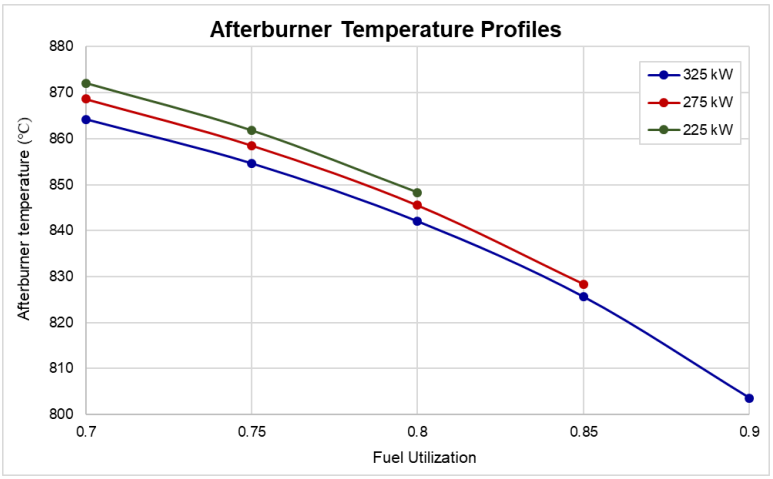

Figure 9.5: Afterburner Temperature profile as a function of the SOFC fuel utilization for three system power levels.

SOFC Efficiency

Figure 9.6 shows the SOFC efficiency based on the SOFC fuel utilization factor for three system power levels: 225 kW, 275 kW, and 325 kW. The graph indicates that SOFC efficiency consistently increases with higher fuel utilization at all power levels. When utilization increases, more input fuel is converted into electrical energy. This results in improved efficiency for the SOFC. The efficiency is slightly higher at lower system power levels, such as 225 kW, especially at mid-range utilization values, suggesting that operating conditions are more favorable at reduced loads. Still, the overall trend remains consistent across power levels, underscoring the substantial impact of fuel utilization on SOFC performance. Overall, optimizing the fuel utilization factor to achieve higher electrical efficiency in SOFC-based systems is crucial.

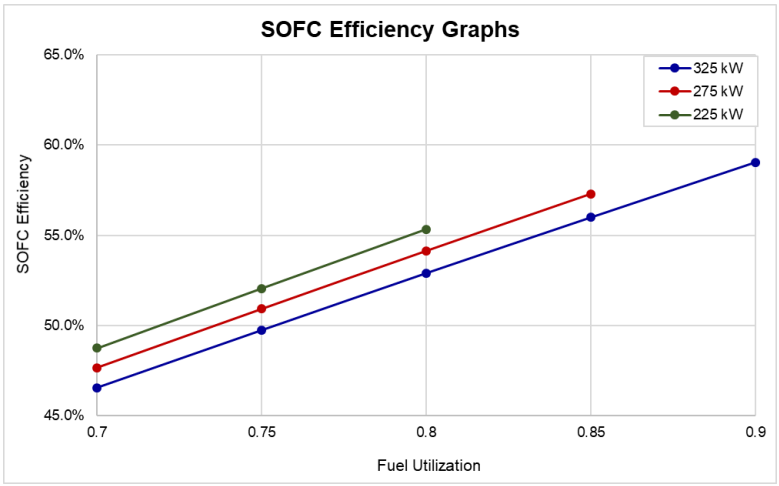

Figure 9.6: SOFC efficiency as a function of the SOFC fuel utilization for three system power levels.

System Electrical Generation Efficiency

Figure 9.7 presents the system's electrical generation efficiency based on the SOFC fuel utilization factor for three system power levels: 225 kW, 275 kW, and 325 kW. In all cases, the electrical efficiency increases with rising SOFC fuel utilization, ranging from approximately 44–48% at 0.7 utilization to 60% at 0.9 utilization. Notably, lower power outputs result in higher efficiency at a given fuel utilization. As the system's electrical generation originates mainly from the SOFC generation, it is expected that the system's electrical generation efficiency follows a similar trend to the SOFC efficiency in Figure 9.6. The selection of the operating conditions and load management is essential in optimizing the system's performance.

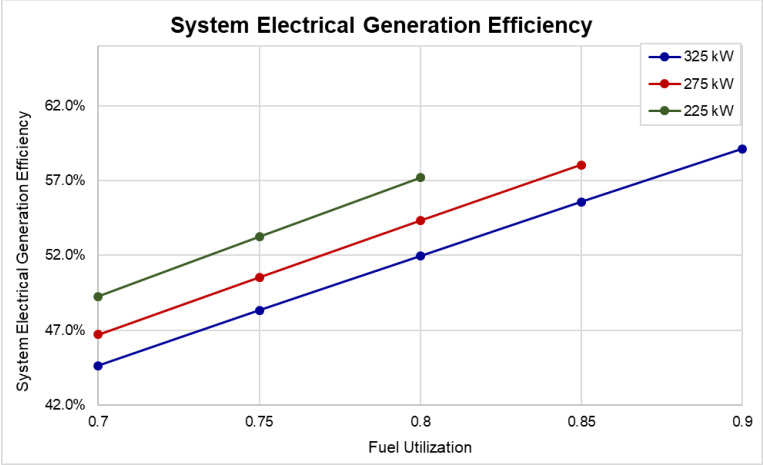

Figure 9.7: System's electrical generation efficiency as a function of the SOFC fuel utilization for three system power levels.

9.8.2. Case 2 - Solid Oxide Fuel Cell Temperature

In the second sensitivity analysis case, the SOFC operating temperature was varied from 700 to 1000 °C with increments of 50 °C. This analysis helps to understand the thermal sensitivity of the SOFC and its effect on the system's performance and operation at different system power levels. All the sensitivity analysis results are analytically presented in Appendix F. In all system power levels and temperatures, the exhaust gas exited in the vapor phase, and the heat utilization network performed successfully.

SOFC Operation

Figure 9.8 illustrates the variation of the SOFC current density and voltage with operating temperature for the three system power levels analysed. As the temperature rises from 700 °C to around 800–850 °C, the voltage increases due to enhanced reaction kinetics and reduced activation and ohmic losses. Beyond this range, the voltage declines slightly due to the decrease in the thermodynamic Nernst potential at elevated temperatures and rise in the concentration losses. The voltage analysis can be seen analytically in Table F.10 in Appendix F.

On the other hand, the current density shows a slight decrease as the temperature rises to about 850 °C. After that, it gradually increases again. This pattern results from the combined effects of voltage changes and the system's constant power needs at each power level. These factors affect the electrochemical load on the cell. Overall, the 225 kW case has the highest voltage and the lowest current density because of its lighter electrochemical load. In contrast, the 325 kW case runs at higher current densities and lower voltages, reflecting the higher power output requirement. The electrochemical behavior of the SOFC is clearly influenced by changes in both temperature and load, emphasizing their important role in determining system efficiency and output.

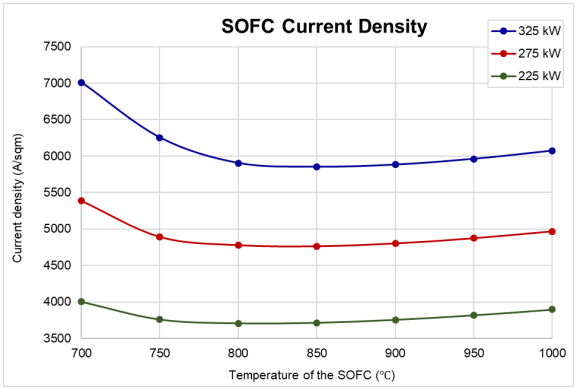

(a) Current Density profiles.

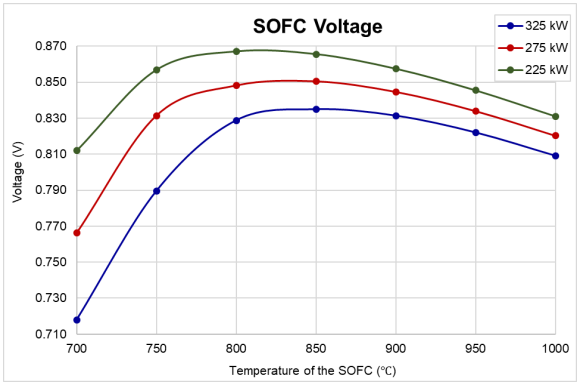

(b) Voltage profiles.

Figure 9.8: SOFC Current density and Voltage as functions of the SOFC temperature for three system power levels.

SOFC Efficiency

Figure 9.9 displays the SOFC efficiency as a function of temperature for three different system power outputs: 225 kW, 275 kW, and 325 kW. For all cases, efficiency increases with temperature up to a certain point, after which it starts to decline. The peak efficiency occurs around 800–850 °C, suggesting an optimal temperature range for the SOFC operation. At higher power levels, the efficiency gains from increasing temperature are more pronounced initially but decline more rapidly. This trend highlights the importance of selecting an optimal SOFC temperature that strikes a balance between performance and thermal management, particularly under varying load conditions.

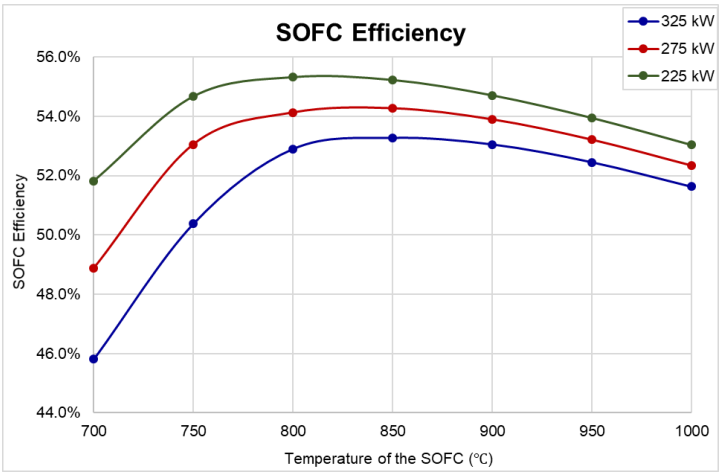

Figure 9.9: SOFC efficiency as a function of the SOFC operating temperature for three different system power levels.

Methanol Consumption

Figure 9.10 demonstrates the annual methanol consumption as a function of SOFC operating temperature for three different system power levels: 225 kW, 275 kW, and 325 kW. For all cases, methanol consumption decreases with increasing temperature up to approximately 800–850 °C, after which it begins to rise again. This trend is attributed to changes in current density. Since the inlet methanol flow is directly proportional to the current density, the methanol consumption profile follows the current density behavior. As expected, the highest methanol demand occurs at the highest power level (325 kW), while the lowest consumption corresponds to the 225 kW case. These results emphasize the importance of optimizing operating temperature to minimize fuel consumption and reduce fuel expenditure.

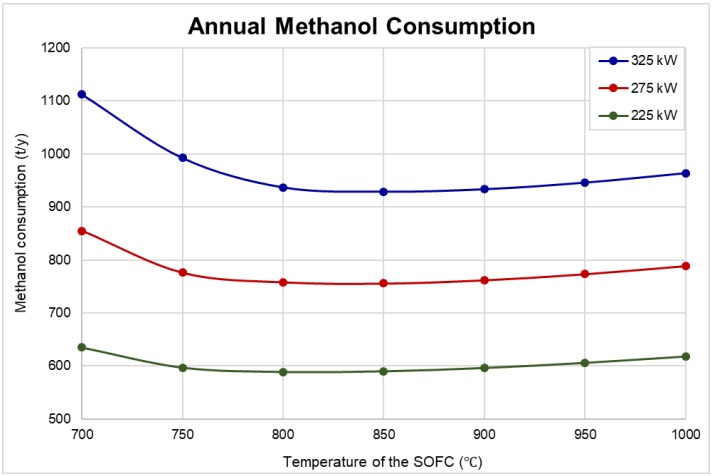

Figure 9.10: Annual consumption of methanol as a function of the SOFC operating temperature for three different system power levels.

System's Electrical Generation Efficiency

In Figure 9.11, the variation in the system's electrical generation efficiency with respect to the SOFC operating temperature for three power levels: 225 kW, 275 kW, and 325 kW is shown. In all cases, the electrical

generation efficiency increases with temperature up to an optimum point (around 800–850 °C), beyond which it begins to decline gradually. The 225 kW case reaches the highest efficiency across the entire temperature range, peaking at 57.2%, while the 325 kW case performs the lowest, with a maximum efficiency of 52.5%. As the electrical generation efficiency is a ratio of the produced power and the inlet chemical energy of methanol, its trend is influenced by the changes in the SOFC power generation (the ORC power output is constant) and the methanol consumption profiles. It is evident that the defining parameter for the system's electrical generation efficiency is the methanol flow to the system, as its variations in the ranges of 700-850°C and 900-1000°C are more significant than those in SOFC power generation. More specifically, as the methanol profiles decrease substantially in the first temperature range, the electrical generation efficiency increases significantly. Conversely, as methanol consumption increases at temperatures above 850 °C, the efficiency drops respectively.

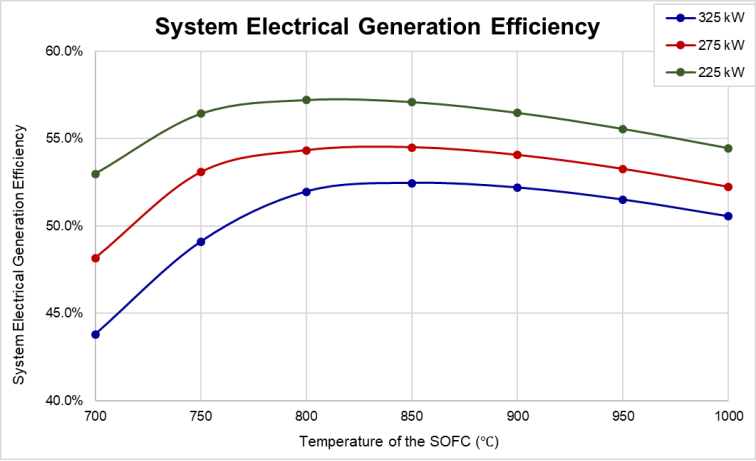

Figure 9.11: System's electrical generation efficiency as a function of the SOFC operating temperature for three different system power levels.

System's CHP Efficiency

Figure 9.12 presents the variation of system combined heat and power efficiency as a function of the SOFC operating temperature for three different system power levels: 325 kW, 275 kW, and 225 kW. Across all power levels, the system CHP efficiency initially increases with temperature, reaching a maximum in the range of 800–850 °C, beyond which a gradual decline is observed. Notably, the system operating at 225 kW consistently achieves the highest CHP efficiency across the entire temperature range, reaching a peak of 79.4%. In contrast, the 325 kW case shows the lowest CHP efficiency. This reflects the reverse relationship between power output and efficiency, caused by higher reactant flow rates and decreased heat recovery effectiveness. Overall, the figure illustrates that optimal SOFC operating temperatures and proper system sizing are essential for enhancing the system's CHP performance.

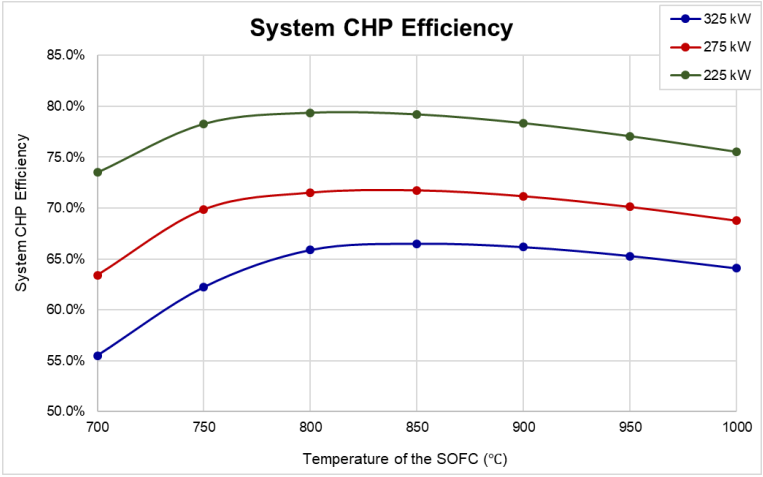

Figure 9.12: System's CHP efficiency as a function of the SOFC operating temperature for three different system power levels.

9.9. Conclusion

The results demonstrate that the integrated system operates more efficiently at lower power levels due to more favorable electrochemical and thermal conditions. The MSR section reveals consistent H_2 production with optimized heat transfer at reduced loads. The ORC delivers constant power output and efficiency of 14.6%, complementing the SOFC. The heat utilization network achieves desirable temperature targets, and the afterburner presents complete fuel combustion with excess air. The SOFC performs better at lower power, exhibiting higher voltages and efficiency. Methanol, air and water consumptions increase with power level, while the overall system achieves electrical generation efficiencies up to 57.2% and CHP efficiencies near 80%. The sensitivity analysis confirms that with optimal fuel utilization at 0.8 and SOFC temperature around 800–850 °C, performance is significantly enhanced, guiding future system design and operation.

10

Operational Costs

This chapter examines the operational cost components of the proposed MSR–SOFC–ORC system installed on a superyacht. These costs play a key role in evaluating the long-term economic feasibility of the system. Fuel expenses, SOFC stack and MSR catalyst replacement, as well as auxiliary unit maintenance, are examined in detail. By identifying and quantifying these cost drivers, the chapter establishes a foundation for assessing yearly costs under representative operating conditions. The capital expenditure (CAPEX) of the system was not included in this analysis. Estimating CAPEX is challenging due to the tailored nature of the heat recovery system. Such systems often involve custom-designed piping and equipment, which are not yet commercially standardized. As a result, cost estimations would be highly case-specific and subject to significant uncertainty.

10.1. Fuel Costs

Fuel costs are typically the most significant recurring expense, influenced by market price and fuel purity. The fuel costs are associated with methanol consumption and the replacement of the ORC working fluid, R1233zd(E). The annual methanol consumption is considered based on the system's energy demand. The Methanol Institute reported that the market price of bio-methanol was about 327 €/tn in 2021 [1].

For the ORC, the cost contribution of the working fluid is associated with the quantity lost due to annual leakage. As per the findings of Li G. [62], an estimated 2% of the working fluid mass flow is lost each year and must be replenished to maintain system performance. This recurring loss constitutes a non-negligible operational expense, especially considering the environmental and financial implications of high-purity refrigerant-grade R1233zd(E). The market price of R1233zd(E) is reported equal to 50 €/lt [8]. Table 10.1 presents the total annual fuel costs. The system operates at three different power levels throughout the year: 325 kW for 19.8% of the time, 275 kW for 26.1%, and 225 kW for 39.6%. These operating durations result in annual fuel costs of €60,663.1, €64,710.3, and €76,191.4, respectively. The total annual fuel expenditure amounts to €201,564.7.

Table 10.1: Fuel Costs breakdown.

P_{system} **(kW)**	**% in a year**	**Fuel Costs in a year**
325	19.8%	60,663.1
275	26.1%	64,710.3
225	39.6%	76,191.4
Total Annual Fuel Costs (€)		**201,564.7**

10.2. Solid Oxide Fuel Cell stack replacement Costs

The degradation of the SOFC stack significantly contributes to elevated maintenance costs. According to Skafte et al. [92], the projected average lifetime of SOFCs is expected to be 60,000 hours by 2026. As reported in 2020, the production cost of an SOFC stack is currently approximately 4000 €/kW [98]. Future projections indicate a reduction to below 800 €/kW by 2030. Table 10.2 presents the overview of SOFC stack

replacement costs, where the stack lifetime includes the percentage of time in a year when the auxiliary system is powering the yacht.

Table 10.2: SOFC replacement costs.

Parameter	Value	Unit
SOFC rated power generation	355.64	kW
Total replacement cost	1,422,544.0	€
Stack lifetime	7.61	years
Annual SOFC stack replacement cost	**186,922.3**	**€/yr**

10.3. Methanol Steam Reforming Costs

The primary operational cost of the MSR process is the replacement of catalyst. Deactivation due to sintering, coking, or poisoning necessitates periodic regeneration or replacement [85, 115]. Catalyst lifetime before sintering is highly dependent on operating conditions and typically lasts several years [93]. Optimization strategies can improve both durability and performance. While some studies report $CuO/ZnO/Al_2O_3$ catalyst lifetimes of 2–6 years with activity losses up to 60–80% [13], such degradation is impractical for methanol reforming. Amphlett et al. [7] define catalyst service life as the period during which methanol conversion remains above 85%—the autothermal point—beyond which unconverted methanol produces excess waste heat. Therefore, a conservative 2-year lifetime is assumed for cost calculations. The catalyst is commercially available for $23–$75/kg [27], and 20.15 kg is required in the reactor (see Appendix D). Assuming an average price of $50/kg, the annual catalyst replacement cost is approximately €474.5/yr. This cost is relatively minor compared to other system operating expenses. Table 10.3 summarizes catalyst costs, accounting for the percentage of annual runtime of the auxiliary system.

Table 10.3: MSR catalyst replacement costs.

Parameter	Value	Unit
Mass of catalyst	20.15	kg
Cost of catalyst	50	$/kg
Total replacement cost	1,007.5	$
Catalyst lifetime	1.8	years
Annual cost	**474.5**	**€/yr**

10.4. Other Costs

Other operational costs include auxiliary units and air control systems maintenance. The auxiliary units, such as pumps, air compressors, and control units, require power during start-up, perhaps from external sources. Air compression and flow control required for SOFC cathode operation and afterburner also add to energy and maintenance costs. In addition, startup or load transition heating requirements may need extra energy input even after heat integration with the ORC and afterburner. Lastly, pumps, heat exchangers, and ORC components require routine servicing to prevent failures from wear, fouling (accumulation of undesired products), or fluid degradation [37]. Altogether, these factors constitute a significant part of the operational costs for such integrated energy systems.

10.5. Total Operational Expenditures

Table 10.4 presents the breakdown of annual operational expenditures (OPEX) for the system. The annual fuel costs are calculated at € 201,564.7, the replacement costs of SOFC stacks are estimated at € 186,922.3 and the MSR catalyst replacement costs are € 474.5. Altogether, the total yearly OPEX for the system is calculated to be € 388,961.5.

Table 10.4: Annual OPEX breakdown.

Cost factor	Amount
Total Annual Fuel Costs (€)	201,564.7
SOFC replacement Costs (€)	186,922.3
MSR catalyst replacement costs (€)	474.5
Total Annual OPEX (€)	**388,961.5**

10.6. Conclusion

This chapter discussed the key operational costs of the studied system, highlighting fuel consumption, SOFC degradation, MSR catalyst replacement and auxiliary component maintenance. Using literature-based data and projected cost trends, annual expenditures were estimated to provide insight into system economic viability.

11

Recommendations & Conclusion

Recommendations

The current work proposes an integrated modeling, simulation and performance analysis of a MSR–SOFC–ORC system designed to meet the auxiliary power needs of a superyacht. Based on the modeling results and sensitivity analyses, the following recommendations are proposed for system improvement, practical implementation, and future research.

To begin with, the system should be operated within an SOFC temperature range of approximately 800–850 °C. This range was optimal in CHP and electrical generation efficiency when combined, delivering a balance between favorable electrochemical performance and manageable fuel consumption. Similarly, an SOFC fuel utilization factor of 0.8 is advised. Higher utilization values, particularly higher than 0.85, result in an exhaust gas temperature fall in a non-vapor phase and in a significant reduction in afterburner outlet temperatures, compromising downstream heat recovery effectiveness and the ability to meet MSR and ORC subsystems' thermal requirements. Fuel utilization optimization, therefore, becomes extremely critical not only for the SOFC performance but also for the system efficiency.

Secondly, regarding system control and design, it is recommended to further enhance the thermal integration approach. The current design relies heavily on waste heat recovery; therefore, it is essential to have proper control of the air flow and heat exchanger sizing to ensure that the inlet streams are properly preheated without requiring any supplementary electrical heating. Furthermore, operating the system at partial load conditions, particularly at 225–275 kW, yields significantly higher efficiencies compared to full-load conditions. At higher power outputs, increased reactant flow and thermal loads reduce both electrical and CHP efficiency, making part-load operation increasingly advantageous for most auxiliary power profiles.

To further improve thermal management and system efficiency, it is recommended to investigate the integration of a methanation reactor between the MSR and SOFC units. The methanation of CO and CO_2 via the exothermic reactions could be leveraged to generate additional heat that can be recovered and reused within the system's heat recovery network. This would not only enhance the overall thermal efficiency but also offer an additional degree of control over gas composition entering the SOFC. In particular, it can be beneficial under load conditions where excess hydrogen is available or where the heat output from the afterburner is insufficient. Moreover, the additional heat from methanation reduces the cooling demand of the SOFC, enabling lower air flow rates. This, in turn, reduces the power consumption of the air compressor and enhances the overall system efficiency.

The methanation process introduces methane into the anode stream, which can subsequently be reformed directly within the SOFC anode. Pianko-Oprych and Palus have explored this scenario [82], in their model of a similar SOFC system in Aspen Plus, where CH_4 was a component of the reformate gas. Within the SOFC anode, methane was reformed via the reaction $CH_4 + H_2O \rightarrow 3\,H_2 + CO$, thereby contributing to internal hydrogen production. This confirms that methane can be effectively utilized within the SOFC, and its behavior can be predicted through validated reforming kinetics in the anode environment. Despite these benefits, integrating a methanation reactor would cause an increase in the system's capital expenditures due to the additional reactor and associated control infrastructure. Careful techno-economic evaluation is therefore necessary to assess whether the performance improvements justify the added investment.

From a modeling perspective, the adopted MSR kinetic model does not account for CO formation and the two side reactions of MSR. To address this, an RGibbs reactor block was implemented in the Aspen Plus model. While this approach maintains chemical equilibrium, future modeling could benefit from incorporating a more detailed and comprehensive kinetic model that includes side reactions and intermediate species, such as CO. This would enable a more realistic prediction of the reformate composition entering the SOFC. In addition, it is recommended that a second-law thermodynamic study—an exergy analysis—be conducted in a subsequent stage of research. Such an analysis would help identify major exergy losses within the system and support improvements in the heat recovery network and overall energy utilization. Lastly, dynamic simulations are recommended for future studies, as the current model primarily focuses on steady-state operation. Adding transients, such as startup, shutdown, or load-following operations, would provide more representative system sizing and flexibility, as well as control requirements in real marine applications.

Regarding the SOFC sizing approach, it is recommended to use the iterative process outlined in this work rather than the simplified single-step method used in the simulations. The iterative approach provides more accurate convergence of the SOFC active area by accounting for feedback from auxiliary components such as the compressor and SWRO unit, and is therefore better suited for precise stack sizing.

An additional improvement could be the recovery of water from the SOFC exhaust through condensation. This recovered water could reduce the power demand on the SWRO unit, thereby minimizing the total area and power requirement of the water purification and SOFC subsystem. This not only simplifies system integration on space-constrained marine vessels but also improves overall energy efficiency.

In this work, pure methanol was used as the fuel input for the simulations. While this simplifies the modeling process, it does not reflect the varying composition of real-world bio-methanol. As discussed in subsection 3.2.3, bio-methanol composition, depending on its source, which can contain impurities and other components, differs significantly between suppliers and sources. Simulating realistic commercial bio-methanol compositions would yield more accurate and valid findings. However, it also introduces complexity and uncertainty due to the industry's non-uniformity. That is why pure methanol was utilized in this project. As noted in subsection 3.3.2, the maritime industry has defined purity specifications for methanol intended for fuel cell applications, highlighting the growing importance of this issue. Impurities present in bio-methanol may also have a harmful impact on catalyst performance and lifetime in the MSR reactor; however, the specific degradation mechanisms are not yet deeply studied. This presents a significant area for future research.

Regarding practical implementation, temperature monitoring and control—particularly of the SOFC exhaust and afterburner outlet—is necessary. These temperatures are crucial to the effectiveness of heat recovery and overall thermal integration. Secondly, the SOFC stack needs to be selected based on its commercialization and resistance to fuel variability and thermal cycling, as the cost of replacing stacks is a significant factor in operational expenses. Supply logistics of methanol and bunkering must also be accounted for. As methanol infrastructure expands, the fuel must be readily available at the yacht's ports of operation, and careful planning may be necessary for efficient operation. Lastly, a detailed study of the system's component configuration for real-life implementation on a yacht, including spatial constraints, should be conducted. In this way, the system can be accurately sized and fitted to the space of the ship.

Looking forward, multiple potential directions for future research are identified. Long-term degradation effects of both the SOFC stack and the MSR catalyst should be studied under realistic operational cycles to better estimate maintenance intervals and costs. Additionally, a further techno-economic analysis can follow, where the capital expenditures are calculated with market prices for each subsystem and component. In this way, the LCOE can be calculated for the system and compared to other SOFC-integrated or marine diesel engine systems. This will define the financial and commercial viability and competitiveness of the proposed system in terms of lifecycle costs, operational savings, payback period, and return on investment relative to conventional and emerging maritime power technologies. Finally, a comprehensive lifecycle environmental analysis, including emissions through different bio-methanol supply pathways, production emissions of the components themselves, and end-of-life considerations, would draw a better overall picture of the system's sustainability impact in the maritime sector.

Conclusion

This thesis project explored the development and evaluation of an MSR–SOFC–ORC system designed for the auxiliary power demands of a superyacht through a comprehensive analysis. The system utilizes bio-methanol, a sustainable carbon-neutral fuel, which undergoes steam reforming to produce a hydrogen-rich gas as feed to an SOFC stack. The research identified optimal operating parameters and integration strategies to maximize both electrical output and thermal utilization by modeling and simulating the system in Aspen Plus.

The findings revealed that the system achieves electrical generation efficiencies of up to 57.2% and CHP efficiencies of 79.4% at partial loads, closely aligning with the performance of similar integrated systems reported in the literature. Compared to conventional marine diesel generators, which typically operate at 25–45% electrical generation efficiency, the proposed system delivers significantly higher performance while also producing substantially lower greenhouse gas emissions. The importance of thermal integration is also highlighted, particularly the positioning of the afterburner and the multi-stage air preheating strategy, which were critical to system feasibility. Ultimately, an iterative approach to SOFC active area sizing proved to be more precise than one-time estimates, considering input from air compressor and SWRO demands.

Incorporating the varying compositions of commercial bio-methanol into the simulations is recommended for future work. However, due to the added modeling complexity and for consistency, pure methanol was used in this study. Moreover, dynamic simulations, comprehensive MSR kinetic models, and long-term degradation analysis will be essential to refine the design further and assess its operational viability. The results clearly show that, beyond efficiency gains, operating the system on bio-methanol directly supports the IMO's decarbonization targets and the broader global climate goals for the maritime sector, offering a viable pathway to replace fossil-based auxiliary systems. Overall, the findings confirm the technical viability and efficiency advantages of implementing a bio-methanol-fueled MSR–SOFC–ORC system for maritime applications, contributing to the ongoing transition towards greener and more sustainable power technologies in the maritime sector.

Beyond the superyacht application, the studied system can be potentially used in other applications requiring compact, high-efficiency, and low-emission energy solutions. Examples of other transport applications include ferries and heavy-duty vehicles, such as trucks or electric buses, where the system can be utilized as a green auxiliary power unit. Other applications could be remote off-grid locations requiring combined heat and power (islands or research stations). The system could also work as a reliable, constant and quiet backup power source for critical infrastructure such as data centers. Lastly, its compatibility with liquid bio-methanol makes it especially attractive for applications where hydrogen infrastructure and storage is limited or challenging.

The outcomes of this research also contribute to the socio-economic transition toward sustainable energy in the maritime sector. This study has demonstrated the feasibility of bio-methanol-fueled SOFC-based systems, supporting the growing research for greener auxiliary maritime power technologies aligned with global decarbonization goals. The use of bio-methanol, a renewable and increasingly available fuel, presents an economically viable alternative to fossil-based marine fuels and is compliant with the emission regulations of the IMO. Moreover, the system's efficiency can reduce operational fuel costs over time, offering long-term savings despite a higher upfront investment. The adoption of such a system could also inspire innovation and job creation in green shipbuilding, bio-fuel production, and manufacturing. However, challenges remain regarding the scalability, fuel standardization, and infrastructure readiness for bio-methanol distribution. In this way, this research does not only contribute to technical knowledge but also to a broader socio-economic context regarding clean energy adoption, energy security, and sustainable marine mobility.

References

[1] International Renewable Energy Agency (IRENA). *Innovation Outlook: Renewable Methanol*. Jan. 2021. URL: https://www.irena.org/-/media/Files/IRENA/Agency/Publication/2021/Jan/IRENA_Innovation_Renewable_Methanol_2021.pdf.

[2] A□Gas. *Technical Information: R□123*. https://www.agas.com/media/4tbjckam/r123-technical-information.pdf. 2025.

[3] Jörg Adolf et al. "Shell Hydrogen Study Energy of the Future? Sustainable Mobility through Fuel Cells and H2". In: (Jan. 2017). DOI: 10.13140/RG.2.2.31848.57604.

[4] Mansur Aliyu and Abdullah A. AlZahrani. "Integrated SMR-SOFC system for efficient hydrogen and power production". In: *International Journal of Hydrogen Energy* (2024). ISSN: 0360-3199. DOI: https://doi.org/10.1016/j.ijhydene.2024.12.354. URL: https://www.sciencedirect.com/science/article/pii/S0360319924055678.

[5] American Bureau of Shipping. *Methanol Bunkering: Technical Advisory*. January 2021. Houston, TX, 2021.

[6] Amogh Amladi et al. "Hot air recirculation enlarges efficient operating window of reversible solid oxide cell systems: A thermodynamic study of energy storage using ammonia". In: *Applied Energy* 355 (2024), p. 122276. ISSN: 0306-2619. DOI: https://doi.org/10.1016/j.apenergy.2023.122276. URL: https://www.sciencedirect.com/science/article/pii/S0306261923016409.

[7] J.C. Amphlett et al. "A Deactivation Model for Methanol-Steam Reformation on Cu/ZnO/Al2O3 Catalyst for Optimizing the Production of Fuel-Cell Hydrogen". In: *Catalyst Deactivation 2001*. Ed. by J.J. Spivey, G.W. Roberts, and B.H. Davis. Vol. 139. Studies in Surface Science and Catalysis. Elsevier, 2001, pp. 205–212. DOI: https://doi.org/10.1016/S0167-2991(01)80199-3. URL: https://www.sciencedirect.com/science/article/pii/S0167299101801993.

[8] Cordin Arpagaus et al. "High Temperature Heat Pump using HFO and HCFO refrigerants - System design, simulation, and first experimental results". In: Aug. 2018.

[9] S.D. Badmaev, V.D. Belyaev, D.I. Potemkin, et al. "Methanol Decomposition to Synthesis Gas over Supported Platinum-Containing Catalysts". In: *Catalysis in Industry* 15 (2023), pp. 367–373. DOI: 10.1134/S2070050423040037. URL: https://link.springer.com/article/10.1134/S2070050423040037.

[10] Sukhvinder Badwal et al. "ChemInform Abstract: Review of Progress in High Temperature Solid Oxide Fuel Cells". In: *Journal of the australian ceramics society* 50 (Apr. 2014), pp. 23–37. DOI: 10.1002/chin.201531316.

[11] Francesco Baldi et al. "The role of solid oxide fuel cells in future ship energy systems". In: *Energy* 194 (2020), p. 116811. ISSN: 0360-5442. DOI: https://doi.org/10.1016/j.energy.2019.116811. URL: https://www.sciencedirect.com/science/article/pii/S036054421932506X.

[12] Jaime Barros. "Modeling the Electric Power Consumption of a Yacht". MA thesis. TU Delft, Nov. 2022. DOI: 10.13140/RG.2.2.36160.92162.

[13] N. Barrow et al. "Doubling the life of Cu/ZnO methanol synthesis catalysts via use of Si as a structural promoter to inhibit sintering". In: *Science Advances* 10.3 (2024), eadk2081. DOI: 10.1126/sciadv.adk2081.

[14] Ameen M. Bassam et al. "Design, modelling and simulation of a hybrid fuel cell propulsion system for a domestic ferry". In: *Proceedings of PRADS 2016*. National Oceanography Centre, Natural Environment Research Council, UK. Fluid Structure Interactions Group, University of Southampton, UK. Copenhagen, Denmark: Naval Architecture and Marine Engineering Department, Port Said University, Egypt, Sept. 2016.

[15] L. van Biert et al. "A review of fuel cell systems for maritime applications". In: *Journal of Power Sources* 327 (2016), pp. 345–364. ISSN: 0378-7753. DOI: https://doi.org/10.1016/j.jpowsour.2016.07.007. URL: https://www.sciencedirect.com/science/article/pii/S0378775316308631.

[16] G. Botta et al. “Thermodynamic evaluation of bi-directional solid oxide cell systems including year-round cumulative exergy analysis”. In: *Applied Energy* 226 (2018), pp. 1100–1118. ISSN: 0306-2619. DOI: https://doi.org/10.1016/j.apenergy.2018.05.061. URL: https://www.sciencedirect.com/science/article/pii/S0306261918307712.

[17] Konstantinos Braimakis and Sotirios Karellas. “Chapter 12 - Organic Rankine cycle systems for waste heat recovery in thermal power plants”. In: *Small Scale Power Generation Handbook*. Ed. by Umberto Desideri and Lorenzo Ferrari. Academic Press, 2025, pp. 309–339. ISBN: 978-0-12-821672-9. DOI: https://doi.org/10.1016/B978-0-12-821672-9.00013-7. URL: https://www.sciencedirect.com/science/article/pii/B9780128216729000137.

[18] Annamaria Buonomano et al. “Hybrid solid oxide fuel cells–gas turbine systems for combined heat and power: A review”. In: *Applied Energy* 156 (2015), pp. 32–85. ISSN: 0306-2619. DOI: https://doi.org/10.1016/j.apenergy.2015.06.027. URL: https://www.sciencedirect.com/science/article/pii/S0306261915007850.

[19] China Classification Society. *Guidelines for Ships Using Methanol/Ethanol Fuel*. GD16-2022. Guidance Notes. Effective from July 1, 2022. Beijing, 2022.

[20] CIMAC Working Group 7. *CIMAC Guideline: FAQs Regarding ISO 6583:2024 for Methanol as a Marine Fuel*. 2025. URL: https://www.cimac.com/cms/upload/workinggroups/WG7/CIMAC_Guideline_FAQ_ISO_6583_Methanol_01_2025.pdf.

[21] Climalife. *R-1234ze Solstice® ze*. https://www.climalife.co.uk/r1234ze. 2025.

[22] Climalife. *R□1233zd Solstice® zd*. https://www.climalife.co.uk/r-1233zd. 2025.

[23] “Chapter 17 - Chemical reactors”. In: *Chemical Process Equipment (Second Edition)*. Ed. by James R. Couper et al. Second Edition. Burlington: Gulf Professional Publishing, 2005, pp. 583–642. ISBN: 978-0-7506-7510-9. DOI: https://doi.org/10.1016/B978-075067510-9/50049-8. URL: https://www.sciencedirect.com/science/article/pii/B9780750675109500498.

[24] Francesco Dalena et al. “Chapter 1 - Methanol Production and Applications: An Overview”. In: *Methanol*. Ed. by Angelo Basile and Francesco Dalena. Elsevier, 2018, pp. 3–28. ISBN: 978-0-444-63903-5. DOI: https://doi.org/10.1016/B978-0-444-63903-5.00001-7. URL: https://www.sciencedirect.com/science/article/pii/B9780444639035000017.

[25] Delft University of Technology. *Summary Table with Heating Values and CO_2 Emissions*. https://ocw.tudelft.nl/wp-content/uploads/Summary_table_with_heating_values_and_CO2_emissions.pdf. n.d.

[26] DNV. *Alternative Fuels Insight Presentation*. https://www.oceanspacemedia.com/files/2024/10/03/2024-10-01_DNV-AFI-presentation.pdf. Oct. 2024.

[27] Electro Power Cell Energy Technology (Shanghai) Co., Ltd. *Copper Zinc Aluminum Methanol Reforming Catalyst Efficient Hydrogen Generator for Green Energy Production*. 2025. URL: https://www.alibaba.com/product-detail/Copper-Zinc-Aluminum-Methanol-Reforming-Catalyst_1601244666112.html.

[28] Ahmed G. Elkafas et al. “Fuel Cell Systems for Maritime: A Review of Research Development, Commercial Products, Applications, and Perspectives”. In: *Processes* 11.1 (2023). ISSN: 2227-9717. DOI: 10.3390/pr11010097. URL: https://www.mdpi.com/2227-9717/11/1/97.

[29] B. Emonts et al. “Compact methanol reformer test for fuel-cell powered light-duty vehicles”. In: *Journal of Power Sources* 71.1 (1998), pp. 288–293. ISSN: 0378-7753. DOI: https://doi.org/10.1016/S0378-7753(97)02724-9. URL: https://www.sciencedirect.com/science/article/pii/S0378775397027249.

[30] Torr Engenharia. *Heat Exchanger Design Handbook*. https://www.torr-engenharia.com.br/wp-content/uploads/2011/05/exchanger.pdf. 2011.

[31] Wenchao Fang et al. “Predicting heat transfer coefficient of a shell-and-plate, moving packed-bed particle-to-sCO2 heat exchanger for concentrating solar power”. In: *Energy* 217 (2021), p. 119389. ISSN: 0360-5442. DOI: https://doi.org/10.1016/j.energy.2020.119389. URL: https://www.sciencedirect.com/science/article/pii/S0360544220324968.

[32] *Feadship*. https://www.feadship.nl/. Feadship.

[33] Zuhang Fu et al. “Fuel cell and hydrogen in maritime application: A review on aspects of technology, cost and regulations”. In: *Sustainable Energy Technologies and Assessments* 57 (2023), p. 103181. ISSN: 2213-1388. DOI: https://doi.org/10.1016/j.seta.2023.103181. URL: https://www.sciencedirect.com/science/article/pii/S2213138823001741.

[34] Gabriel Garcia et al. “A comprehensive review of hydrogen production from methanol thermochemical conversion for sustainability”. In: *Energy* 217 (2021), p. 119384. ISSN: 0360-5442. DOI: https://doi.org/10.1016/j.energy.2020.119384. URL: https://www.sciencedirect.com/science/article/pii/S0360544220324919.

[35] Emeline Georges et al. “Design of a small-scale organic Rankine cycle engine used in a solar power plant”. In: *International Journal of Low Carbon Technologies* 8 (June 2013). DOI: 10.1093/ijlct/ctt030.

[36] J. Gerritse et al. “Greenhouse Gas Emission Reduction Strategies in Maritime Transport”. In: (2023). URL: https://publications.tno.nl/publication/34640817/zpBGh5/gerritse-2023-green.pdf.

[37] Donna Post Guillen and Jalal Zia. *Modifications and Optimization of the Organic Rankine Cycle to Improve the Recovery of Waste Heat*. Tech. rep. Prepared for the U.S. Department of Energy, Assistant Secretary for Energy Efficiency and Renewable Energy, under DOE Idaho Operations Office Contract DE-AC07-05ID14517. Idaho Falls, Idaho 83415: Idaho National Laboratory, Sept. 2013. URL: http://www.inl.gov.

[38] Engin Güler and Selma Ergin. “Investigation of a solid oxide fuel cell integrated into an internal combustion engine with carbon capture for maritime applications”. In: *Energy Conversion and Management* 314 (2024), p. 118660. ISSN: 0196-8904. DOI: https://doi.org/10.1016/j.enconman.2024.118660. URL: https://www.sciencedirect.com/science/article/pii/S0196890424006010.

[39] C. Hamelinck and M. Bunse. “The carbon footprint of methanol produced from various feedstocks”. In: (Feb. 4, 2022). URL: https://www.studiogearup.com/the-carbon-footprint-of-methanol-produced-from-various-feedstocks/ (visited on 06/12/2022).

[40] Maximilian Hauck, Stephan Herrmann, and Hartmut Spliethoff. “Simulation of a reversible SOFC with Aspen Plus”. In: *International Journal of Hydrogen Energy* 42.15 (2017), pp. 10329–10340. ISSN: 0360-3199. DOI: https://doi.org/10.1016/j.ijhydene.2017.01.189. URL: https://www.sciencedirect.com/science/article/pii/S0360319917303579.

[41] H.M.D.P. Herath et al. “Working fluid selection of Organic Rankine Cycles”. In: *Energy Reports* 6 (2020). 2020 The 7th International Conference on Power and Energy Systems Engineering, pp. 680–686. ISSN: 2352-4847. DOI: https://doi.org/10.1016/j.egyr.2020.11.150. URL: https://www.sciencedirect.com/science/article/pii/S2352484720315754.

[42] Honeywell Refrigerants. *Genetron® 245fa (R□245fa)*. https://www.honeywell-refrigerants.com/europe/product/genetron-245fa/. 2025.

[43] Jiuqing Hu et al. “Investigation of the electrochemical performance of solid oxide fuel cells with methanol internal reforming”. In: *International Journal of Electrochemical Science* 19.5 (2024), p. 100550. ISSN: 1452-3981. DOI: https://doi.org/10.1016/j.ijoes.2024.100550. URL: https://www.sciencedirect.com/science/article/pii/S1452398124000919.

[44] Yang Hu et al. “Experimental evaluation of methanol steam reforming reactor heated by catalyst combustion for kW-class SOFC”. In: *International Journal of Hydrogen Energy* 48.12 (2023), pp. 4649–4664. ISSN: 0360-3199. DOI: https://doi.org/10.1016/j.ijhydene.2022.10.274. URL: https://www.sciencedirect.com/science/article/pii/S0360319922051576.

[45] Yang Hu et al. “Experimental evaluation of SOFC fuel adaptability and power generation performance based on MSR”. In: *Fuel Processing Technology* 250 (2023), p. 107919. ISSN: 0378-3820. DOI: https://doi.org/10.1016/j.fuproc.2023.107919. URL: https://www.sciencedirect.com/science/article/pii/S0378382023002679.

[46] SGS INSPIRE. *Global Quality Specifications and Requirements for Methanol as a Fuel for Marine Applications*. 2023. URL: https://inspire.sgs.com/content/101106486/global-quality-specifications-and-requirements-for-methanol-as-a-fuel-for-marine-applications.

[47] Methanol Institute. *Marine Methanol Report*. https://www.methanol.org/wp-content/uploads/2023/05/Marine_Methanol_Report_Methanol_Institute_May_2023.pdf. May 2023.

[48] Intergovernmental Panel on Climate Change. *Contribution of Working Group III to the Sixth Assessment Report of the Intergovernmental Panel on Climate Change, Mitigation of Climate Change*. IPCC, 2022. Chap. 2.

[49] International Maritime Organization. *Energy Efficiency Technologies Information Portal*. https://greenvoyage2050.imo.org/energy-efficiency-technologies-information-portal/. 2025.

[50] International Maritime Organization. *Interim Guidelines for the Safety of Ships Using Methyl/Ethyl Alcohol as Fuel*. MSC.1/Circ.1621. Dec. 7, 2020. URL: https://www.register-iri.com/wp-content/uploads/MSC.1-Circ.1621.pdf.

[51] International Maritime Organization (IMO). *2023 IMO Strategy on Reduction of GHG Emissions from Ships*. Resolution MEPC.377(80), adopted on 7 July 2023. London: Marine Environment Protection Committee (MEPC), 2023. URL: https://www.imo.org.

[52] International Maritime Organization (IMO). *Fourth IMO GHG Study 2020*. Tech. rep. International Maritime Organization, 2020. URL: https://maritimecyprus.com/wp-content/uploads/2021/03/4th-IMO-GHG-Study-2020.pdf.

[53] International Organization for Standardization. *ISO 6583:2024 – Methanol as a Marine Fuel*. Standard published by ISO, Geneva, Switzerland. 2024. URL: https://www.iso.org/obp/ui/en/#iso:std:iso:6583:ed-1:v1:en.

[54] S.K. Kamarudin, F. Achmad, and W.R.W. Daud. "Overview on the application of direct methanol fuel cell (DMFC) for portable electronic devices". In: *International Journal of Hydrogen Energy* 34.16 (2009). 4th Dubrovnik Conference, pp. 6902–6916. ISSN: 0360-3199. DOI: https://doi.org/10.1016/j.ijhydene.2009.06.013. URL: https://www.sciencedirect.com/science/article/pii/S0360319909008829.

[55] Jungbin Kim et al. "A comprehensive review of energy consumption of seawater reverse osmosis desalination plants". In: *Applied Energy* 254 (2019), p. 113652. ISSN: 0306-2619. DOI: https://doi.org/10.1016/j.apenergy.2019.113652. URL: https://www.sciencedirect.com/science/article/pii/S030626191931339X.

[56] Sehwa Kim et al. "Steam reforming of methanol for ultra-pure H2 production in a membrane reactor: Techno-economic analysis". In: *International Journal of Hydrogen Energy* 44.4 (2019). The 2nd International Conference on Alternative Fuels and Energy (ICAFE2017), pp. 2330–2339. ISSN: 0360-3199. DOI: https://doi.org/10.1016/j.ijhydene.2018.08.087. URL: https://www.sciencedirect.com/science/article/pii/S0360319918326284.

[57] Arunabha Kundu, Yong Gun Shul, and Dong Hyun Kim. "Chapter Seven - Methanol Reforming Processes". In: *Advances in Fuel Cell*. Ed. by T.S. Zhao, K.-D. Kreuer, and Trung Van Nguyen. Vol. 1. Advances in Fuel Cells. Elsevier Science, 2007, pp. 419–472. DOI: https://doi.org/10.1016/S1752-301X(07)80012-3. URL: https://www.sciencedirect.com/science/article/pii/S1752301X07800123.

[58] U. Larsen, O. Sigthorsson, and F. Haglind. "A comparison of advanced heat recovery power cycles in a combined cycle for large ships". In: *Energy* 74 (2014), pp. 260–268. DOI: 10.1016/j.energy.2014.06.096.

[59] Steven Lecompte et al. "Review of organic Rankine cycle (ORC) architectures for waste heat recovery". In: *Renewable and Sustainable Energy Reviews* 47 (2015), pp. 448–461. ISSN: 1364-0321. DOI: https://doi.org/10.1016/j.rser.2015.03.089. URL: https://www.sciencedirect.com/science/article/pii/S1364032115002427.

[60] Clara Ng Kay Leng. *Marine Methanol Fuel Specification and Engine Technologies*. MESD Seminar, 1st December 2023. 2023. URL: https://www.ntu.edu.sg/docs/librariesprovider79/publication/mesd-seminar-2023-marine-methanol-fuel-specification-and-engine-technologies.pdf?sfvrsn=318084f2_3.

[61] Chengjie Li et al. "Exergetic and exergoeconomic evaluation of an SOFC-Engine-ORC hybrid power generation system with methanol for ship application". In: *Fuel* 357 (2024), p. 129944. ISSN: 0016-2361. DOI: https://doi.org/10.1016/j.fuel.2023.129944. URL: https://www.sciencedirect.com/science/article/pii/S0016236123025589.

[62] G. Li. “Organic Rankine cycle environmental impact investigation under various working fluids and heat domains concerning refrigerant leakage rates”. In: *International Journal of Environmental Science and Technology* 16 (2019), pp. 431–450. DOI: 10.1007/s13762-018-1686-y. URL: https://www.researchgate.net/publication/325080622_Organic_Rankine_cycle_environmental_impact_investigation_under_various_working_fluids_and_heat_domains_concerning_refrigerant_leakage_rates.

[63] Qingshan Li et al. “Dynamic modelling and characteristics analysis of methanol steam reforming solid oxide fuel cell system”. In: *Renewable Energy* 241 (2025), p. 122187. ISSN: 0960-1481. DOI: https://doi.org/10.1016/j.renene.2024.122187. URL: https://www.sciencedirect.com/science/article/pii/S0960148124022559.

[64] Yanyong Liu et al. “Methanol decomposition to synthesis gas at low temperature over palladium supported on ceria–zirconia solid solutions”. In: *Applied Catalysis A: General* 210.1 (2001), pp. 301–314. ISSN: 0926-860X. DOI: https://doi.org/10.1016/S0926-860X(00)00817-6. URL: https://www.sciencedirect.com/science/article/pii/S0926860X00008176.

[65] Juan Sebastian Lopez-Echeverry, Simon Reif-Acherman, and Eduard Araujo-Lopez. “Peng-Robinson equation of state: 40 years through cubics”. In: *Fluid Phase Equilibria* 447 (2017), pp. 39–71. ISSN: 0378-3812. DOI: https://doi.org/10.1016/j.fluid.2017.05.007. URL: https://www.sciencedirect.com/science/article/pii/S0378381217301851.

[66] Jincheng Ma et al. “Optimization of heat transfer device and analysis of heat mass transfer on the finned multi-tubular metal hydride tank”. In: *International Journal of Hydrogen Energy* 39.25 (2014), pp. 13583–13595. ISSN: 0360-3199. DOI: https://doi.org/10.1016/j.ijhydene.2014.03.016. URL: https://www.sciencedirect.com/science/article/pii/S0360319914006296.

[67] Yue Ma et al. “Efficient and sustainable power propulsion for all-electric ships: An integrated methanol-fueled SOFC-sCO2 system”. In: *Renewable Energy* 230 (2024), p. 120822. ISSN: 0960-1481. DOI: https://doi.org/10.1016/j.renene.2024.120822. URL: https://www.sciencedirect.com/science/article/pii/S0960148124008905.

[68] Deqing Mei et al. “A performance study of methanol steam reforming in an A-type microchannel reactor”. In: *International Journal of Hydrogen Energy* 39.31 (2014), pp. 17690–17701. ISSN: 0360-3199. DOI: https://doi.org/10.1016/j.ijhydene.2014.08.114. URL: https://www.sciencedirect.com/science/article/pii/S0360319914024550.

[69] Zhang Mengyuan et al. “Recent Advances in Methanol Steam Reforming Catalysts for Hydrogen Production”. In: *Catalysts* 15 (Jan. 2025), p. 36. DOI: 10.3390/catal15010036.

[70] Methanex Corporation. *Methanol North America Safety Data Sheet (SDS)*. https://www.methanex.com/wp-content/uploads/UL-METHANOL-NA_Methanol_NGHS_English_01.31.2025v6.pdf. 2025.

[71] Methanol Institute. *Carbon Footprint of Methanol*. 2022. URL: https://www.methanol.org/wp-content/uploads/2022/01/CARBON-FOOTPRINT-OF-METHANOL-PAPER_1-31-22.pdf.

[72] Methanol Institute. *Physical Properties of Pure Methanol*. https://www.methanol.org/wp-content/uploads/2016/06/Physical-Properties-of-Pure-Methanol.pdf. 2016.

[73] Methanol Institute. *Safe Handling Manual, 5th Edition*. 2020. URL: https://www.methanol.org/wp-content/uploads/2020/03/Safe-Handling-Manual_5th-Edition_Final.pdf.

[74] Joan M. Ogden, Thomas G. Kreutz, and Margaret M. Steinbugler. “Fuels for fuel cell vehicles”. In: *Fuel Cells Bulletin* 3.16 (2000), pp. 5–13. ISSN: 1464-2859. DOI: https://doi.org/10.1016/S1464-2859(00)86613-4. URL: https://www.sciencedirect.com/science/article/pii/S1464285900866134.

[75] Lukman Ahmed Omeiza et al. “Chapter 14 - Solid oxide fuel cells (SOFCs)”. In: *Electrochemical Energy Storage Technologies Beyond LI-ION Batteries*. Ed. by Guanjie He. Elsevier, 2025, pp. 405–424. ISBN: 978-0-443-15514-7. DOI: https://doi.org/10.1016/B978-0-443-15514-7.00006-0. URL: https://www.sciencedirect.com/science/article/pii/B9780443155147000060.

[76] Karittha Im-orb, Anh N. Phan, and Amornchai Arpornwichanop. “Bio-methanol production from oil palm residues: A thermodynamic analysis”. In: *Energy Conversion and Management* 226 (2020), p. 113493. ISSN: 0196-8904. DOI: https://doi.org/10.1016/j.enconman.2020.113493. URL: https://www.sciencedirect.com/science/article/pii/S0196890420310256.

[77] Ahmed Osman et al. “Hydrogen, ammonia and methanol for marine transportation”. In: *Environmental Chemistry Letters* 22 (June 2024). DOI: 10.1007/s10311-024-01757-9.

[78] Orhan Özcan and Ayşe Nilgün Akın. “Methanol steam reforming kinetics using a commercial CuO/ZnO/Al2O3 catalyst: Simulation of a reformer integrated with HT-PEMFC system”. In: *International Journal of Hydrogen Energy* 48.60 (2023). The 6th International Hydrogen Technologies Congress (IHTEC-2022), pp. 22777–22790. ISSN: 0360-3199. DOI: https://doi.org/10.1016/j.ijhydene.2023.01.093. URL: https://www.sciencedirect.com/science/article/pii/S0360319923001295.

[79] Byung-Sik Park et al. “Review of Organic Rankine Cycle experimental data trends”. In: *Energy Conversion and Management* 173 (2018), pp. 679–691. ISSN: 0196-8904. DOI: https://doi.org/10.1016/j.enconman.2018.07.097. URL: https://www.sciencedirect.com/science/article/pii/S0196890418308379.

[80] Sang-Chan Park et al. “Performance analysis of an organic Rankine cycle with an internal heat exchanger considering turbine pressure ratio and efficiency”. In: *Energy* 285 (2023), p. 129507. ISSN: 0360-5442. DOI: https://doi.org/10.1016/j.energy.2023.129507. URL: https://www.sciencedirect.com/science/article/pii/S0360544223029018.

[81] M. Pehnt. “Life-cycle analysis of fuel cell system components”. In: *Handbook of Fuel Cells – Fundamentals, Technology and Applications*. Ed. by Wolf Vielstich, Arnold Lamm, and Hubert A. Gasteiger. Vol. 4.13. Chichester: John Wiley & Sons, Ltd, 2003, pp. 1293–1317. ISBN: 0-471-49926-9.

[82] Paulina Pianko-Oprych and Mateusz Palus. “Simulation of SOFCs based power generation system using Aspen”. In: *Polish Journal of Chemical Technology* 19 (Jan. 2017). DOI: 10.1515/pjct-2017-0061.

[83] Hossein Pourrahmani, Chengzhang Xu, and Jan Van herle. “Organic Rankine Cycle as the Waste Heat Recovery Unit of Solid Oxide Fuel Cell: A Novel System Design for the Electric Vehicle Charging Stations Using Batteries as a Backup/Storage Unit”. In: *Batteries* 8.10 (2022). ISSN: 2313-0105. DOI: 10.3390/batteries8100138. URL: https://www.mdpi.com/2313-0105/8/10/138.

[84] Masoud Rokni. “Thermodynamic and thermoeconomic analysis of a system with biomass gasification, solid oxide fuel cell (SOFC) and Stirling engine”. In: *Energy* 76 (2014), pp. 19–31. ISSN: 0360-5442. DOI: https://doi.org/10.1016/j.energy.2014.01.106. URL: https://www.sciencedirect.com/science/article/pii/S0360544214001285.

[85] Mohse Rostami et al. “A review study on methanol steam reforming catalysts: Evaluation of the catalytic performance, characterizations, and operational parameters”. In: *AIP Advances* 13 (Mar. 2023), p. 030701. DOI: 10.1063/5.0137706.

[86] Concetta Ruocco et al. “Intensified methanol steam reforming over active and stable CeO2-Al2O3 supported catalysts”. In: *Fuel Processing Technology* 272 (2025), p. 108212. ISSN: 0378-3820. DOI: https://doi.org/10.1016/j.fuproc.2025.108212. URL: https://www.sciencedirect.com/science/article/pii/S0378382025000360.

[87] Roberto Scataglini et al. *A Total Cost of Ownership Model for Solid Oxide Fuel Cells in Combined Heat and Power and Power-Only Applications*. Technical Report LBNL-1004371. Supported by the U.S. Department of Energy, Office of Energy Efficiency and Renewable Energy (EERE) Fuel Cells Technologies Office (FCTO). Berkeley, California: Ernest Orlando Lawrence Berkeley National Laboratory, Dec. 2015.

[88] Julian Schiffler and Valeria Jan Schwanitz. *Methanol as a marine fuel: Environmental performance, availability, and cost*. 2021. URL: http://oeko.de/fileadmin/oekodoc/Methanol-as-a-marine-fuel.pdf.

[89] S.I. Schöffer et al. “A solid oxide fuel cell- supercritical carbon dioxide Brayton cycle hybrid system”. In: *Applied Energy* 283 (2021), p. 115748. ISSN: 0306-2619. DOI: https://doi.org/10.1016/j.apenergy.2020.115748. URL: https://www.sciencedirect.com/science/article/pii/S0306261920312356.

[90] Sang Hern Seo and Chang Sik Lee. “A study on the overall efficiency of direct methanol fuel cell by methanol crossover current”. In: *Applied Energy* 87.8 (2010), pp. 2597–2604. ISSN: 0306-2619. DOI: https://doi.org/10.1016/j.apenergy.2010.01.018. URL: https://www.sciencedirect.com/science/article/pii/S0306261910000310.

[91] Ray Sinnott and Gavin Towler. *Chemical Engineering Design*. 6th. Coulson and Richardson’s Chemical Engineering Series. Butterworth-Heinemann, an imprint of Elsevier, 2020. ISBN: 978-0-08-102599-4.

[92] T. L. Skafte et al. “Quantitative review of degradation and lifetime of solid oxide cells and stacks”. In: *Proceedings of 12th European SOFC & SOE Forum 2016*. Article B0501, European Fuel Cell Forum. 2016, pp. 8–27.

[93] James T. Sun, Ian S. Metcalfe, and Mortaza Sahibzada. “Deactivation of $Cu/ZnO/Al_2O_3$ Methanol Synthesis Catalyst by Sintering”. In: *Industrial & Engineering Chemistry Research* 38.10 (Sept. 1999), pp. 3868–3872. DOI: 10.1021/ie990114p.

[94] The Engineering ToolBox. *Heat Exchangers– Overall Heat Transfer Coefficients*. Online. 2003. URL: https://www.engineeringtoolbox.com/heat-transfer-coefficients-exchangers-d_450.html.

[95] The Engineering Toolbox. *Refrigerants– Ozone Depletion (ODP) and Global Warming Potential (GWP)*. https://www.engineeringtoolbox.com/Refrigerants-Environment-Properties-d_1220.html. 2025.

[96] TNO. *Assessment and Reduction of Maritime Sector GHG Emissions: A Feasibility Study*. Tech. rep. TNO-2020-R11105. TNO, 2020. URL: https://publications.tno.nl/publication/34637282/W1qAlG/TNO-2020-R11105.pdf.

[97] Takuya Tsujiguchi, Takayuki Furukawa, and Nobuyoshi Nakagawa. “Effect of the impurities in crude bio-methanol on the performance of the direct methanol fuel cell”. In: *Journal of Power Sources* 196.22 (2011), pp. 9339–9345. ISSN: 0378-7753. DOI: https://doi.org/10.1016/j.jpowsour.2011.08.025. URL: https://www.sciencedirect.com/science/article/pii/S0378775311015254.

[98] European Union. *Strategic Research and Innovation Agenda 2021 – 2027*. https://www.clean-hydrogen.europa.eu/document/download/8a35a59b-a689-4887-a25a-6607757bbd43_en. Clean Hydrogen Partnership, 2022.

[99] United Nations Conference on Trade and Development (UNCTAD). *Review of Maritime Transport 2021*. Geneva: United Nations Publications, 2021. URL: https://unctad.org/topic/transport-and-trade-logistics/review-of-maritime-transport.

[100] United Nations Conference on Trade and Development (UNCTAD). *Review of Maritime Transport 2023: Towards a Green and Just Transition*. Geneva: United Nations Publications, 2023. ISBN: 978-92-1-002886-8. URL: https://unctad.org/system/files/official-document/rmt2023_en.pdf.

[101] Yoshikazu Usami et al. “Catalytic methanol decomposition at low temperatures over palladium supported on metal oxides”. In: *Applied Catalysis A: General* 171.1 (1998), pp. 123–130. ISSN: 0926-860X. DOI: https://doi.org/10.1016/S0926-860X(98)00082-9. URL: https://www.sciencedirect.com/science/article/pii/S0926860X98000829.

[102] Bruno Vanslambrouck et al. “Efficiency comparison between the steam cycle and the organic rankine cycle for small scale power generation”. In: Jan. 2012, p. 13.

[103] Feadship / de Voogt Naval Architects. *MENENS F4 MBSE Pilot Reduced Use Case*. Internal document, BN710 Primary Power System, December 2024. 2024.

[104] Kenneth E. Voss et al. *Design and Analysis of a 5-kW SOFC System for Telecommunication Backup Power*. NASA Technical Memorandum NASA/TM—2005-213805. NASA Glenn Research Center, 2005. URL: https://ntrs.nasa.gov/api/citations/20060003629/downloads/20060003629.pdf.

[105] J.S. Wainright, M.H. Litt, and Robert Savinell. “In Handbook of Fuel Cells; W. Vielstichm, A. Lamm, H. A. Gasteiger”. In: *Editors.; John Wiley and Sons Ltd.: New York* 3 (Jan. 2003).

[106] W. Wiese, B. Emonts, and R. Peters. “Methanol steam reforming in a fuel cell drive system”. In: *Journal of Power Sources* 84.2 (1999), pp. 187–193. ISSN: 0378-7753. DOI: https://doi.org/10.1016/S0378-7753(99)00316-X. URL: https://www.sciencedirect.com/science/article/pii/S0378775399900316X.

[107] M. Winterberg and E. Tsotsas. “Impact of tube-to-particle-diameter ratio on pressure drop in packed beds”. In: *AIChE Journal* 46.5 (2000), pp. 1084–1088. DOI: https://doi.org/10.1002/aic.690460519. eprint: https://aiche.onlinelibrary.wiley.com/doi/pdf/10.1002/aic.690460519. URL: https://aiche.onlinelibrary.wiley.com/doi/abs/10.1002/aic.690460519.

[108] Takahisa Yamamoto et al. “Design and testing of the Organic Rankine Cycle”. In: *Energy* 26.3 (2001), pp. 239–251. ISSN: 0360-5442. DOI: https://doi.org/10.1016/S0360-5442(00)00063-3. URL: https://www.sciencedirect.com/science/article/pii/S0360544200000633.

[109] Fan Yang, Xin-Jian Zhu, and Guang-Yi Cao. “Nonlinear fuzzy modeling of a MCFC stack by an identification method”. In: *Journal of Power Sources* 166.2 (2007), pp. 354–361. ISSN: 0378-7753. DOI: https://doi.org/10.1016/j.jpowsour.2007.01.062. URL: https://www.sciencedirect.com/science/article/pii/S0378775307002467.

[110] Yunqi Yu et al. “Recent progress on reduced graphene oxide supported Pt-based catalysts and electrocatalytic oxidation performance of methanol”. In: *International Journal of Hydrogen Energy* 48.5 (2023), pp. 1785–1812. ISSN: 0360-3199. DOI: https://doi.org/10.1016/j.ijhydene.2022.10.021. URL: https://www.sciencedirect.com/science/article/pii/S0360319922046444.

[111] Vasiola Zhaka and Björn Samuelsson. “Hydrogen as fuel in the maritime sector: From production to propulsion”. In: *Energy Reports* 12 (2024), pp. 5249–5267. ISSN: 2352-4847. DOI: https://doi.org/10.1016/j.egyr.2024.11.005. URL: https://www.sciencedirect.com/science/article/pii/S2352484724007261.

[112] Heng Zhang et al. “High-Performance Cu/ZnO/Al2O3 Catalysts for CO2 Hydrogenation to Methanol”. In: *Industrial & Engineering Chemistry Research* 63.14 (2024), pp. 6210–6221. DOI: 10.1021/acs.iecr.4c00357. URL: https://doi.org/10.1021/acs.iecr.4c00357.

[113] Huajing Zhang et al. “Enhancement of methanol steam reforming in a tubular fixed-bed reactor with simultaneous heating inside and outside”. In: *Energy* 254 (2022), p. 124330. ISSN: 0360-5442. DOI: https://doi.org/10.1016/j.energy.2022.124330. URL: https://www.sciencedirect.com/science/article/pii/S0360544222012336.

[114] Li Zhang et al. “Comparative study of solid oxide fuel cell combined heat and power system with Multi-Stage Exhaust Chemical Energy Recycling: Modeling, experiment and optimization”. In: *Energy Conversion and Management* 139 (2017), pp. 79–88. ISSN: 0196-8904. DOI: https://doi.org/10.1016/j.enconman.2017.02.045. URL: https://www.sciencedirect.com/science/article/pii/S0196890417301565.

[115] Mengyuan Zhang et al. “Recent Advances in Methanol Steam Reforming Catalysts for Hydrogen Production”. In: *Catalysts* 15 (Jan. 2025), p. 36. DOI: 10.3390/catal15010036.

[116] Jimin Zhu et al. “Modeling and Design of a Multi-Tubular Packed-Bed Reactor for Methanol Steam Reforming over a Cu/ZnO/Al2O3 Catalyst”. In: *Energies* 13.3 (2020). ISSN: 1996-1073. DOI: 10.3390/en13030610. URL: https://www.mdpi.com/1996-1073/13/3/610.

A

MATLAB Codes

A.1. MATLAB Kinetic Model Validation Code

```
clc; clear;

% Constants
R = 8.314; %J/(mol·K)
T = 246 + 273.15; % K
Ea = 65590; %J/mol
A = 53.48; % molCH3OH/(s*gcatalyst*kPa^0.38)

% Catalyst weight
Wcat = 0.05; % kg

% Table data
P_CH3OH_list = [57.09, 50.67, 44.26, 37.84, 31.43, 25.01]; % kPa
P_H2O_list = [38.63, 38.63, 38.63, 38.63, 38.63, 38.63];   % kPa
W_by_F = [0.99, 1.11, 1.28, 1.49, 1.80, 2.26];             % kg·s/mol
H2O_CH3OH_ratio = [0.66, 0.74, 0.85, 0.99, 1.20, 1.50];
P_N2_list=[5.61, 12.03, 18.45,24.86,31.28,37.69];  % kPa

V_total_mlmin = 220; % Total feed flow rate in mL/min
P_total_kPa = 101.325; % Total pressure in kPa (1 atm)

%  volumetric flow in m^3/s
V_total_m3s = (V_total_mlmin / 1e6) / 60; % Convert mL/min to m^3/s
V_n2_m3s = V_total_m3s * (P_N2_list / P_total_kPa);

% Convert to mol/s using ideal gas law: n = PV / RT
P_n2_Pa = P_N2_list * 1000; % kPa to Pa
F_n2_mol_s = (P_n2_Pa .* V_n2_m3s) / (R * T);

% Convert to actual molar flows
F_CH3OH_list = Wcat / 1000 ./ W_by_F;        % mol/s (from W/F)
F_H2O_list = F_CH3OH_list .* H2O_CH3OH_ratio; % mol/s
F_total_list = F_CH3OH_list + F_H2O_list+F_n2_mol_s;

conversion_model = zeros(1,6);

% Loop for each set
for i = 1:6
    F_CH3OH = F_CH3OH_list(i);
    F_H2O = F_H2O_list(i);
    F_N2= F_n2_mol_s (i);
    F_total = F_CH3OH + F_H2O+F_N2;
    y0 = [F_CH3OH; F_H2O; 0; 0];

    % Partial pressures
    P_total = P_CH3OH_list(i) + P_H2O_list(i)+P_N2_list(i);

    % Define ODE
    msr_ode = @(W, F) reaction_ode(F, T, R, A, Ea, P_total);

```

```
    % Solve ODE
    opts = odeset('RelTol',1e-10,'AbsTol',1e-12);
    [W, Fsol] = ode45(msr_ode, [0 Wcat], y0, opts);
    F_out = Fsol(end, :)';

    % Conversion
    conversion_model(i) = 100*((F_CH3OH - F_out(1)) / F_CH3OH);
end

% --- Experimental Conversion ---
 rate_exp = [6.24, 6.11, 5.78, 5.53, 5.39, 5.05] * 1e-5; % mol/s/g

conversion_exp = rate_exp .* (W_by_F * 1000); % fraction
conversion_exp_percent = conversion_exp * 100;

% --- Plot ---
figure;
set_num = 1:6;

% Model simulation
plot(P_CH3OH_list, conversion_model, '-sb', 'LineWidth', 2, ...
    'DisplayName','Kinetic␣model'); hold on;

% Experimental values (corrected W/F units)
plot(P_CH3OH_list, conversion_exp_percent, '-o', 'Color', [1 0.5 0], 'LineWidth', 2, ...
    'DisplayName','Experimental');

 xlim([20 60])
 xlabel('CH_3OH␣partial␣pressure␣(kPa)');
 ylabel('CH_3OH␣conversion␣(%)');
 legend('Location','northeast');
 title('MSR␣Kinetic␣Model␣Validation');
grid on;

% --- Reaction ODE ---
function dFdW = reaction_ode(F, T, R, A, Ea, P_total)
    F_sum = sum(F);
    if F_sum <= 0
        dFdW = zeros(4,1);
        return;
    end
    y = F / F_sum;
    P_CH3OH = max(y(1) * P_total, 1e-6); % avoid zero
    P_H2O   = max(y(2) * P_total, 1e-6);

    k = A * exp(-Ea / (R * T));
    r = k * (P_CH3OH^0.29) * (P_H2O^0.09);

    dFdW = [-r; -r; r; 3*r];
end

% --- Calculate R-squared (R^2) ---
y_true = conversion_exp_percent;   % Experimental conversion (%)
y_pred = conversion_model;         % Modeled conversion (%)

SS_res = sum((y_true - y_pred).^2);
SS_tot = sum((y_true - mean(y_true)).^2);

R_squared = 1 - SS_res / SS_tot;

% Display result
fprintf('R-squared␣between␣model␣and␣experimental␣conversion:␣%.4f\n', R_squared);
```

A.2. MATLAB Molar Composition Graph Code

```
clc; clear;

% Constants
R = 8.314; % J/mol/K
T = 246 + 273.15; % Temperature in Kelvin
Ea = 65590; % Activation energy (J/mol)
A = 53.48; % Pre-exponential factor (mol/s/g/kPa^0.38)
P_total = 101.325; % Total pressure in kPa

% Catalyst bed setup
bed_length_cm = 1.5;
catalyst_loading_g = 1;
catalyst_density = catalyst_loading_g / bed_length_cm; % g/cm

zspan_cm = linspace(0, bed_length_cm, 100);
Wspan = zspan_cm * catalyst_density; % g

% Feed conditions from paper (converted to mol/s)
F_CH3OH = 2e-6 * 1000 / 60; % kmol/min to mol/s
F_H2O = 3e-6 * 1000 / 60;
F0 = [F_CH3OH; F_H2O; 0; 0];

% ODE solver
opts = odeset('RelTol',1e-8,'AbsTol',1e-10);
[W, F] = ode45(@(W, F) msr_ode(F, T, R, A, Ea, P_total), Wspan, F0, opts);

% Mole fractions
F_sum = sum(F, 2);
Y = F ./ F_sum;

% Position in cm
z_plot = W / catalyst_density;

% Plot
figure;
hold on;

% Sample every 0.15 cm
z_marker = 0:0.15:max(z_plot);
Y_interp = interp1(z_plot, Y, z_marker);

plot(z_plot, Y(:,1), 'r-', 'DisplayName','CH_3OH');
plot(z_plot, Y(:,2), '-', 'Color', [0, 0.5, 0], 'DisplayName','H_2O');
plot(z_plot, Y(:,3), 'b-', 'DisplayName','CO_2');
plot(z_plot, Y(:,4), 'k-', 'DisplayName','H_2');

% Add solid dots at 0.15 cm intervals
plot(z_marker, Y_interp(:,1), 'ro', 'MarkerFaceColor','r', 'HandleVisibility','off');
plot(z_marker, Y_interp(:,2), 'o', 'Color', [0, 0.5, 0], 'MarkerFaceColor', [0, 0.5, 0], '
    HandleVisibility','off');  % Dark green dots
plot(z_marker, Y_interp(:,3), 'bo', 'MarkerFaceColor','b', 'HandleVisibility','off');
plot(z_marker, Y_interp(:,4), 'ko', 'MarkerFaceColor','k', 'HandleVisibility','off');

xlabel('Catalyst␣bed␣length␣(cm)');
xticks(0:0.15:max(z_plot)); % Add x-axis ticks every 0.15 cm
ylabel('Reactor␣molar␣composition');
title('Molar␣composition␣along␣reactor');
legend('Location','best');
grid on;

% --- ODE function ---
function dFdW = msr_ode(F, T, R, A, Ea, P_total)
    % Avoid division by zero
    F_sum = max(sum(F), 1e-12);
    y = F / F_sum;

    % Partial pressures (kPa)
    P_CH3OH = y(1) * P_total;
    P_H2O = y(2) * P_total;

    % Rate constant
    k = A * exp(-Ea / (R * T)); % mol/g/s/kPa^0.38
```

```
72
73      % Rate expression from paper (Eq. 10)
74      r = k * (P_CH3OH^0.29) * (P_H2O^0.09); % mol/g/s
75
76      % Stoichiometry
77      dFdW = zeros(4,1);
78      dFdW(1) = -r;      % CH3OH
79      dFdW(2) = -r;      % H2O
80      dFdW(3) = +r;      % CO2
81      dFdW(4) = +3*r;    % H2
82  end
```

A.3. MATLAB SOFC Model Validation Code

```
1   clear all;
2   clc;
3
4
5   % Constants and Parameters
6
7   p = 0.986923;          % bar -> atm (stack pressure in atm)
8   F = 96485;             % Faraday's constant (C/mol)
9   R = 8.314;             % gas constant (J/(mol*K))
10  Uf = 0.85;             % Fuel utilization
11  Patm = 101325;         % 1 atm in Pa
12  Astack = 0.0016;       % Cell active area (m^2)
13  T = 850 + 273.15;      % Operating temperature (K)
14
15  % Fuel Electrode Parameters
16  n_FE = 2;              % electrons transferred
17  alpha_FE = 0.5;        % symmetry factor
18  gamma_FE = 1.34e10;    % pre-exponential factor (A m^-2)
19  E_act_FE = 1.00e5;     % activation energy (J mol^-1)
20
21  % Air Electrode Parameters
22  n_AE = 4;              % electrons transferred
23  alpha_AE = 0.5;        % symmetry factor
24  gamma_AE = 2.05e9;     % pre-exponential factor (A m^-2)
25  E_act_AE = 1.20e5;     % activation energy (J mol^-1)
26
27  % Electrolyte Properties
28  delta_el = 1.25e-5;    % electrolyte thickness (m)
29  gamma_el = 3.33e4;     % pre-exponential factor for conductivity Ω(^-1 m^-1)
30  E_act_el = 85634;      % activation energy for conductivity (J mol^-1)
31
32  % Electronic Resistance
33  r_const = 5.70e-6;     % electronic area-specific Ohmic resistance Ω( m^2)
34
35  % Diffusion Volumes
36  V_d_H2   = 6.12;
37  V_d_H2O  = 13.10;
38  V_d_O2   = 16.30;
39  V_d_N2   = 18.50;
40
41  % Molecular Masses (g/mol)
42  M_h2  = 2.02;
43  M_h2o = 18.02;
44  M_o2  = 32.00;
45  M_N2  = 28.01;
46
47  % Electrode Properties
48  epsilon   = 0.30;          % porosity
49  tau       = 5.00;          % tortuosity
50  d_p       = 2.00e-6;       % mean pore diameter (m)
51  delta_FE  = 3.20e-5;       % fuel electrode thickness (m)
52  delta_AE  = 1.75e-5;       % air electrode thickness (m)
53
54  % Bulk pressures (Pa)
55  p_H2_bulk  = 0.5 * 10^5;
56  p_H2O_bulk = 0.5 * 10^5;
57  p_O2_bulk  = 1* 10^5;
58
59  % Knudsen Diffusivities (m^2/s)
```

```
D_Kn_H2O = (d_p / 3) * sqrt((8 * R * T) / (pi * M_h2o));
D_Kn_H2  = (d_p / 3) * sqrt((8 * R * T) / (pi * M_h2));
D_Kn_O2  = (d_p / 3) * sqrt((8 * R * T) / (pi * M_o2));

% Diffusivities : p is in atm, T in K
D_H2_H2O = (1.43e-7 * T^1.75) / ...
           (p * sqrt((2 * M_h2 * M_h2o) / (M_h2 + M_h2o)) * ...
           ((V_d_H2O^(1/3) + V_d_H2^(1/3))^2));
D_O2_N2  = (1.43e-7 * T^1.75) / ...
           (p * sqrt((2 * M_o2 * M_N2) / (M_o2 + M_N2)) * ...
           ((V_d_O2^(1/3) + V_d_N2^(1/3))^2));



% Effective Diffusivities
D_eff_H2  = (epsilon / tau) * (D_Kn_H2  * D_H2_H2O) / (D_Kn_H2  + D_H2_H2O);
D_eff_H2O = (epsilon / tau) * (D_Kn_H2O * D_H2_H2O) / (D_Kn_H2O + D_H2_H2O);
D_eff_O2  = (epsilon / tau) * (D_Kn_O2  * D_O2_N2 ) / (D_Kn_O2  + D_O2_N2 );


jValues = -10021:10720;             % range of current densities (A/m^2)

U_cell_FC_vals = zeros(size(jValues));


%  U_cell_FC for Each j

for i = 1:length(jValues)
    j = jValues(i);

    % Current (A)
    I = j * Astack;


    p_H2_TPB  = p_H2_bulk  - (R * T * delta_FE * j) / (2 * F * D_eff_H2 );
    p_H2O_TPB = p_H2O_bulk + (R * T * delta_FE * j) / (2 * F * D_eff_H2O);
    p_O2_TPB  = p_O2_bulk  - (R * T * delta_AE * j) / (4 * F * D_eff_O2 );

    % Concentration overpotentials
    U_conc_FE = ((R * T) / (2 * F)) * log((p_H2_bulk * p_H2O_TPB) / (p_H2_TPB * p_H2O_bulk));
    U_conc_AE = ((R * T) / (2 * F)) * log((p_O2_bulk^0.5) / (p_O2_TPB^0.5));

    % Nerst voltage


    ph2  = 0.5;  % atm
    po2  = 1;  % atm
    ph2o = 0.5;  % atm
    patm = 1.05; % atm


     E = (4187 * (58.3 - (0.0113 + 9.6e-7 * T)*T))  / (2 * F) + (R*T/(2*F)) * log((ph2*(po2^0.5))
         / (ph2o*(patm^0.5)));

    % Exchange current densities
    j0_AE = gamma_AE * exp(-E_act_AE / (R * T));
    j0_FE = gamma_FE * exp(-E_act_FE / (R * T));

    % Activation overpotentials
    U_act_AE = (R * T) / (n_AE * F * alpha_AE) * asinh(j / (2 * j0_AE));
    U_act_FE = (R * T) / (n_FE * F * alpha_FE) * asinh(j / (2 * j0_FE));

    % Electrolyte conductivity
    sigma_0_el = 3.33e4;  % Ω(^-1 m^-1)
    sigma_el   = sigma_0_el * exp(-E_act_el / (R * T));

    % Ohmic overpotential
    U_ohm = j * ((delta_el / sigma_el) + r_const);

    % Total cell voltage
    U_cell_FC_vals(i) = E - U_act_FE - U_act_AE - U_ohm - U_conc_FE - U_conc_AE;
end


```

```
% Experimental Data
% ==========================
ExpData = [
  -10022.727272727274, 1.1689059500959693;
  -8318.18181818182,   1.125911708253359;
  -6443.181818181819,  1.0856046065259117;
  -4704.545454545457,  1.0452975047984645;
  -3034.09090909091,   1.0103646833013435;
  -1636.363636363636,  0.980806142034549;
  -477.27272727272975, 0.9593090211132437;
   613.636363636364,   0.9404990403071017;
  2147.7272727272684,  0.9136276391554702;
  5556.8181818181818,  0.8518234165067179;
  8420.45454545454,    0.800767754318618;
 10772.727272727265,   0.7577735124760078
];


% ==========================
% Plot
figure;

plot(jValues, U_cell_FC_vals, 'LineWidth',2, ...
    'DisplayName','Simulation');
hold on;


plot(ExpData(:,1), ExpData(:,2), 'ks', 'MarkerFaceColor','r', ...
    'DisplayName','Experiment');

hold off;

xlabel('Current Density (A/m^2)');
ylabel('Voltage (V)');
title('SOFC Model Validation');
legend('Location','best');
grid on;


ylim([0 1.4]);
yticks(0:0.2:1.4);


% ==========================
% R^2 Correlation Calculation



sim_interp = interp1(jValues, U_cell_FC_vals, ExpData(:,1), 'linear', 'extrap');

% Extract experimental voltages
exp_voltage = ExpData(:,2);

% Compute R^2
SS_res = sum((exp_voltage - sim_interp).^2);                          % Residual sum of squares
SS_tot = sum((exp_voltage - mean(exp_voltage)).^2);                  % Total sum of squares
R_squared = 1 - (SS_res / SS_tot);

% Print  R^2
fprintf('R² between simulation and experimental data: %.4f\n', R_squared);
```

B

ORC Working Fluids

Table B.1 summarizes some of the most significant environmental and thermophysical properties of various considered working fluids for the ORC system, including their molecular mass, critical pressure and temperature, global warming potential (GWP), and ozone depletion potential (ODP). Among of the listed fluids, R1233zd(E) and R1234ze(E) have the least environmental impact, with a GWP of 5 and 7, respectively, and an ODP of zero, and hence are promising candidates for future sustainable ORC application. Next, R123 has the highest critical temperature (183.7 °C), and a relatively low GWP of 77, but a non-zero ODP of 0.0015 and is therefore potentially less desirable to use in environmentally sensitive applications. The working fluids R245fa and R134a however, have considerably higher GWP figures (1,030 and 1,430, respectively) but zero ODP, and are therefore less environmentally desirable options. The thermophysical data also confirm that most of these fluids have a similar range of critical pressures (approximately 36–41 bar) of interest for the design of systems and sizing of equipment. Overall, the ORC working fluid choice is a balance between physical properties and environmental factors, with newer fluids like the R1233zd(E) and R1234ze(E) promising low-GWP options.

Table B.1: Environmental and thermophysical properties of different ORC working fluids.

Working fluid	Molecular Mass (g/mol)	T_{crit} (°C)	P_{crit} (bar)	GWP	ODP	Source
R1233zd(E)	130.5	166.5	36.2	5	0	[22]
R1234ze(E)	114.0	109.4	36.4	7	0	[21]
R123	152.9	183.7	36.6	77	0.0015	[2]
R245fa	134.0	154.0	36.5	1,030	0	[42]
R134a	102.0	101.1	40.6	1,430	0	[41, 95]

C

SOFC and Heat Utilization Network Sizing

C.1. SOFC Sizing Process

To size the SOFC stack, the design focuses on the maximum system power level of 325 kW, as this represents the most demanding operational condition of the system. The SOFC must supply sufficient power to cover the superyacht's auxiliary power demand as well as the auxiliary loads from the air compressor and the sea water reverse osmosis unit. However, at the beginning of the sizing process, the power consumption of the compressor and SWRO unit is unknown, as these depend on system parameters: the SOFC area, which is an input and current density, which is internally adjusted in Aspen Plus via a Design Specification to meet the total system power of 325 kW. The ORC contributes a known 14.1 kW, meaning the SOFC must initially be sized to provide the remaining 310.91 kW.

As a first approximation, the system is sized assuming zero auxiliary loads (compressor and SWRO), yielding a minimum SOFC area of 63.45 m^2. This area is then input into Aspen Plus, which calculates the resulting power demands for the compressor and SWRO. With these new demands, the required SOFC power is updated, and a new area is calculated. Through successive iterations, this process converges to a final SOFC area of 72.58 m^2. In the simulations, a slightly different approach was employed: after the initial estimate of 63.45 m^2, a larger area of 69.7 m^2 was input in Aspen Plus, resulting in an updated required area of 72.65 m^2. For consistency, an area of 72.7 m^2 was adopted for all simulations. While the iterative method provides a more accurate convergence, both approaches yield very similar final results.

Table C.1: Iterative SOFC sizing results based on input area values and resulting auxiliary power demands.

A (m^2)	$P_{max\ sys}$ (kW)	P_{compr} (kW)	P_{SWRO} (kW)	$P_{SOFC\ net}$ (kW)	$P_{SOFC,generation}$ (kW)	Note
Iterative method						
63.45	325	0	0	310.91	310.91	Initial estimate
72.85	325	16.71	29.3813	310.91	357.00	Step 1
72.57	325	15.35	29.3507	310.91	355.61	Step 2
72.58	325	15.38	29.3513	310.91	355.64	Step 3
72.58	325	15.38	29.3514	310.91	355.64	Final value
Alternative method: After initial estimate, input A = 69.7 m^2						
63.45	325	0	0	310.91	310.91	Initial estimate
69.70	325	15.74	29.3597	310.91	356.01	Input value
72.65	325	15.74	29.3597	310.91	356.01	Final value

C.2. Heat Utilization Network Design Process

As mentioned in subsection 8.4, the design of the heat recovery network was a trial-and-error process. Figure C.1 illustrates three preliminary heat utilization network designs that were tested and ultimately found unsuitable for final implementation since they did not meet the key criteria described in subsection 7.5.

In the first design (Figure C.1a), the afterburner was placed after the air and fuel preheating stages. As a result, it operated at a relatively low temperature of around 290 °C. This low temperature was insufficient to ensure the complete combustion of the unreacted fuel within the SOFC. Furthermore, the air preheating in this design employed an auxiliary electrical heater in order to reach the required inlet temperature for the SOFC cathode, which is undesirable in terms of energy efficiency and practical operation. The reliance on electrical heating goes against the system's goal of maximizing internal heat recovery.

The second design (Figure C.1b) represents an improved design of the first configuration. In this case, the afterburner was moved upstream, providing thermal energy directly to the air preheating. While this change improved the overall heat recovery, it was still inadequate to fully preheat both the cathode air stream and the MSR reactor. As a result, an electrical heater was again required to meet the air temperature demands. Moreover, the exhaust gas was exiting the system at high temperatures (around 150 °C), indicating that the heat could be better distributed and recovered in the network. The main limitation of this design was that air preheating occurred in a single stage, which prevented it from meeting the needs for both air and fuel reforming simultaneously.

The third design (Figure C.1c) is the closest to the final design configuration and the system's thermal integration goals. In this configuration, the exhaust gas was redirected from the ORC condenser back into the air preheating stages, forming a three-stage, temperature-based air preheating design. With this approach, a more gradual and thermodynamically favorable heat exchange was achieved. However, this design presented a significant drawback. The exhaust gas was exiting the system at 37 °C, which was below its vaporization temperature, resulting in condensation and creating issues for system performance and exhaust handling. As a result, the design was not suitable for implementation, even with its improved heat integration strategy.

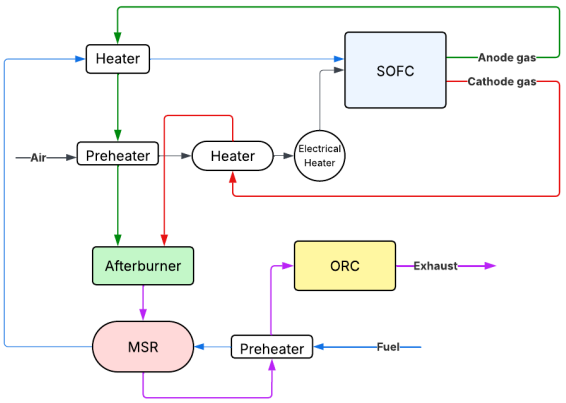

(a) First Design.

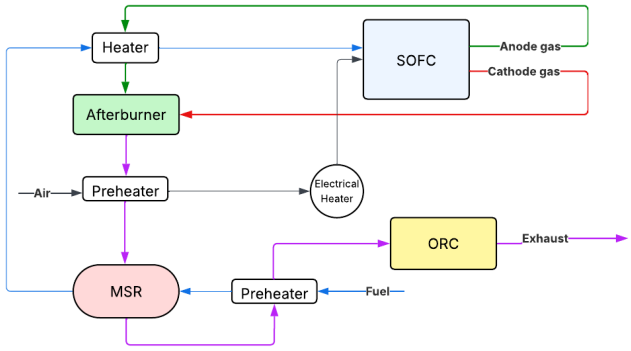

(b) Second Design.

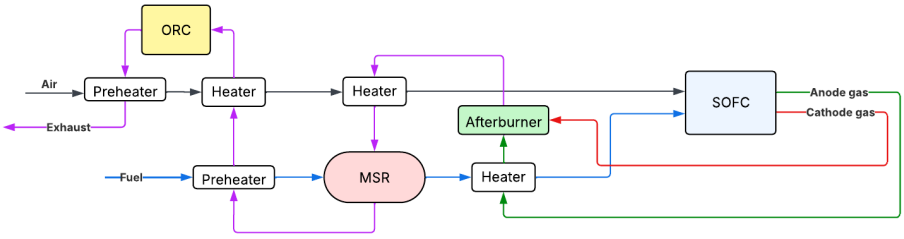

(c) Third Design.

Figure C.1: Three different heat utilization network trial designs.

D

Catalyst mass calculation

The reactor bed voidage is described in Equation D.1, where ρ_b and ρ_{cat} are the densities of the bed and the catalyst, respectively. Knowing the bed voidage and the catalyst density, the bed density can be calculated, and is equal to 806 kg/m^3.

$$\epsilon = 1 - \frac{\rho_b}{\rho_{cat}} \Rightarrow \ \rho_b = \rho_{cat} \cdot (1 - \epsilon) = 1300 kg/m^3 \cdot (1 - 0.38) = 806 kg/m^3 \tag{D.1}$$

Equation D.2 expresses the reactor's volume, where N is the number of tubes, r is the tube radius and h is the length. The volume is equal to 0.025 m^3.

$$V_{reactor} = N \cdot \pi r^2 h = 95 \cdot \pi \cdot (0.08^2) \cdot 1.3 = 0.025 m^3 \tag{D.2}$$

Using the reactor's volume and the density of the bed, the mass of the catalyst in the reactor can be calculated using Equation D.3, and is equal to 20.15 kg.

$$W_{cat} = \rho_b \cdot V_{reactor} = 806 kg/m^3 \cdot 0.025 m^3 = 20.15 kg \tag{D.3}$$

E

Sensitivity analysis - Case 1: Fuel Utilization

E.1. System Power Level: 325 kW

Table E.1: SOFC Operation and Efficiency for varying $U_f = 0.7$–0.9 at system power level of 325 kW.

U_f	$P_{\text{SOFC, generation}}$ (kW)	Current Density (A/m^2)	Voltage (V)	η_{SOFC}
0.7	364.6	6,016.2	0.834	46.5%
0.75	359.7	5,952.1	0.831	49.7%
0.8	355.6	5,902.7	0.829	52.9%
0.85	352.1	5,865.2	0.826	56.0%
0.9	349.1	5,838.3	0.823	59.0%

Table E.2: Key temperatures for varying $U_f = 0.7$–0.9 at system power level of 325 kW.

U_f	$T_{\text{air,in,SOFC}}$ (°C)	$T_{\text{exhaust,out}}$ (°C)	$T_{\text{afterburner}}$ (°C)
0.7	728.6	107.6	864.2
0.75	712.7	98.9	854.6
0.8	692.4	88.3	842.0
0.85	665.9	74.9	825.6
0.9	630.4	57.6	803.6

Table E.3: Methanol, air and water consumptions for varying $U_f = 0.7$–0.9 at system power level of 325 kW.

U_f	Methanol (t/yr)	Air (m^3/yr)	Water (m^3/yr)
0.7	1,091.4	123,508.1	17,082.7
0.75	1,007.8	102,070.2	17,021.5
0.8	936.9	83,945.4	16,969.6
0.85	876.2	68,359.6	16,925.2
0.9	823.7	54,928.5	16,886.7

Table E.4: System's electrical and CHP efficiencies for varying $U_f = 0.7$–0.9 at system power level of 325 kW.

U_f	$\eta_{\text{el,sys}}$	η_{CHP}
0.7	44.6%	56.6%
0.75	48.3%	61.3%
0.8	52.0%	65.9%
0.85	55.6%	70.5%
0.9	59.1%	75.0%

E.2. System Power Level : 275 kW

Table E.5: SOFC Operation and Efficiency for varying $U_f = 0.7$–0.9 at system power level of 275 kW.

U_f	$P_{\text{SOFC, generation}}$ (kW)	Current Density (A/m^2)	Voltage (V)	η_{SOFC}
0.7	301.61	4,860.4	0.854	47.7%
0.75	297.79	4,813.3	0.851	50.9%
0.8	294.53	4,776.7	0.848	54.1%
0.85	291.76	4,749.2	0.845	57.3%
0.9	The heat network cannot fully preheat the air and heat the ORC.			

Table E.6: Key temperatures for varying $U_f = 0.7$–0.9 at system power level of 275 kW.

U_f	$T_{\text{air,in,SOFC}}$ (°C)	$T_{\text{exhaust,out}}$ (°C)	$T_{\text{afterburner}}$ (°C)
0.7	729.6	95.5	868.6
0.75	713.1	84.1	858.5
0.8	691.8	69.8	845.5
0.85	663.6	51.5	828.4
0.9	The heat network cannot fully preheat the air and heat the ORC.		

Table E.7: Methanol, air and water consumptions for varying $U_f = 0.7$–0.9 at system power level of 275 kW.

U_f	Methanol (t/yr)	Air (m^3/yr)	Water (m^3/yr)
0.7	881.7	96,066.6	16,929.2
0.75	814.9	78,964.5	16,880.3
0.8	758.2	64,383.9	16,838.7
0.85	709.5	51,909.7	16,803.1
0.9	The heat network cannot fully preheat the air and heat the ORC.		

Table E.8: System's electrical and CHP efficiencies for varying $U_f = 0.7$–0.9 at system power level of 275 kW.

U_f	$\eta_{\text{el,sys}}$	η_{CHP}
0.70	46.7%	61.5%
0.75	50.5%	66.5%
0.80	54.3%	71.5%
0.85	58.1%	76.4%
0.90	The heat network cannot fully preheat the air and heat the ORC.	

E.3. System Power Level : 225 kW

Table E.9: SOFC Operation and Efficiency for varying $U_f = 0.7$–0.9 at system power level of 225 kW.

U_f	$P_{\text{SOFC, generation}}$ (kW)	Current Density (A/m^2)	Voltage (V)	η_{SOFC}
0.7	239.04	3,766.6	0.873	48.7%
0.75	236.13	3,732.7	0.870	52.1%
0.8	233.67	3,706.8	0.867	55.3%
0.85	The exhaust gas does not exit in vapor phase.			
0.9	The exhaust gas does not exit in vapor phase.			

Table E.10: Key temperatures for varying $U_f = 0.7$–0.9 at system power level of 225 kW.

U_f	$T_{\text{air,in,SOFC}}$ (°C)	$T_{\text{exhaust,out}}$ (°C)	$T_{\text{afterburner}}$ (°C)
0.7	730.7	77.0	872.1
0.75	713.6	61.2	861.8
0.8	691.3	41.2	848.3
0.85	The exhaust gas does not exit in vapor phase.		
0.9	The exhaust gas does not exit in vapor phase.		

Table E.11: Methanol, air and water consumptions for varying $U_f = 0.7$–0.9 at system power level of 225 kW.

U_f	Methanol (t/yr)	Air (m^3/yr)	Water (m^3/yr)
0.7	683.3	71,659.0	16,783.9
0.75	632.0	58,495.5	16,746.3
0.8	588.4	47,338.9	16,714.4
0.85	The exhaust gas does not exit in vapor phase.		
0.9	The exhaust gas does not exit in vapor phase.		

Table E.12: System's electrical and CHP efficiencies for varying $U_f = 0.7$–0.9 at system power level of 225 kW.

U_f	$\eta_{\text{el,sys}}$	η_{CHP}
0.7	49.3%	68.4%
0.75	53.3%	73.9%
0.8	57.2%	79.4%
0.85	The exhaust gas does not exit in vapor phase.	
0.9	The exhaust gas does not exit in vapor phase.	

F

Sensitivity analysis - Case 2: SOFC Temperature

F.1. System Power Level : 325 kW

Table F.1: SOFC Operation and Efficiency for varying T_{SOFC} = 700–1000 °C at system power level of 325 kW.

T_{SOFC} (°C)	$P_{\text{SOFC, generation}}$ (kW)	Current Density (A/m^2)	Voltage (V)	η_{SOFC}
700	365.8	7,009.4	0.718	45.8%
750	358.8	6,251.9	0.790	50.4%
800	355.6	5,902.7	0.829	52.9%
850	355.2	5,851.2	0.835	53.3%
900	355.4	5,880.6	0.831	53.1%
950	356.2	5,959.7	0.822	52.5%
1000	357.2	6,072.6	0.809	51.6%

Table F.2: Key temperatures for varying T_{SOFC} = 700–1000 °C at system power level of 325 kW.

T_{SOFC} (°C)	$T_{\text{air,in,SOFC}}$ (°C)	$T_{\text{exhaust,out}}$ (°C)	$T_{\text{afterburner}}$ (°C)
700	592.8	109.3	738.0
750	642.4	97.0	791.7
800	692.4	88.3	842.0
850	743.0	86.8	888.7
900	793.8	87.7	934.3
950	844.7	89.9	979.5
1000	895.6	92.8	1,024.7

Table F.3: Methanol, air and water consumptions for varying T_{SOFC} = 700-1000 °C at system power level of 325 kW.

T_{SOFC} (°C)	Methanol (t/yr)	Air (m^3/yr)	Water (m^3/yr)
700	1,112.6	128,932.7	17,098.3
750	992.4	98,124.9	17,010.2
800	936.9	83,945.4	16,969.6
850	928.8	81,823.0	16,963.6
900	933.4	83,037.9	16,967.1
950	946.0	86,258.3	16,976.3
1000	963.9	90,807.9	16,989.4

Table F.4: System's electrical and CHP efficiencies for varying T_{SOFC} = 700–1000 °C at system power level of 325 kW.

T_{SOFC} (°C)	$\eta_{el,sys}$	η_{CHP}
700	43.8%	55.5%
750	49.1%	62.2%
800	52.0%	65.9%
850	52.5%	66.5%
900	52.2%	66.2%
950	51.5%	65.3%
1000	50.5%	64.1%

F.2. System Power Level : 275 kW

Table F.5: SOFC Operation and Efficiency for varying T_{SOFC} = 700–1000 °C at system power level of 275 kW.

T_{SOFC} (°C)	$P_{SOFC,\ generation}$ (kW)	Current Density (A/m^2)	Voltage (V)	η_{SOFC}
700	300.08	5,387.3	0.766	48.9%
750	295.56	4,889.8	0.831	53.1%
800	294.53	4,776.7	0.848	54.1%
850	294.40	4,761.8	0.850	54.3%
900	294.76	4,800.5	0.845	53.9%
950	295.40	4,872.7	0.834	53.2%
1000	296.27	4,968.6	0.820	52.3%

Table F.6: Key temperatures for varying T_{SOFC} = 700–1000 °C at system power level of 275 kW.

T_{SOFC} (°C)	$T_{air,in,SOFC}$ (°C)	$T_{exhaust,out}$ (°C)	$T_{afterburner}$ (°C)
700	591.9	91.5	744.5
750	641.4	74.9	797.7
800	691.8	69.8	845.5
850	742.5	69.1	891.6
900	793.4	71.0	936.8
950	844.4	74.2	981.8
1000	895.3	78.2	1,026.9

Table F.7: Methanol, air and water consumptions for varying T_{SOFC} = 700–1000 °C at system power level of 275 kW.

T_{SOFC} (°C)	Methanol (t/yr)	Air (m^3/yr)	Water (m^3/yr)
700	855.1	89,239.2	16,909.7
750	776.2	68,989.7	16,851.9
800	758.2	64,383.9	16,838.7
850	755.8	63,791.3	16,837.0
900	762.0	65,384.0	16,841.5
950	773.4	68,288.2	16,849.9
1000	788.7	72,194.6	16,861.0

Table F.8: System's electrical and CHP efficiencies for varying T_{SOFC} = 700–1000 °C at system power level of 275 kW.

T_{SOFC} (°C)	$\eta_{\text{el,sys}}$	η_{CHP}
700	48.2%	63.4%
750	53.1%	69.9%
800	54.3%	71.5%
850	54.5%	71.8%
900	54.1%	71.2%
950	53.3%	70.1%
1000	52.2%	68.8%

F.3. System Power Level : 225 kW

Table F.9: SOFC Operation and Efficiency for varying T_{SOFC} = 700–1000 °C at system power level of 225 kW.

T_{SOFC} (°C)	$P_{\text{SOFC, generation}}$ (kW)	Current Density (A/m^2)	Voltage (V)	η_{SOFC}
700	236.33	4,003.4	0.812	51.8%
750	234.14	3,758.6	0.857	54.7%
800	233.67	3,706.8	0.867	55.3%
850	233.73	3,714.2	0.866	55.2%
900	234.09	3,755.1	0.857	54.7%
950	234.65	3,817.6	0.845	53.9%
1000	235.35	3,895.2	0.831	53.0%

Table F.10: SOFC Voltage breakdown for varying T_{SOFC} at system power level of 225 kW.

T_{SOFC} (°C)	V (V)	V_{Nesrt} (V)	V_{Ohm} (V)	V_{Conc} (V)	V_{Act} (V)
700	0.8120	0.9681	0.0822	0.0061	0.0678
800	0.8671	0.9386	0.0416	0.0064	0.0235
900	0.8575	0.9051	0.0306	0.0074	0.0097

Table F.11: Key temperatures for varying T_{SOFC} = 700–1000 °C at system power level of 225 kW.

T_{SOFC} (°C)	$T_{\text{air,in,SOFC}}$ (°C)	$T_{\text{exhaust,out}}$ (°C)	$T_{\text{afterburner}}$ (°C)
700	590.9	62.5	750.2
750	640.6	45.6	801.4
800	691.3	41.2	848.3
850	742.0	41.7	893.8
900	793.1	45.2	938.6
950	844.0	50.2	983.3
1000	895.0	55.7	1,028.2

Table F.12: Methanol, air and water consumptions for varying T_{SOFC} = 700–1000 °C at system power level of 225 kW.

T_{SOFC} (°C)	Methanol (t/yr)	Air (m^3/yr)	Water (m^3/yr)
700	635.5	59,388.1	16,748.8
750	596.6	49,452.2	16,720.4
800	588.4	47,338.9	16,714.4
850	589.6	47,604.4	16,715.2
900	596.0	49,256.4	16,720.0
950	606.0	51,803.9	16,727.2
1000	618.3	54,966.0	16,736.3

Table F.13: System's electrical and CHP efficiencies for varying T_{SOFC} = 700–1000 °C at system power level of 225 kW.

T_{SOFC} (°C)	$\eta_{\text{el,sys}}$	η_{CHP}
700	53.0%	73.5%
750	56.4%	78.3%
800	57.2%	79.4%
850	57.1%	79.2%
900	56.5%	78.4%
950	55.6%	77.1%
1000	54.4%	75.5%